2023

ENHANCING MICROSTRUCTURE, COMPOSITION HOMOGENEITY, AND MECHANICAL PROPERTIES IN LASER POWDER BED FUSED METALLIC ALLOYS: DESIGN, FABRICATION, AND EVALUATION

Bahzad Farhang

Recommended Citation

Farhang, Bahzad, "ENHANCING MICROSTRUCTURE, COMPOSITION HOMOGENEITY, AND MECHANICAL PROPERTIES IN LASER POWDER BED FUSED METALLIC ALLOYS: DESIGN, FABRICATION, AND EVALUATION" (2023). *Mechanical and Aerospace Engineering Dissertations*. 287.
https://mavmatrix.uta.edu/mechaerospace_dissertations/287

ENHANCING MICROSTRUCTURE, COMPOSITION HOMOGENEITY, AND MECHANICAL PROPERTIES IN LASER POWDER BED FUSED METALLIC ALLOYS: DESIGN, FABRICATION, AND EVALUATION

by

BEHZAD FARHANG

DISSERTATION

Submitted in partial fulfillment of the requirements
for the degree of Doctor of Philosophy at
The University of Texas at Arlington
May, 2023

Arlington, Texas

Supervising Committee:

Narges Shayesteh, Supervising Professor
Robert M. Taylor
Ankur Jain
Rassel Raihan
Yiran (Emma) Yang

This dissertation is dedicated to

my wife

who emotionally and financially supported me through all the stages of my Ph.D.

ACKNOWLEDGEMENTS

First and foremost, I would like to express my deepest gratitude to my advisor, Dr. Narges Shayesteh, for her unwavering support throughout my Ph.D. journey. My passion for researching material characterization of superalloys processed through metal additive manufacturing was a driving force that led me to join Dr. Shayesteh's Innovative Additive Manufacturing lab in January 2019. Her enthusiasm for research greatly inspired me, and her continuous encouragement bolstered my determination to achieve my academic goals. I am profoundly thankful for her patience, guidance, and the invaluable knowledge she imparted. Her supportive, understanding, and responsive nature has provided me with the opportunity to participate in numerous research projects without hesitation.

I would also like to extend my appreciation to Dr. Amir Ameri for his invaluable assistance and advice at every stage of the research projects and throughout the completion of my Ph.D.

My heartfelt thanks go to Professors Robert M. Taylor, Ankur Jain, Rassel Raihan, and Yiran (Emma) Yang for their time and effort in reviewing my thesis as part of the dissertation committee, as well as for their technical support during my studies.

I am sincerely grateful to my collaborators Aditya Krishna Ganesh Ram, Ahmet Alptug Tanrikulu, and former members of the IAM lab Bharath Bhushan Ravichander and Kiriti Mamidi for their significant contributions to my research projects.

Lastly, I would like to express my deepest gratitude to my wife, my parents, and my siblings, whose unwavering hope and belief in my success carried me through this journey. I could not have accomplished my academic goals without their constant support and encouragement. My wife has been my rock, providing emotional and financial support throughout the completion of this Ph.D. dissertation.

ABSTRACT

Enhancing Microstructure, Composition Homogeneity, and Mechanical Properties in Laser Powder Bed Fused Metallic Alloys: Design, Fabrication, and Evaluation

Behzad Farhang, Ph.D.

The University of Texas at Arlington, 2023

Supervising Professor: Narges Shayesteh

Over the past five decades, Nickel-based and Titanium-based alloys have become increasingly popular materials. As the manufacturing industry for these alloys has advanced, the demand for fabricating complex parts with enhanced mechanical properties at elevated temperatures has grown. Laser Powder Bed Fusion (LPBF), one of the most prevalent additive manufacturing techniques, has been employed successfully to produce these alloys. Nonetheless, there is still considerable effort being made to improve the microstructural, compositional, and mechanical properties of LPBF-processed components. In this study, we focused on adjusting the multi-scale microstructure and composition of LPBF-fabricated Nickel-based and Titanium-based alloys. The first objective of this study was to investigate the spatial variation of microstructure, composition, and metallurgical properties in LPBF-fabricated samples. Our findings revealed that the properties of LPBF-processed parts vary across different heat-affected areas due to differences in heat transfer modes. To regulate the cooling rate, we fabricated cubic samples surrounded by cubic borders in the second study. The results showed deeper melt pools in the samples fabricated with borders compared to those without. Additionally, we observed a lower level of porosity and higher hardness values in the samples surrounded by borders. In the third study, we aimed to find the optimal gap value between the main sample and the border by considering a wide range of gap values. According to our findings, the smallest gap value resulted in a more homogeneous microstructure, increased ductility, and greater tensile strength. Furthermore, we achieved in-situ microstructure adjustment through martensitic decomposition for the samples fabricated with borders. The method used in this study proved to be capable of expanding the possibilities for in-situ property optimization of LPBF-processed products, presenting an alternative solution to post-processing techniques.

LIST OF FIGURES

Figure 2.1.Transformation of NiTi alloy and its shape memory effect mechanism [37] 8

Figure 2.2.(a) Phase diagram of Ti64 alloy [56] (b) Effect of cooling rate on Ti64 phase transformation [57]. 11

Figure 2.3.Classification of Laser-Based Additive Manufacturing techniques [81-83]. 15

Figure 2.4.Powder bed-based AM techniques [84]. 16

Figure 3.1.SEM Micrographs of top view of grain structure of areas a) near the surface and b) away from the surface. 28

Figure 3.2.SEM Micrographs of side view of grains formed at areas located a) near the substrate and b) away from the substrate. 28

Figure 3.3.SEM Micrographs of top view of melt pools formed a) near the surface and b) away from the surface. 29

Figure 3.4.SEM Micrographs of side view of melt pools formed: a) near the substrate, b) away from the substrate, and c) magnified view of a region picked from the area away from the substrate. 30

Figure 3.5.Ni-rich precipitates observed in top surface of the sample at areas: a) near the surface b) away from the surface c) Both Ni-rich and Ti-rich precipitates found at an area near the surface. 31

Figure 3.6.Precipitates formed at an area near the substrate. 32

Figure 3.7.Top view SEM micrographs of defects including a) cracks formed near the surface b) magnified region at (a) c) a large crack formed at the surface. 33

Figure 3.8.a) an irregular-shaped defect formed away from the surface and b) magnified image of defect at (a). 34

Figure 3.9.SEM micrographs of a & b) cracks formed at the substrate, and c) un-melted area with impurities found near the substrate. 35

Figure 3.10.SEM micrographs of defects observed in the areas away from the substrate: a) small crack formed due to the precipitate b) crack formed with un-melted powders. 36

Figure 3.11.XRD spectrogram extracted from top surface of the sample shows presence of main and secondary phases at regions: a) near the surface b) away from the surface. 37

Figure 3.12.XRD spectrogram from side surface of the sample with a) presence of both Ni_2Ti and $NiTi_2$ secondary phases at area near the substrate b) Nitinol austenite and martensite without secondary phases at area away from the substrate 37

Figure 3.13.Microhardness results extracted from a) top surface and b) side surface (The highlighted planes in red color show the view direction). 38

Figure 4.1.Scanning electron microscope (SEM) micrograph of fresh powder; (b) particle size distribution of EOS supplied IN718 powder. 52

Figure 4.2.a) schematic of sample with border, b) infill and contour scan tracks for the main sample and border c) sample fabricated without border (reference sample) d) sample fabricated with border with 2 mm gap between the main sample and the border. 54

Figure 4.3.Optical microscopy of melt Pools for a) gap 0.5 sample b) gap 2.0 sample and c) reference sample. 56

Figure 4.4.Scanning electron microscopy of melt Pools for a) gap 0.5 sample 1 b) gap 2.0 sample and c) reference sapmle. 57

Figure 4.5.Scanning electron microscopy of columnar grains for a) gap 0.5 sample b) gap 2.0 sample and c) reference sample 58

Figure 4.6.Scanning electron microscopy of grains for a) gap 0.5 sample b) gap 2.0 sample and c) reference sapmle. 59

Figure 4.7.Porous areas formed for a) gap 0.5 sample b) gap 2.0 sample and c) reference sample 60

Figure 4.8.Precipitates formed in a) gap 0.5 sample b) gap 2.0 sample and c) reference sample (Numbers 1 to 4 correspond γ, γ″, MC carbide and Lave phases respectively) 61
Figure 4.9.The XRD diffractograms of a) gap 0.5 sample b) gap 2.0 sample and c) reference sample 62
Figure 4.10.The variation in (002) peak position in the XRD diffractograms extracted for three samples 63
Figure 4.11.Lattice constant of the γ phase extracted from the XRD diffractograms of the samples......... 64
Figure 4.12.The average value of the Vickers Hardness for three samples 64
Figure 4.13.Overlapping of melt pools results in formation of bigger pools (overlapped regions are highlighted) 66
Figure 5.1.Characterization of EOS Ti64 Grade 5 powder through (a) SEM micrograph and (b) particle size distribution analysis. 81
Figure 5.2.LPBF-built samples designed for (a) microstructural analysis and (b) tensile testing. 82
Figure 5.3.Schematic representation of tensile samples used in this study........ 83
Figure 5.4.Representative scanning electron microscopy (SEM) micrographs showing the distribution of pores for the a) Reference, and b) Gap 0.5 samples........ 86
Figure 5.5.Comparison of average porosity levels between samples fabricated with various gap distances between the sample and border, and the Reference sample. 86
Figure 5.6.Examining the correlation between pore size and gap distance between the sample and border, as compared to the Reference sample. 87
Figure 5.7.The evolution of different phases in the a) Reference and b) Gap 0.5 samples was analyzed using SEM images. The Reference sample mainly consisted of acicular α′ phase, while the Gap 0.5 sample contained a mixture of α + β basket-weave matrix, lamellar α, and acicular α′. 88
Figure 5.8.The comparison between border samples and the Reference sample reveals that the average thickness of α/α′ increases as the gap distance between the sample and border decreases. 88
Figure 5.9.X-Ray Diffraction (XRD) spectrographs for the samples, showing slight variations in the position of the main α/α′ peak. The largest discrepancy is observed between the Reference and Gap 0.5 samples. The β phase content is higher in the border samples, with the presence of an additional β phase peak at 2θ=57.5° in the Gap 0.5 sample indicating its highest content........ 90
Figure 5.10.The graph illustrates the variation in the average Vickers Hardness (HV) values plotted against the gap value. The results show a slight increase in microhardness as the gap value decreased from 4 to 0.5 mm. The Reference sample had the lowest microhardness value of 388 HV........ 92
Figure 5.11.Stress-strain plots for the Reference sample, Gap 0.5, Gap 1.0, and Gap 2.0 samples in uniaxial tensile testing. Gap 0.5 sample showed an approximately 15% and 9% improvement in UTS and fracture strain, respectively, compared to the Reference sample. 93
Figure 5.12.The DIC strain mappings corresponding to the frame before fracture extracted for a) Reference, b) Gap 0.5, c) Gap 1.0, and d) Gap 2.0 sample. The Gap 0.5 sample experienced a maximum local strain approximately 30% higher than that of the Reference sample and significantly higher than that of the Gap 1.0 and Gap 2.0 samples.. 94

LIST OF TABLES

Table 2.1.The phases commonly seen in IN718 [38]........ 8
Table 2.2.Different types of powder bed-based AM techniques [86]........ 17
Table 3.1.Melt pools dimensions extracted by Image J software for different areas of the samples........ 29
Table 4.1.The geometry and dimensions of the fabricated samples 53
Table 4.2.Melt pools dimensions extracted by Image J software for three samples........ 56
Table 5.1.Geometry and dimensions of fabricated samples. 82
Table 5.2.Comparing Vanadium Composition in α/α′ Phase: Various Samples. The vanadium percentage exhibited an increase with increasing gap value, but remained lower compared to the Reference sample.89
Table 5.3.Quantitative analysis of the XRD patterns with their possible corresponding microstructure. .. 91
Table 5.4.Parameters calculated from the XRD patterns for the Reference and Gap 0.5 samples. FWHM for Gap 0.5 sample was lower, indicating larger α/α′ phase size than Reference sample. No significant c/a variation observed, so XRD peak position deviation can be ignored. 91
Table 5.5.Tensile test parameters extracted from the stress-strain plots of the samples........ 93

TABLE OF CONTENTS

ACKNOWLEDGEMENTS iv

ABSTRACT v

LIST OF FIGURES vii

LIST OF TABLES ix

1. INTRODUCTION 1

  1.1. Motivation 1

  1.2. Objectives 2

  1.3. Approach 2

  1.4. Outline 3

  1.5. Contribution 3

2. BACKGROUND AND LITERATURE REVIEW 5

  2.1. Nickel-based and Titanium-based alloys 5
   2.1.1. History 5
   2.1.2. Ni-based alloys microstructure 7
   2.1.3. Ti-based alloys microstructure 9
   2.1.4. Conventional manufacturing of Ni-based and Ti-based alloys 11

  2.2. Metal Additive Manufacturing 12
   2.2.1. Introduction and History 12
   2.2.2. Advantages and Challenges 13
   2.2.3. Classification of Metal Additive Manufacturing Technology 14
    2.2.3.2. Powder bed-based technique 16

  2.5. References 17

3. SPATIAL VARIATION OF MICROSTRUCTURE, COMPOSITION, AND MECHANICAL PROPERTIES IN LPBF PROCESSED PARTS 23

  3.1. Introduction and overview 23

  3.2. Fabrication and experimental procedure 26
   3.2.1. Materials and fabrication 26
   3.2.2. Experiment method 26

  3.3. Results 27
   3.3.1. Microstructural analysis 27
    3.3.1.1. Grain structure and grain size 27
    3.3.1.2. Melt pools 29
    3.3.1.3. Precipitates 30
    3.3.1.4. Microstructure defects 32
   3.3.2. X-ray diffraction (XRD) analysis 36
   3.3.3. Microhardness analysis 38

  3.4. Discussion 39

  3.5. References 46

4. THE EVOLUTION OF MICROSTRUCTURE AND COMPOSITION HOMOGENEITY INDUCED BY BORDERS IN LASER POWDER BED FUSED PARTS 49

4.1. Introduction and overview 49

4.2. Materials and methods 52
4.2.1. Powder Preparation and Fabrication 52
4.2.2. Experimental Procedure 54

4.3. Results 55
4.3.1. Microstructure analysis 55
4.3.1.1. Melt Pools 55
4.3.1.2. Grain size and grain structure 57
4.3.1.3. Defects 59
4.3.1.4. Precipitates 60
4.3.2. X-Ray Diffraction (XRD) Analysis 61
4.3.3. Vickers Hardness 64

4.4. Discussion 64

4.5 References 73

5. INNOVAITIVE FABRICATION DESIGN FOR IN-SITU MARTENSITE DECOMPOSITION AND ENHANCED MECHANICAL PROPERTIES IN LASER POWDER BED FUSED Ti6Al4V ALLOY 78

5.1. Introduction and overview 78

5.2. Fabrication and Experimental Procedure 80

5.2.1. Powder Preparation and Fabrication 80

5.2.2.Experimental Procedure 83

5.3. Results 85
5.3.1. Microstructure analysis 85
5.3.1.1. Porosity Analysis 85
5.3.1.2. Lath Thickness Analysis 87
5.3.2. Compositional analysis 89
5.3.2.1. Energy Dispersive Spectroscopy (EDS) Analysis 89
5.3.2.2. X-Ray Diffraction (XRD) Analysis 89
5.3.3. Vickers Hardness 91
5.3.4. Mechanical properties 92

5.4. Discussion 94

5.5. References 100

6. CONCLUSIONS AND FUTURE WORKS 106

6.1. Conclusion 106

6.2. Future Work 107

1. INTRODUCTION

1.1. Motivation

Additive manufacturing (AM) has emerged as a highly versatile method for fabricating parts with intricate geometries. Utilizing AM techniques, near net shape dense parts with mechanical properties comparable to those of conventionally fabricated samples can be produced. However, structural defects and anisotropic behavior may arise in certain cases, necessitating optimization of the manufacturing process through vigilant material characterization.

Microstructural analysis is a comprehensive method employed to predict the properties of fabricated parts and identify the origin of defects, while compositional analysis provides insights into the phases present within the products. A strong correlation exists between the microstructure and composition of parts and their metallurgical and mechanical properties. In the context of AM, this relationship becomes even more complex and critical, as it directly influences the manufacturing process.

The microstructure and composition of AM parts are affected by various process parameters, encompassing energy source features (such as laser parameters), feedstock materials, layer thickness, fabrication atmosphere conditions (e.g., temperature), and process physics (including heat transfer modes). Consequently, the properties of the final part result from the interplay of all these process parameters, which collectively determine the microstructure and composition of the sample.

To optimize AM-produced parts, not only should laser process parameters be considered, but fabrication design and heat transfer conditions must also be accounted for during manufacturing. This study examines the microstructure, composition, and subsequent metallurgical and mechanical properties of parts fabricated using the Laser Powder Bed Fusion (LPBF) technique, a widely employed AM method. By concentrating on heat transfer conditions, the concepts and effects of fabrication parameters on the microstructure and composition of parts are discussed and evaluated.

The fabrication design is optimized by controlling the cooling rate and heat transfer modes, aiming to achieve a more homogeneous microstructure and composition throughout the part. This optimization leads to desired mechanical properties and a reduced level of defects, thereby significantly enhancing the quality and performance of LPBF-produced parts.

1.2. Objectives

This work primarily focuses on material characterization to manage the microstructural, compositional, and mechanical properties of samples fabricated using the LPBF technique on an EOS M290 metal 3D printer machine. Microstructural, compositional, and hardness analyses were performed on the fabricated parts to anticipate their mechanical properties, followed by mechanical testing to evaluate the validity of the results. In this study, three main objectives were pursued: (1) Investigate variations in microstructure and metallurgical properties across different heat-affected zones of LPBF-processed parts, aiming to understand the impact of these variations on the overall properties of the fabricated components. (2) Control the microstructure, composition, and metallurgical properties across the cross-section of the parts to ensure consistent quality and performance throughout. This objective encompasses understanding the relationship between process parameters and material properties, and leveraging this knowledge to create a more uniform distribution of properties within the part. (3) Implement in-situ optimization of microstructure, composition, metallurgical, and mechanical properties using a novel design for fabrication. This objective seeks to develop and apply innovative techniques for controlling and optimizing the properties of LPBF-produced parts during the fabrication process, ultimately enhancing the quality and performance of the final components.

1.3. Approach

In the beginning, a detailed literature review was conducted on the properties of Nickel-based and Titanium-based alloys. The LPBF method and its features compared to the conventionally manufacturing techniques was discussed in parallel. Following that a set of samples was fabricated using the LPBF technique. After the successful fabrication of the samples, microstructural and compositional tests were performed to investigate the variation of properties among different areas of the sample. Following that, microstructure and composition homogeneity across the cross section of the LPBF fabricated parts was evaluated by fabricating cubic borders surrounding the main samples. Similarly, optical and electron microscopy, X-ray diffraction analysis and hardness measurements were conducted on samples. Using the same methods and by extending the range of gap space between the border and main part, the in-situ microstructure and composition adjustment for the LPBF processed parts was investigated. Finally, mechanical testing was performed to support the effect of borders on the microstructural homogeneity level and elements distribution variation observed for the samples.

1.4. Outline

This study is organized into six chapters, beginning with Chapter 1, which presents the motivation, objectives, and approach of the investigation into the microstructural, compositional, and mechanical properties of samples fabricated using the LPBF technique. Chapter 2 provides a comprehensive literature review on Nickel-based and Titanium-based alloys, as well as an in-depth discussion of the LPBF method and its applications. In Chapter 3, the focus is on analyzing the spatial variation of microstructure, composition, and mechanical properties in LPBF fabricated parts. Chapter 4 delves into the evolution of microstructure and composition homogeneity across the cross-section of LPBF processed samples, examining the impact of processing parameters on homogeneity. Chapter 5 evaluates in-situ microstructure and composition optimization techniques for LPBF fabricated parts, including the presentation of mechanical testing results to validate optimization approaches. Finally, Chapter 6 concludes the study by summarizing the findings and offering recommendations for future research to complement and expand on the results presented in this work.

1.5. Contribution

Throughout the study, the following contributions will be made: (1) Gaining a comprehensive understanding of material characterization and the applications of microstructural, compositional, and mechanical analysis tests in the context of LPBF-fabricated parts. (2) Investigating variations in microstructure and metallurgical properties across the cross-section and height of LPBF fabricated parts, providing valuable insights into the factors influencing these properties and how they can be optimized. (3)

Implementing an innovative design in fabrication to achieve desired properties, along with a higher level of homogeneity in microstructure and composition for LPBF-manufactured parts. This will be accomplished by controlling the cooling rate and in-situ phase transformations, resulting in improved component quality and performance. (4) Performing mechanical testing on LPBF samples fabricated using the proposed method to validate the microstructural and compositional results, confirming the effectiveness of the optimized fabrication approach in enhancing the properties of the final parts.

2. BACKGROUND AND LITERATURE REVIEW

2.1. Nickel-based and Titanium-based alloys

2.1.1. History

Nickel-based (Ni-based) alloys are one of the widely-used superalloys known for their high strength and corrosion-resistance at elevated temperatures. They are usually comprised of several elements (up to ten) including carbon or boron or heavier elements such as tungsten, tantalum or rhenium. Due to maintaining their properties even at temperatures near their melting points, they are considered as suitable materials for high temperature applications. Because of this feature, Ni-based alloys have been employed in different industries such as aerospace, automotive and power generation applications since 1950s [1]. In this study, the focus would be on two widely used Ni-based alloys: Nickel-Titanium (NiTi) and Inconel 718.

NiTi, as one of the commonly-used Ni-based alloys, has been employed in many research studies and different industries. This alloy is formed of nearly equal atomic amount of Nickel (Ni) and Titanium (Ti) (49-51 mol percentage of Ni). Along with perfect mechanical properties, NiTi has unique features that has drawn much attention from researchers. The capability of recovering its original shape after deformation (known as shape memory properties), high level of superelasticity (returning to original state after unloading the plastic deformation) and good damping properties are specific mechanical properties can be found in NiTi. These features have made this alloy a perfect option to be used in biomedical applications and components like stents, guide wires, orthodontic wires and endodontic reamers [2, 3]. Due to its features, NiTi was chosen as one of the most-widely alloys to be studied in this research.

Developed by the International Nickel Company in 1960s, Inconel 718 (i.e., IN718) has been utilized as an age-hardening Ni-based superalloy [4, 5]. In addition to its good weldability properties, this superalloy is insensitive respect to the strain-age cracking. Due to its excellent mechanical and chemical properties at extremely low and high temperatures, an extensive range of working temperature (-257 °C to

704 °C) has been reported for IN718 [6-10]. Its high corrosion and creep resistant at elevated temperature (even close to the melting point) along with high strength accounts for a specific feature for this alloy [11, 12]. Because of these properties, IN718 has been widely employed in high temperature applications like gas turbines, combustion chambers, aircraft engines and nuclear power plants [5, 13, 14]. Moreover, as this alloy is comprised of high amount of economical elements such as Fe and Co, it is commonly used in the oil and gas industry [15-17]. This is why IN718 accounted for around 35% of all the superalloys produced in the 1980s and nowadays it is used in almost half of the engines [18]. For this reason, IN718 was selected as one of the Ni-based alloys for this study.

Titanium-based (Ti-based) alloys were first developed in 1940s to be used in aeronautical applications. It was about the same time that they were used in biomedical industry for the first time [19]. Due to their high specific strengths, Ti-based alloys are appropriate materials to be employed in aerospace applications. Except for the temperatures below 300 °C dominated by carbon fiber reinforced plastics, Ti-based alloys have the highest specific strength among all the commercial materials used for the high temperature conditions [20]. However, their remarkable features are not limited to the high temperature applications. Because of their excellent creep and corrosion resistance, low thermal coefficient of expansion, and their biocompatibility properties, they are also utilized in non-aerospace applications [20]. In this case, commercially pure Titanium (known as CPTi) and Ti-6Al-4V are two predominant Ti-based alloys which have been used in biomedical implants [19].

Ti-6Al-4V (known as Ti64), one of the most popular Ti-based alloys, accounts for almost the half of the market share of Titanium alloys utilized around the world today. This alloy was originally designed for aircraft applications in 1950s. Ti64 provides strength and lightness at the same time and therefore it is used in highly loaded structures to reduce the weight. In this case, Ti64 is employed in the components of gas turbines, jet engines and airframe structures [21-25]. Although, this alloy is mostly being used in aerospace applications, it has also been drawn the attention of automotive and biomedical industries during the 50 years ago [22-24, 26]. Ti64 is well-known for its lightness, high strength and corrosion resistance. These features along with its biocompatibility has made it a proper option for using in bridges and implants

[27-32]. Also, because of its resistance to most corrosive acids, Ti64 has applications in marine and chemical industries [31, 33-35]. Therefore, a part of this study will be on properties of Ti64 as one of the widely-employed Ti-based alloys.

2.1.2. Ni-based alloys microstructure

The microstructure of Ni-based alloys mainly depends on the phase compositions of these alloys. However, as the main element is Ni, the basic structure of Ni-based alloys is FCC with variation of other phases which form a multi-phase structure. In this case, formation of secondary phases like precipitation of γ' (Ni_3Al), γ'' (Ni_3Nb) and $Cr_{23}C_6$ among grain boundaries results in different properties and level of defects. In addition to Ni, these alloys may contain elements including a dozen of atomic components varying from 1% to more 50%. The mechanical properties, corrosion resistance and durability of Ni-based alloys are dependent of this multi-phase microstructure [36].

NiTi alloy, one of the commonly used Ni-based alloys, has a very narrow composition range, with nearly 1 to 1 atomic ratio. As a biomaterial, this alloy has a specific transformation temperature. The austenitic phase (A phase) forms at elevated temperature, with the phase corresponding to the lower temperature is called martensitic phase (M phase). As depicted in Figure 2.1(a), during the temperature reduction from A phase, the martensitic transformation starts at M_s (1) and the process of transformation is completed at M_f (2). Conversely, during the temperature rising from M phase, austenitic transformation starts at A_f (3) and the process finishes at A_f (4). From the crystal structure point of view, as shown in Figure 2.1(b), when the alloy is cooled in the A phase under M_s, it experiences transformation to the M phase with somewhat straining; however, the morphology is not changing. When the alloy experiences an external load, deformation occurs through formation of a twin, with the relative configuration of atoms is being kept. As a consequence, when the alloy is being heated again, the crystal structure returns to its original state and morphology. The properties of the NiTi alloy change based on the transformation temperature and it is then affected by the alloy composition, level of impurity, and its thermal history [37].

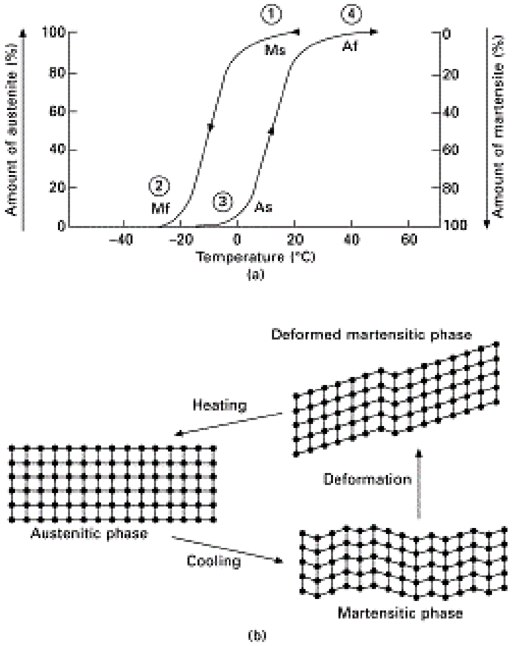

Figure 2.1.Transformation of NiTi alloy and its shape memory effect mechanism [37]

IN718, one of the other widely-used Ni-based alloys, is made of several elements including Ni as the main element and Chromium, Aluminum, Molybdenum, Titanium, Cobalt, and Niobium [38]. These phases can precipitate at different levels during the alloy processing and brings about desirable properties depending on the application requirements. The main phases of IN718 alloy are γ, γ', γ", δ, MC and laves, with their crystal structure and chemical composition being reported in table 2.1.

Table 2.1.The phases commonly seen in IN718 [38].

Phase	**Crystal structure**	**Chemical formula**
γ	Face Centered Cube	Ni
γ'	Face Centered Cube	Ni_3(Al, Ti)
γ"	Body-Centered Tetragonal	Ni_3Nb
δ	Orthorhombic	Ni_3Nb
MC	Cubic	(Nb,Ti)C
Laves	Hexagonal	$(Ni,Fe,Cr)_2(Nb,Mo,Ti)$

Among these phases, the gamma (γ) phase is the main phase of IN718 since it is made of Ni which forms matrix with the FCC crystal structure [39, 40]. However, the mechanical properties of IN718 is function of the secondary phases which are derived from the main γ phase. The gamma prime (γ') phase is one of the most important secondary phases of IN718 which with its FCC structure accounts for an strengthening phase of the alloy [41]. This phase stabilizes the alloy against dissolution through homogeneously precipitation in the matrix. Gamma double prime (γ") phase is the one of the other major secondary phases which strengthens the material with its BCC structure [42]. Among these two secondary phases, γ" phase has higher strengthening properties compared to γ′ phase [43]. Delta phase (δ) is the other secondary phases of IN718 which with its orthorhombic crystal structure accounts for a thermally stable phase of the alloy. It has been revealed that formation of this phase is detrimental for mechanical properties, as precipitation of this phase results in lower yield and tensile strength of the alloy [44, 45]. It should be noted that this phase also deteriorates the ductility of the alloy as well. However, low quantity of this phase is proved to be useful for improving the creep fracture resistance properties [39, 44, 46].

2.1.3. Ti-based alloys microstructure

Titanium has two main phases: α and β. Ti-based alloys can be categorized into α type, α+β type, or β type based on the composition of the alloy. α phase has hcp structure while β forms in BCC [47]. Reduction in α phase results in lower rigidity of the alloy, therefore Ti-based alloys with higher quantity of β phase are commonly used in trauma implants [48]. Titanium alloys with high quantity of β phase (such as Ti–29Nb–4.6Zr–13Ta, Ti-15Mo-5Zr-3Al, Ti–35Nb–7Zr–5Ta) have relatively high corrosion resistance and ductility in respect to the α+β type alloys [49, 50]. It has been revealed that the microstructure of α+β type Titanium alloys can be tailored to bring about Ti-based alloys with lower level of rigidity and superior mechanical properties for use in biomedical applications [51, 52].

Ti64, one of the (α + β) type Ti-based alloys, contains Al as the α stabilizer and V as the β stabilizer. When this alloys is processed through casting, the microstructure contains transformed β phase including acicular α phase and α phase formed at the prior β grain boundaries. However, the annealed Ti64 usually includes equiaxed α phase within intergranular β [53]. Since Al and V elements act as α and β stabilizer respectively, Ti64 alloy can provide a wide range of ductility and mechanical strength through adjusting the composition of this alloy.

Regradless of the manufacturing technique, the phase transformation in Ti64 accounts for the major factor which determines the properties of this alloy. In this case, thermal history and cooling rate induced by the manufacturing process specifies the decomposition and formation of the phases in Ti64 [54]. When the alloy undergoes a relatively fast cooling rate from temperatures above the β transus, β phase is decomposed to form the α + β matrices. If material experiences a higher cooling rate, then the resultant will be a fully martensitic microstructure known as needle shape α′ phase. This phase is one of the variants of α phase which provides high level of strength for this alloy [55].

The phase diagram of Ti64 alloy [56] is shown in Figure 2.2(a). During a complete melting and solidification process, Ti64 undergoes several phase transformations (α + β → β liquid→β → α + β/α′). As discussed, formation of fully martensitic α′ phase occurs through a specific thermal condition. When the cooling rate is fast enough and the temperature during manufacturing process is below the start temperature (Ms), the α′ phase forms in the microstructure. According to the previous studies, a range of the Ms temperature has been reported for Ti64 (from around 575 °C [57] up to 800 °C [53, 58]). This variation is due to the different initial thermal condition, composition and level of purity of the elements observed for Ti64, as these factors have impact on Ms temperature [53, 59]. This variation has also been reported for the the β transus temperature.

As it is illustrated in Figure 2.2(b), formation of α′ phase occurs only within a specific range of solidification rate [57]. When the solidification rate is higher than 410 °C/s, a fully martensitic microstructure forms. However, an incomplete formation of α′ phase happens when the cooling rate is lower but still higher than 20 °C/s, with no α′ phase forming under cooling rate lower than that [57]. Therefore, microstructure and mechanical properties of Ti64 alloy can be optimized through controlling the cooling rate which material experiences during the manufacturing process. For the cases that thermal conditions cannot be changed, post-treatment is a requirement for obtaining the desirable properties.

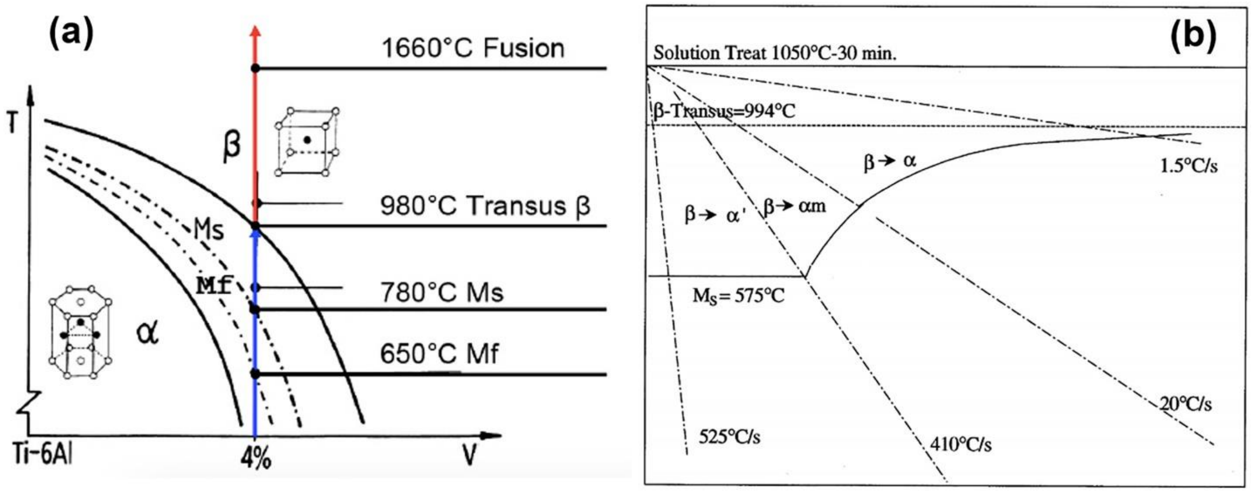

Figure 2.2.(a) Phase diagram of Ti64 alloy [56] (*b) Effect of cooling rate on Ti64 phase transformation* [57].

2.1.4. Conventional manufacturing of Ni-based and Ti-based alloys

Polycrystalline wrought alloys are considered as the first-generation Ni-based alloys. After developing the vacuum melting, cast Ni-based alloys became popular. With further progress in casting techniques, manufacturing of single-crystalline high-strength alloys was developed. Following that, powder metallurgy (PM) of Ni-base alloys was established during 1960s [60]. When it comes to the manufacturing of components that cannot be made through ingot metallurgy, conventional PM can be a proper option. In this case, hot isostatic pressing (HIP) following by forging is applied after PM when uniform grains and high level of homogeneity and density are needed [1]. It wasn't before 1908s when metal injection molding (MIM) of Ni-based alloys was introduced as a novel manufacturing technique [61]. MIM is a near-net shape process which can be used as an automated method for fabrication of Ni-based alloys in large quantities. By preventing the macro-segregation which usually occurs in other techniques, MIM provides parts with relatively good mechanical properties and uniform microstructure. Also compared to other conventional techniques, this method saves time and fabrication costs [1].

Although there are several manufacturing techniques that can be used for fabrication of Ni-based alloys, still some challenges and limitations exist in these methods. As mentioned in the previous section, Ni-based alloys have specific features which make them suitable for high temperature applications.

However, these properties also make them difficult-to-cut alloys as a high level of stress and temperature is generated during their machining process [62]. Compared to stainless steel, the machinability of Ni-based alloys is only 8 to 21% which brings about challenges in machining [63]. Another issue is that Nickel alloys undergoes work hardening during the machining process. Moreover, the machined surfaces show gummy and adhesive behavior for Nickel alloys [64]. These challenges have motivated manufacturers to use Additive Manufacturing (AM) techniques for fabrication of Ni-based alloys [65].

Manufacturing of Ti-based alloys (particularly Ti64), despite its high demand, is still a challenging process. Their low thermal conductivity [66], tendency to strain hardening [67, 68], and high chemical reaction with Oxygen [69] bring about difficulties in the fabrication process. These properties along with high-temperature strength, low Young's module, and high level of stress at the cutting tool edges make the Titanium alloys machining difficult. Generation of high temperatures, formation of buildup edges, and tool wearing occur during the machining process which thereby affect the quality of the final part [70]. Ti64 is one of the Ti-based alloys which can be processed through conventional manufacturing techniques. In this case, fabrication of Ti64 relies on casting, forging and rolling of bulk materials and therefore machining process is inevitable for the final shape of the products. As a result, waste of the material in large amount along with the high manufacturing costs and long processing time would be unavoidable [71, 72]. Under such circumstances, AM technology which offers advantageous capability for manufacturing of Ti64 components with shape complexities, would be the best solution [24, 71, 73].

2.2. Metal Additive Manufacturing

2.2.1. Introduction and History

Metal Additive Manufacturing (MAM) is an extremely promising method capable of fabricating complex geometries of metallic alloys as well as composites [74]. This manufacturing technique which is historically called rapid prototyping, includes several manufacturing technologies in which the materials are deposited layer by layer to form the final part [4]. The first step of MAM process is preparation a computer-aided design (CAD) model of the part. At the next step, the CAD model is sliced and stored usually in STL format and then is fed into the AM machine to be printed in successive layers and correct region [5]. Generally, there are four main components in the MAM process [6]:

1. A CAD model of the part
2. The raw materials which can be in smallest possible form of liquid droplets, wire, or mainly powder
3. A tool which is used to set the materials in the correct position
4. A digital system to control the tool which lays the materials layer-by-layer to form the geometry of the part.

These components utilized in the MAM process, result in a unique technique different from traditional formative or subtractive methods. This unique freedom in fabrication of single parts, alloys, composites and hybrid structures with even complex geometries arises from the layer-by-layer manufacturing method that can be controlled to provide high precision parts which is not achievable using the traditional processes. [11, 75]. However, it is not very long time that MAM techniques has been fully used in different industries from prototypes to products [15]. Nowadays, this manufacturing process is widely used in aerospace and automotive industry for fabrication of complex-shaped components [18, 76, 77], biomedical industry to build supporting devices like implants and prosthetic elements [38, 78-80], food and drug industry to manufacture equipment [6] and even international space stations to make parts and components [39].

2.2.2. Advantages and Challenges

MAM process, like other conventional manufacturing techniques, has its own benefits and drawbacks. Compared to the other methods, some of the advantages of MAM technique can be listed below [6]:

- Direct conversion of design to part
- Fabrication of parts with customization option and without need for any special tools or additional costs
- Producing complex geometries with internal features using a functional design
- Manufacturing of lightweight parts with lattice pattern or hollow structure

- Near net shape production of components with approximately no extra cost
- Efficient in manufacturing and minimum waste in raw materials
- A substantial reduction in manufacturing time which results in rapid transfer to market
- Capability of fabrication of various components due to less operational contribution
- On-demand fabrication
- Ability of scalability

However, there are still limitations in the speed of fabrication and reducing the manufacturing costs. In some cases, the required time to fabricate parts using MAM methods is still too long for mass production [15]. Also, although the quality and mechanical properties of the metal additive manufactured parts are comparable with conventional methods, MAM is still not the best option for fabrication of high-quality parts in special cases. Porosity is one major problem of metal additive manufactured parts and can affect the mechanical properties [40-42]. Therefore, as a manufacturing technique, improvement in the MAM processes is required to reduce the limitations and drawbacks. Understanding the concepts and physics of processes applied in MAM methods is the key to make considerable progress.

Based on the demand for manufacturing parts with complex geometries in high resolution, different MAM methods have been developed. Progress in fabrication of large parts with minimum defects and acceptable mechanical properties has been made by modification of MAM techniques and through introducing different methods [15].

2.2.3. Classification of Metal Additive Manufacturing Technology

Metal additive manufacturing (MAM) techniques can be categorized based on the source of the energy employed during the fabrication. Laser-based, ultrasonic-based, and electron-based methods account for the main MAM techniques. Laser-based MAM, which is the focus of this thesis, can be further classified into three main fabrication methods: powder-bed based, directed enrgy deposition, and sheet lamination. The detailed categories of each method is shown in Figure 2.3. Since the powder-bed based method has been employed to fabricate all the samples in this thesis, the focus will be on this technique.

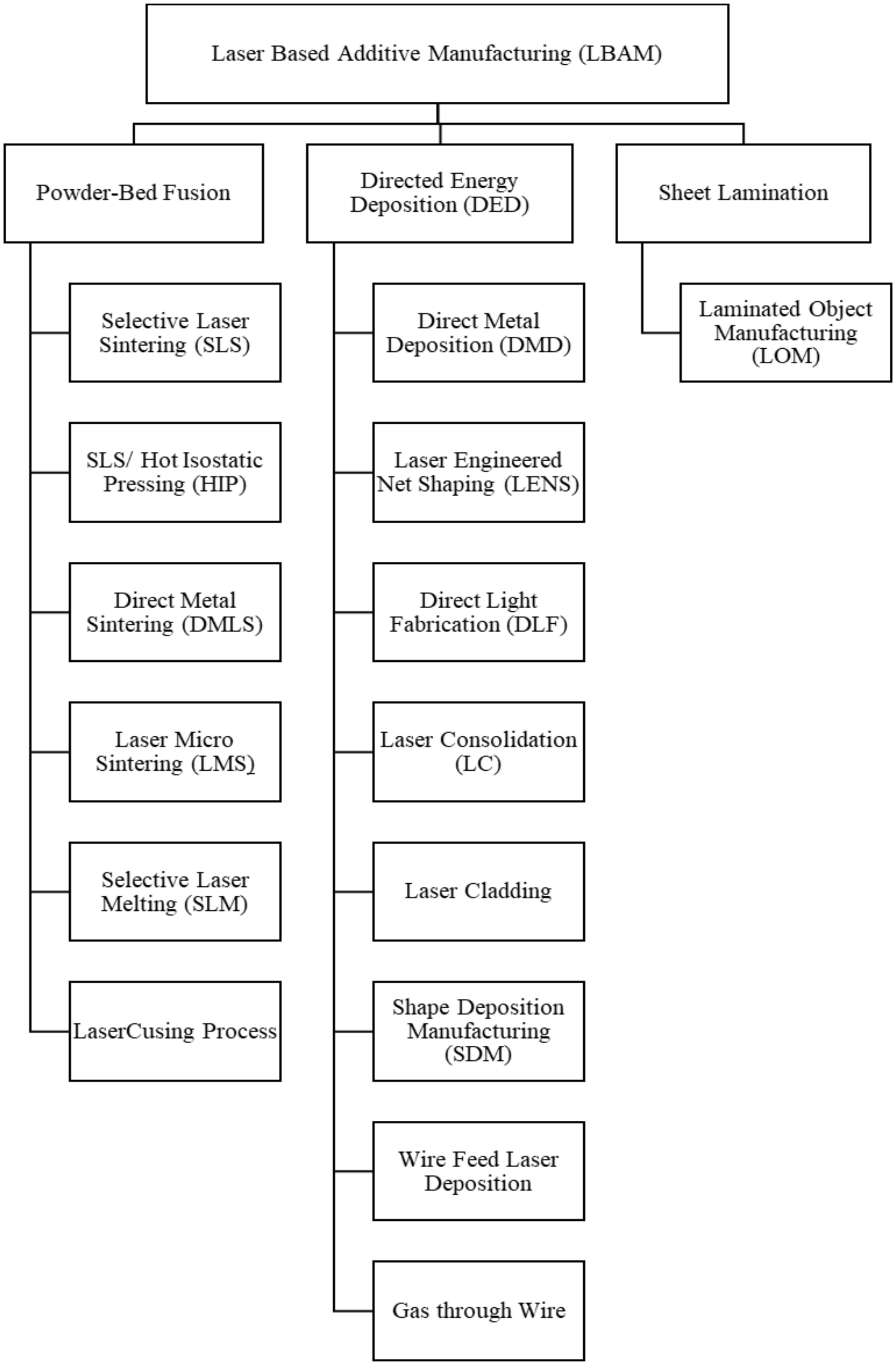

Figure 2.3.Classification of Laser-Based Additive Manufacturing techniques [81-83].

2.2.3.2. Powder bed-based technique

In powder bed-based technique, a recoater is used to distribute a layer of powder on the building plate. Then the powder is melted and fused by applying the laser power. The laser scans each layer of powder based on the computer-aided design (CAD) model of the part which is transferred to the machine. The unprocessed powder acts as a support for the next layer. The build plate drops dwon by one layer and a fresh layer of powder is distributed by the recoater. This process repeats layer by layer until the part is manufactured [84, 85]. A schemiatic of this manufactrung technique is illustrated in Figure 2.4, with all the main components being labeled on the figure. There are different types of powder bed-based methods which are commonly used to fabricate parts based on the application requirements. Selective laser sintering (SLS), Direct metal laser sintering (DMLS), Hot isostatic pressing (HIP), Laser micro sintering (LMS), and Selective laser melting (SLM) are considered as main powder bed-based techniques. Table 2.2 compares the capabilities and resolution of these techniques.

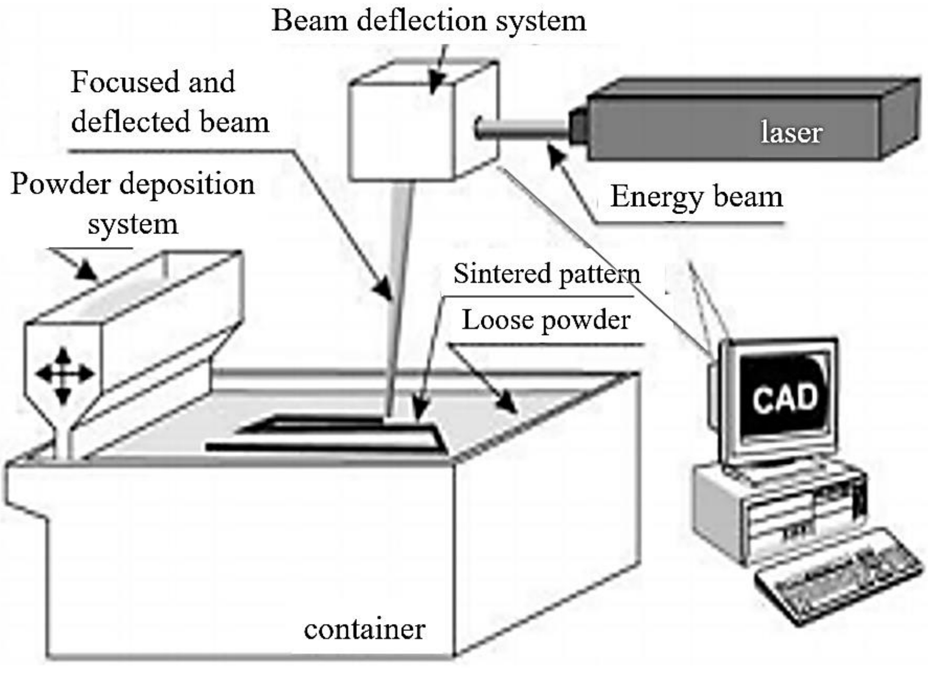

Figure 2.4.Powder bed-based AM techniques [84].

Table 2.2.Different types of powder bed-based AM techniques [86].

Powder-bed	Layer Thickness	Common Materials	Resolution	Laser type
SLS	100-300μm	Almost all metallic materials	> 100 μm	CO_2, Nd:YAG, fiber lasers, and disc lasers
SLS/HIP	100-300μm	Inconel 625 superalloy, Ti64	> 100 μm	CO_2, Nd:YAG, fiber lasers, and disc lasers
DMLS	20-50 μm	Steel alloys, stainless steel, tool steel, aluminum, bronze, cobalt-chrome, (Fe,Ni)–TiC composites and titanium	≈20 μm	CO_2, Fiber
LMS	1-10 μm	Steel, silver and copper	<30 μm	Q-switched Nd:YAG in TEM00 mode
SLM	20-100 μm	Stainless steels, aluminum, copper, iron, cobalt chrome, titanium, Ni-based alloy, and a mixture of different types of particles (Fe, Ni, Cu, and Fe_3P)	≈20 μm	Nd: YAG

In this study, we used an SLM 3D printer machine to fabricate Ni-based and Ti-based alloy samples. For the fabrication method, laser powder bed fusion (LPBF) terminology has been used throughout the text as it conveys the general manufacturing technique.

2.5. References

1. Horke, K., A. Meyer, and R.F. Singer, 24 - Metal injection molding (MIM) of nickel-base superalloys, in Handbook of Metal Injection Molding (Second Edition), D.F. Heaney, Editor. 2019, Woodhead Publishing. p. 575-608.

2. Hanawa, T., 1 - Overview of metals and applications, in Metals for Biomedical Devices, M. Niinomi, Editor. 2010, Woodhead Publishing. p. 3-24.

3. Safaei, K., et al. Controlling crystallographic texture and thermomechanical properties of NiTi shape memory alloy through laser powder bed fusion. in SMST2022. 2022. ASM International.

4. Zheng, L., et al., Mechanism of Intermediate Temperature Embrittlement of Ni and Ni-based Superalloys. Critical Reviews in Solid State and Materials Sciences, 2012. 37(3): p. 181-214.

5. Paulonis, D.F. and J.J. Schirra, Alloy 718 at Pratt & Whitney: Historical Perspective and Future Challenges. Vol. 1. 2001. 13-23.

6. Metals, S., Inconel alloy 718. Publication Number SMC-045. Special Metals Corporation, 2007.

7. Ravichander, B.B., et al., Experimental investigation of laser scan strategy on the microstructure and properties of Inconel 718 parts fabricated by laser powder bed fusion. Materials Characterization, 2022. 186: p. 111765.

8. Ravichander, B.B., et al. A Prediction Model for Additive Manufacturing of Inconel 718 Superalloy. Applied Sciences, 2021. 11, DOI: 10.3390/app11178010.

9. Vignesh, R.K.R., et al. Determination of residual stress for Inconel 718 samples fabricated through different scanning strategies in selective laser melting. in Proc.SPIE. 2020.

10. Ravichander, B.B., et al. Cost-Aware Design and Fabrication of New Support Structures in Laser Powder Bed Fusion: Microstructure and Metallurgical Properties. Applied Sciences, 2021. 11, DOI: 10.3390/app112110127.

11. Ardila, L.C., et al., Effect of IN718 Recycled Powder Reuse on Properties of Parts Manufactured by Means of Selective Laser Melting. Physics Procedia, 2014. 56: p. 99-107.

12. Ganesh-Ram, A., et al. Study on the microstructural and hardness variations of unsupported overhangs fabricated using selective laser melting. in Behavior and Mechanics of Multifunctional Materials XV. 2021. SPIE.

13. Farhang, B., et al. Investigating the Effect of Heat Transfer on the Homogenity in Microstructure and Properties of Inconel 718 Alloy Fabricated by Laser Powder Bed Fusion Technique. in 2021 International Solid Freeform Fabrication Symposium. 2021. University of Texas at Austin.

14. Hanumantha, M., et al. Microstructural and Mechanical Characterization of Laser Powder Bed Fusion of IN718 Overhangs. in 2021 International Solid Freeform Fabrication Symposium. 2021. University of Texas at Austin.

15. Brooks, J. and P. Bridges, Metallurgical stability of Inconel alloy 718. Superalloys, 1988. 88: p. 33-42.

16. Ramachandra, S., et al. Impact of Porosity Type on Microstructure and Mechanical Properties in Selectively Laser Melted IN718 Lattice Structures. in 2021 International Solid Freeform Fabrication Symposium. 2021. University of Texas at Austin.

17. Ravichander, B., et al. Investigation of the Properties of Reinforced IN718 Structures Fabricated using Laser Powder Bed Fusion. in 2021 International Solid Freeform Fabrication Symposium. 2021. University of Texas at Austin.

18. Loria, E.A., The status and prospects of alloy 718. Jom, 1988. 40(7): p. 36-41.

19. Hallab, N.J. and J.J. Jacobs, Chapter II.5.6 - Orthopedic Applications, in Biomaterials Science (Third Edition), B.D. Ratner, et al., Editors. 2013, Academic Press. p. 841-882.

20. Chattoraj, I., 10 - Stress corrosion cracking (SCC) and hydrogen-assisted cracking in titanium alloys, in Stress Corrosion Cracking, V.S. Raja and T. Shoji, Editors. 2011, Woodhead Publishing. p. 381-408.

21. Inagaki, I., et al., Application and features of titanium for the aerospace industry. Nippon steel & sumitomo metal technical report, 2014. 106(106): p. 22-27.

22. Boyer, R.R., An overview on the use of titanium in the aerospace industry. Materials Science and Engineering: A, 1996. 213(1): p. 103-114.

23. Singh, P., H. Pungotra, and N.S. Kalsi, On the characteristics of titanium alloys for the aircraft applications. Materials Today: Proceedings, 2017. 4(8): p. 8971-8982.

24. Uhlmann, E., et al., Additive Manufacturing of Titanium Alloy for Aircraft Components. Procedia CIRP, 2015. 35: p. 55-60.

25. Ganesh-Ram, A., et al. Study of Spatter Formation and Effect of Anti-Spatter Liquid in Laser Powder Bed Fusion Processed Ti-6Al-4V Samples. in 2021 International Solid Freeform Fabrication Symposium. 2021. University of Texas at Austin.

26. Waterman, N.A. and P. Dickens, Rapid Product Development in the USA, Europe and Japan. World Class Design to Manufacture, 1994. 1(3): p. 27-36.

27. Emmelmann, C., et al., Laser Additive Manufacturing of Modified Implant Surfaces with Osseointegrative Characteristics. Physics Procedia, 2011. 12: p. 375-384.

28. Emmelmann, C., et al., Laser Additive Manufacturing and Bionics: Redefining Lightweight Design. Physics Procedia, 2011. 12: p. 364-368.

29. Hao, Y.-L., S.-J. Li, and R. Yang, Biomedical titanium alloys and their additive manufacturing. Rare Metals, 2016. 35(9): p. 661-671.

30. Giannatsis, J. and V. Dedoussis, Additive fabrication technologies applied to medicine and health care: a review. The International Journal of Advanced Manufacturing Technology, 2009. 40(1): p. 116-127.

31. Cui, C., et al., Titanium alloy production technology, market prospects and industry development. Materials & Design, 2011. 32(3): p. 1684-1691.

32. Ciocca, L., et al., Direct metal laser sintering (DMLS) of a customized titanium mesh for prosthetically guided bone regeneration of atrophic maxillary arches. Medical & Biological Engineering & Computing, 2011. 49(11): p. 1347-1352.

33. Gurrappa, I., Characterization of titanium alloy Ti-6Al-4V for chemical, marine and industrial applications. Materials Characterization, 2003. 51(2): p. 131-139.

34. Oryshchenko, A.S., et al., Marine titanium alloys: Present and future. Inorganic Materials: Applied Research, 2015. 6(6): p. 571-579.

35. Gorynin, I.V., Titanium alloys for marine application. Materials Science and Engineering: A, 1999. 263(2): p. 112-116.

36. Pomeroy, M., Encyclopedia of Materials: Technical Ceramics and Glasses. 2021: Elsevier Science.

37. Nakano, T., 3 - Mechanical properties of metallic biomaterials, in Metals for Biomedical Devices, M. Niinomi, Editor. 2010, Woodhead Publishing. p. 71-98.

38. Deng, D., Additively Manufactured Inconel 718: Microstructures and Mechanical Properties. 2018: Department of Management and Engineering, Linköping University.

39. Donachie, M.J. and S.J. Donachie, Superalloys: A Technical Guide, 2nd Edition. 2002: ASM International.

40. Bowman, R. Superalloys: A primer and history. in 9th International Symposium on superalloys. 2000.

41. Seitz, B., METHODOLOGY FOR EFFICIENTLY ESTABLISHING PROCESSING-STRUCTURE-PROPERTY RELATIONSHIPS FOR ADDITIVE-MANUFACTURED AGE-HARDENED ALLOYS, in George W. Woodruff School of Mechanical Engineering. 2016, Georgia Institute of Technology.

42. Bhadeshia, H.K.D.H., Nickel Based Superalloys. 2016.

43. Oblak, J.M., D.F. Paulonis, and D.S. Duvall, Coherency strengthening in Ni base alloys hardened by DO_{22} γ' precipitates. Metallurgical Transactions, 1974.

44. Azadian, S., L.-Y. Wei, and R. Warren, Delta phase precipitation in Inconel 718. Materials Characterization, 2004. 53(1).

45. J.K.Hong, et al., Microstructures and mechanical properties of Inconel 718 welds by CO_2 laser welding. Journal of Materials Processing Technology, 2008. 201(1-3).

46. Sjoberg, G., N. Ingesten, and R. Carlson, Grain boundary δ-phase morphologies, carbides and notch rupture sensitivity of cast alloy 718. Superalloys, 1991. 718(625): p. 603-620.

47. Morinaga, M., 5 - Titanium Alloys, in A Quantum Approach to Alloy Design, M. Morinaga, Editor. 2019, Elsevier. p. 77-94.

48. Goharian, A. and M.R. Abdullah, 7 - Bioinert Metals (Stainless Steel, Titanium, Cobalt Chromium), in Trauma Plating Systems, A. Goharian, Editor. 2017, Elsevier. p. 115-142.

49. Taddei, E.B., et al., Production of new titanium alloy for orthopedic implants. Materials Science and Engineering: C, 2004. 24(5): p. 683-687.

50. Disegi, J.A., Titanium alloys for fracture fixation implants. Injury, 2000. 31: p. D14-D17.

51. Banerjee, R., S. Nag, and H.L. Fraser, A novel combinatorial approach to the development of beta titanium alloys for orthopaedic implants. Materials Science and Engineering: C, 2005. 25(3): p. 282-289.

52. Tanrikulu, A.A., Microstructure and Mechanical Properties of Additive Manufacturing Titanium Alloys After Thermal Processing. 2017, Portland State University: United States -- Oregon. p. 171.

53. Welsch, G., R. Boyer, and E.W. Collings, Materials Properties Handbook: Titanium Alloys. 1993: ASM International.

54. Banerjee, D. and J.C. Williams, Perspectives on Titanium Science and Technology. Acta Materialia, 2013. 61(3): p. 844-879.

55. Bae, C.-J., A.B. Diggs, and A. Ramachandran, 6 - Quantification and certification of additive manufacturing materials and processes, in Additive Manufacturing, J. Zhang and Y.-G. Jung, Editors. 2018, Butterworth-Heinemann. p. 181-213.

56. Ducato, A., et al. An Automated Visual Inspection System for the Classification of the Phases of Ti-6Al-4V Titanium Alloy. in Computer Analysis of Images and Patterns. 2013. Berlin, Heidelberg: Springer Berlin Heidelberg.

57. Ahmed, T. and H.J. Rack, Phase transformations during cooling in α+β titanium alloys. Materials Science and Engineering A-structural Materials Properties Microstructure and Processing, 1998. 243: p. 206-211.

58. Gil Mur, F.X., D. Rodríguez, and J.A. Planell, Influence of tempering temperature and time on the α′-Ti-6Al-4V martensite. Journal of Alloys and Compounds, 1996. 234(2): p. 287-289.

59. Reisgen, U., et al., Influence on martensite-start-temperature and volume expansion of low-transformation-temperature materials used for residual stress relief in beam welding. Materialwissenschaft und Werkstofftechnik, 2017. 48(12): p. 1276-1282.

60. Sims, C.T., N.S. Stoloff, and W.C. Hagel, Superalloys II / edited by Chester T. Sims, Norman S. Stoloff, William C. Hagel. 1987, New York: Wiley.

61. Diehl, W. and D. Stöver, Injection moulding of superalloys and intermetallic phases. Metal Powder Report, 1990. 45(5): p. 333-338.

62. Mali, H.S. and D.R. Unune, Machinability of Nickel-Based Superalloys: An Overview, in Reference Module in Materials Science and Materials Engineering. 2017, Elsevier.

63. Zhu, D., X. Zhang, and H. Ding, Tool wear characteristics in machining of nickel-based superalloys. International Journal of Machine Tools and Manufacture, 2013. 64: p. 60-77.

64. Evans, R., 2 - Selection and testing of metalworking fluids, in Metalworking Fluids (MWFs) for Cutting and Grinding, V.P. Astakhov and S. Joksch, Editors. 2012, Woodhead Publishing. p. 23-78.

65. Safaei, K., et al., The Build Orientation Dependency of NiTi Shape Memory Alloy Processed by Laser Powder Bed Fusion. Shape Memory and Superelasticity, 2022. 8(4): p. 265-276.

66. Parry, L., I.A. Ashcroft, and R.D. Wildman, Understanding the effect of laser scan strategy on residual stress in selective laser melting through thermo-mechanical simulation. Additive Manufacturing, 2016. 12: p. 1-15.

67. Gupta, R.K., et al., Strain hardening of Titanium alloy Ti6Al4V sheets with prior heat treatment and cold working. Materials Science and Engineering: A, 2016. 662: p. 537-550.

68. de Formanoir, C., et al., A strategy to improve the work-hardening behavior of Ti–6Al–4V parts produced by additive manufacturing. Materials Research Letters, 2017. 5(3): p. 201-208.

69. Prasad, A.V.S.R., K. Ramji, and G.L. Datta, An Experimental Study of Wire EDM on Ti-6Al-4V Alloy. Procedia Materials Science, 2014. 5: p. 2567-2576.

70. Hourmand, M., M.S. Uddin, and A.A.D. Sarhan, Processing of Titanium by Machining: A Closer Look Into Performance Metrics in Bio-Fabrications, in Reference Module in Materials Science and Materials Engineering. 2017, Elsevier.

71. Huang, R., et al., Energy and emissions saving potential of additive manufacturing: the case of lightweight aircraft components. Journal of Cleaner Production, 2016. 135: p. 1559-1570.

72. Lütjering, G. and J.C. Williams, Titanium. 2013: Springer Berlin Heidelberg.

73. Güden, M., et al., The quasi-static crush response of electron-beam-melt Ti6Al4V body-centred-cubic lattices: The effect of the number of cells, strut diameter and face sheet. Strain, 2022. 58(3): p. e12411.

74. Gökdağ, İ., et al., Design optimization and validation for additive manufacturing: a satellite bracket application. Structural and Multidisciplinary Optimization, 2022. 65(8): p. 237.

75. Reed, R.C., The superalloys: fundamentals and applications. 2008: Cambridge university press.

76. Patel, P., et al., Characterization of the effect of in-process annealing using a novel print head assembly on the ultimate tensile strength & toughness of Fused Filament Fabrication (FFF) parts. Virtual and Physical Prototyping, 2022. 17(4): p. 989-1005.

77. Ganesh Ram, A.K., Design and Optimization of Additively Manufactured Heat Sink and Heat Spreader for Microelectronics Cooling. 2019.

78. Patel, P.T., et al. Additive manufacturing of heterogeneous bio-Resorbable constructs for soft tissue applications. in Materials Science and Technology 2018, MS and T 2018. 2019. Association for Iron and Steel Technology, AISTECH.

79. Patel, P.T., Additive Manufacturing Process Investigation for the Fabrication of Composite Scaffolds for Soft Tissue Application. 2018: The University of Texas at Arlington.

80. Taylor, M.S., et al., Medical devices, uses and additive manufacture thereof. 2022, Google Patents.

81. Kruth, J.-P., et al., Consolidation phenomena in laser and powder-bed based layered manufacturing. CIRP annals, 2007. 56(2): p. 730-759.

82. Campbell, I., D. Bourell, and I. Gibson, Additive manufacturing: rapid prototyping comes of age. Rapid prototyping journal, 2012.

83. Hu, D., H. Mei, and R. Kovacevic, Improving solid freeform fabrication by laser-based additive manufacturing. Proceedings of the Institution of Mechanical Engineers, Part B: Journal of Engineering Manufacture, 2002. 216(9): p. 1253-1264.

84. Gibson, I., et al., Additive manufacturing technologies. Vol. 17. 2021: Springer.

85. Güden, M., et al., Orientation dependent tensile properties of a selective-laser-melt 316L stainless steel. Materials Science and Engineering: A, 2021. 824: p. 141808.

86. Moghaddam, N.S., et al., Recent advances in laser-based additive manufacturing. Laser-Based Additive Manufacturing of Metal Parts, 2017: p. 1-24.

3. SPATIAL VARIATION OF MICROSTRUCTURE, COMPOSITION, AND MECHANICAL PROPERTIES IN LPBF PROCESSED PARTS

3.1. Introduction and overview

Nickel–Titanium (NiTi) is part of a larger group of alloys appropriately named Shape Memory Alloys (SMA) that constitute metals that can recover their shape after large deformations up to 8% in the case of NiTi [1]. Due to various unique and advantageous properties including, high damping, corrosion resistance, excellent biocompatibility, ductility, and strength, NiTi has garnered attention in industries as widespread as biomedical, automotive, and aerospace [2–5,41,42]. However, the main limitation preventing the common use of NiTi in these industries is attributed to its poor workability due to its high strength, ductility, and high work hardening [1]. In facilitating the manufacturing of NiTi, many fabrication techniques have been used in the past to produce the alloy including casting and powder metallurgy, but both suffer from poor complexity and control of size and porosity of the finished part. With the growth of the field of additive manufacturing, this technology has become a clear contender for the fabrication of NiTi [6]. Additive manufacturing is a wide field with various technologies including powder bed, powder feed, and wire feed machines and techniques using these technologies including LPBF, Laser Engineering Net Shaping (LENS), and Electron Beam Additive Manufacturing (EBAM) [7]. LENS and EBAM offer reduced production times and greater mobility, but they also require increased post-process machining and do not meet the same tolerances of parts produced via LPBF [8]. As such, LPBF is the technology utilized to produce samples for this paper.

The mechanical properties of NiTi are strongly linked to microstructure properties including grain size and orientation, melt pool size, density of dislocations, and presence of defects such as porosity [6]. These microstructure features are of immense interest in the material science community and how each are affected by additive manufacturing processes such as LPBF. Of great importance is having an understanding of how the microstructure features affect the mechanical properties of NiTi. According to Watanabe et al. [9], the number of randomly oriented grain boundaries directly affects the propensity for a material to be brittle or ductile. More randomly oriented grain boundaries correlate with higher levels of brittleness while lower counts of randomly oriented grain boundaries correspond with more ductile materials due to the more difficult task of a crack traversing long boundaries at a time. Due to the number of instances of grains in a given part, larger grains that occupy more space will have lower amounts of grain boundaries while the opposite is true for smaller grains. Additionally, according to Frazier et al. [8], grain structures in LPBF-fabricated parts were found to be mostly columnar with epitaxial grain growth from the preceding fabrication layer. Kok et al. [10] attribute the anisotropic mechanical properties commonly found in additive manufacturing to this grain morphology noting an average loss in directional yield strength of approximately 5% when comparing tests performed in the build direction versus those performed perpendicular to the build direction. Bormann et al. [11] found that one of the printing parameters responsible for grain structure was the laser power. With increasing power, the grain structure became more elongated and structured as opposed to laser powers below 80 W producing grains with shorter, more random structures. Another aspect of LPBF that must be taken into consideration is manufacturing defects. Micro porosity is typically introduced via gas entrapment during the melting and cooling process [12]. Choong et al. [13], relates percentage of micro porosity present within a part to its ultimate tensile strength noting that there is a correlation between higher micro porosities and lower ultimate tensile strengths. Even the composition of the metal powder used in the LPBF process affects the resultant mechanical properties. Shiva et al. [14], found that of Ni55Ti45 (at.%), Ni50Ti50 (at.%), and Ni45Ti55 (at.%), the higher the composition of Titanium, the lower the value of the modulus of elasticity and ultimate tensile strength. Micro-precipitates formed through heated aging of NiTi were found by Karaca et al. [15], to have a significant effect on the transformation temperature and hardness. Higher values of transformation temperatures were found in specimens aged at lower temperatures versus those aged for the same time but at higher temperatures. Additionally, samples aged at a lower temperature were found to have a higher value of Vickers Hardness attribute to low density, coherent precipitate formation. Clearly, the process parameters of the LPBF technology need to manipulate these material properties to adapt to the desired attributes warranted by the application.

Although additive manufacturing as a whole has advanced the ability to produce NiTi parts, there are distinct differences between parts fabricated by conventional methods and those fabricated by additive manufacturing. This difference mainly lies in heterogeneity caused by layered fabrication and thermal gradation. Li et al. [16] found that the average temperature difference between the center of melt pools created by the laser of approximately 884 ˚C is only approximately 64.55 μm. Shayesteh Moghaddam et al. [17] attributed this temperature gradient to various heat transportation modes including conduction of heat throughout the powder bed, from the powder bed to the base plate, and convection of heat from the powder bed to the environment, typically flowing argon gas. Kok et al. [10] researched the specific anisotropic properties in additively manufactured parts. They specifically noted that the columnar and epitaxial grain growth found in LPBF parts is attributed to the build direction and more specifically due to the re-melting of the previous layer during the melting of the current layer of powder. These columnar grains were labeled as a factor in the anisotropic ductility values between vertical and horizontal directions based on the build orientation of the LPBF fabricated part. Even final material composition is a necessary consideration due to the evaporation found during the LPBF process. Bormann et al. [11] found that the amount of Ni evaporation was a function of exposure time, affected by the scanning speed of the laser. As exposure time increases, the amount of Ni evaporation increases but the rate of evaporation drops off as exposure time increases as well suggesting an exposure time dependency function for Ni evaporation. With these large variations in microstructural properties within an LPBF fabricated part, the understanding of these differences compared to conventional manufacturing methods is critical in efficient and effective designs.

The following study is the first of its kind in attempting to characterize the variations of microstructure properties throughout samples of NiTi fabricated by LPBF. To this end we had several samples fabricated with a single set of processing parameters. These samples were then cut and analyzed from the top view to observe the areas near and away from the edges. Similarly, observing the samples from the side, the areas near and away from the substrate were analyzed. Next, we evaluated several microstructural and metallurgical properties of the samples including grain structure, melt pools, precipitate formation, and defects such as cracks and un-melted powder. Through the use of Energy Dispersive XRay Spectroscopy (EDS), Secondary Electron Microscopy (SEM), X-ray Diffraction (XRD), and Vickers Hardness Tester, results were produced to detail the variations in each of the analyzed samples and to summarize the study and produce conclusions in the material properties.

3.2. Fabrication and experimental procedure

3.2.1. Materials and fabrication

An EOS M290 DMLS metal 3D printer (EOS GmbH Electro Optical Systems, Germany), equipped with a 400 W Ytterbium fiber laser, was employed for the LPBF fabrication of a series of specimens from pre-alloyed $Ni_{49.7}Ti_{50.3}$ at. % powder material. The overall dimensions of the test specimens were: length of 30 mm, width of 15 mm and height of 15 mm. For the current study, in order to produce LPBF NiTi parts, laser power (P) of 250 W, scanning speed (v) of 1.25 m/s, and hatch spacing (h) of 120 µm have been used to melt each layer of NiTi powders with 30 µm thickness (t). These LPBF processing parameters have been selected according to previous studies on the fabrication of LPBF $Ni_{50.1}Ti_{49.9}$ at.% [17] (Note: The slight difference in the material composition was neglected). The supplied energy from laser beam to volume of powder was calculated as 55.5 J/mm^3 using the energy density equation:

$$E_v = \frac{P_{nom}}{vhd}$$

Where Ev (J/mm^3) is the energy input, P_{nom} is nominal laser power, v (mm/s) is scanning speed, h (mm) is hatch distance and d (mm) is layer thickness.

3.2.2. Experiment method

A Hitachi S–3000 N Variable Pressure SEM microscopy was used to reveal the microstructure of the sample by producing all SEM and EDS tests in this study. For sample preparation, prior to mounting, the sample was ultrasonically cleaned, rinsed, and dried with compressed air to remove any oil or debris from sectioning or handling. Then, the LPBF fabricated sample was mounted on epoxy resin and hardeners. Grinding and polishing of sample were performed by Allied E-prep 4TM with power head in individual force mode. Grinding was conducted with a series of silicon carbide (SiC) abrasive discs (320–1200 Grit size). After each grinding step, the sample surface was inspected using the metallographic microscope XJP-H100 (Amscope, Irvine, CA) to ensure the scratch pattern was uniform. Removal of deformation caused by grinding was accomplished using 1 μm diamond suspension on DiaMat polishing cloth with GreenLube lubricant. Final polishing was performed with 0.04 μm colloidal silica suspension on a Chem-pol polishing cloth. To remove debris and abrasive particulates after each grinding and polishing step, the platen was wiped with water and spin-dried. The sample and fixture were cleaned with micro organic soap, rinsed with isopropyl alcohol, and then dried using compressed air spray. Before the microstructural analysis, the sample was etched by Kroll's Reagent (1–3 mL HF, 2–6 mL HNO3, 100 mL water). Crystal and compositional structures of the sample were determined using Bruker D8 Advance Xray diffractometer. The x-ray source was Cu k-alpha and measurements were made at room temperature with wavelength of 1.5406 Å, step intervals of 0.04˚ in 2Ɵ between 30˚ and 80˚ and speed of 1 s/step. The Vickers hardness of samples was measured by LECO LM 300 AT Micro Hardness Tester under 100 g loads which were applied for 10 s. At least 3 indentations were done to report the average number for each point.

3.3. Results

3.3.1. Microstructural analysis

3.3.1.1. Grain structure and grain size

Figure 3.1 a and b show SEM Micrographs focusing areas near the surface of the sample and away from the surface, respectively. In the area near the surface, equiaxed grains with smaller sizes of approximately 5 μm can be observed. However, as the focus moves towards the center of the sample, the grain size starts to increase. Looking at the area away from the surface, larger grains formed in cellular structure. The size of the grains can be found at the area away from the surface is approximately 5 times larger than those formed near the surface.

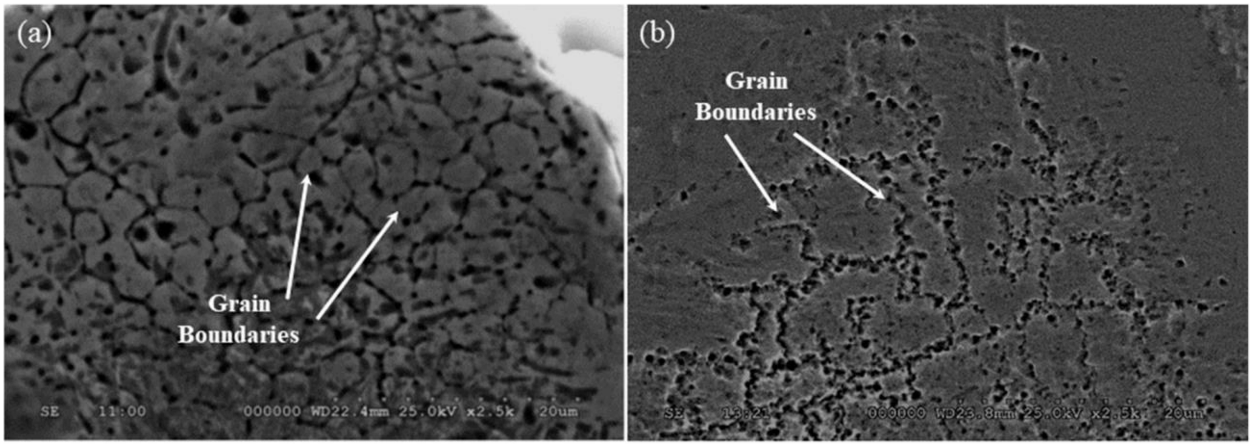

Figure 3.1.SEM Micrographs of top view of grain structure of areas a) near the surface and b) away from the surface.

When it comes to the side view, our observation is focused on two different areas, near and away from the substrate. Observing the area near the substrate, particularly at the melt pool boundaries, grains with more equiaxed structure were formed which are shown in Figure 6a. In contrast, looking at the region away from the substrate, a quite number of longer grains are visible at the melt pool boundaries (Figure 3.2). In this region, structure of grains tends to be more columnar as they are elongated parallel to the build direction and towards to the center of the melt pool. In terms of defects, the density of porosity among grains formed at the region near the substrate is significantly higher as against the area away from the substrate where no evidence of porosity can be found.

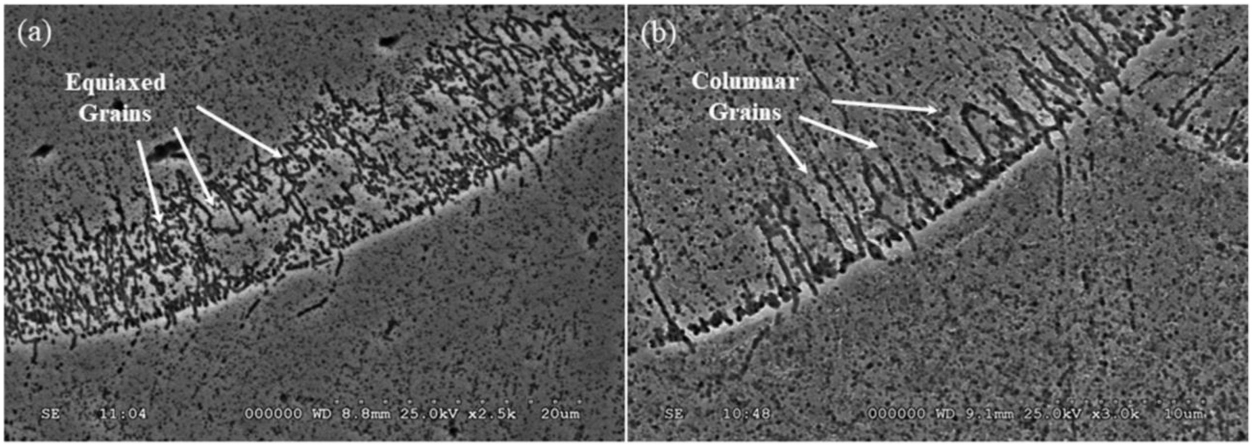

Figure 3.2.SEM Micrographs of side view of grains formed at areas located a) near the substrate and b) away from the substrate.

3.3.1.2. Melt pools

The top view of the sample shows cross-section of the melt pools formed during the LPBF process. As can be seen in Figure 3.3a, wider melt pools are formed at the area near the surface compared to those observed away from the surface, shown in Figure 3.3b. The density of defects was also found higher for the area away from the surface respect to the area near the surface. The dimensions of the pools were extracted using the scales of the images and ImageJ, an open-source image analysis software. Table 3.1 provides the width and depth of the pools for regions near and away from the substrate. It should be noted that the widest portion of the melt pools were used for the measurements. Based on the dimensions, the ratio of the width for pools near the surface to those found away from the surface was calculated as 1.45.

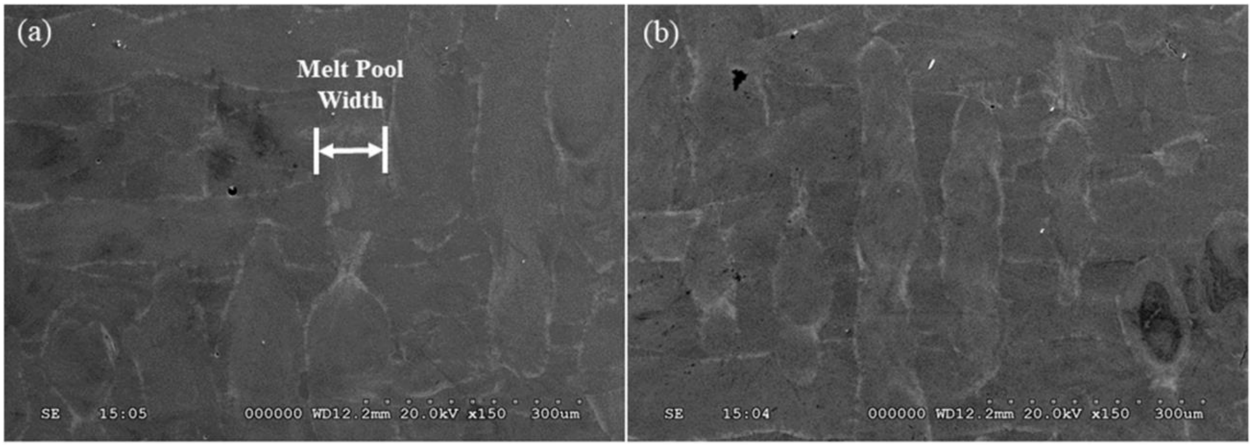

Figure 3.3.SEM Micrographs of top view of melt pools formed a) near the surface and b) away from the surface.

Table 3.1.Melt pools dimensions extracted by Image J *software for different areas of the samples*

	Near the surface	Away from the surface
Average Melt Pool Width (µm)	115	79
	Near the substrate	Away form the substrate
Average Melt Pool Depth (µm)	31	46

Focusing on side view, the depth of the melt pools can be evaluated. Pools formed at area away from the substrate (Figure 3.4b) were found to be deeper with 1.48 times deeper than those observed near the substrate (Figure 3.4a). The formation of columnar grains was observed within each melt pool. A magnified view of a region picked from the area away from the substrate is shown in Figure 8c. As mentioned, we elongated grains formed between the melt pool boundaries are visible. Unlike those found in the top view, the overlapping between melt pools can be seen in the side view when penetration through the lower layers occurs.

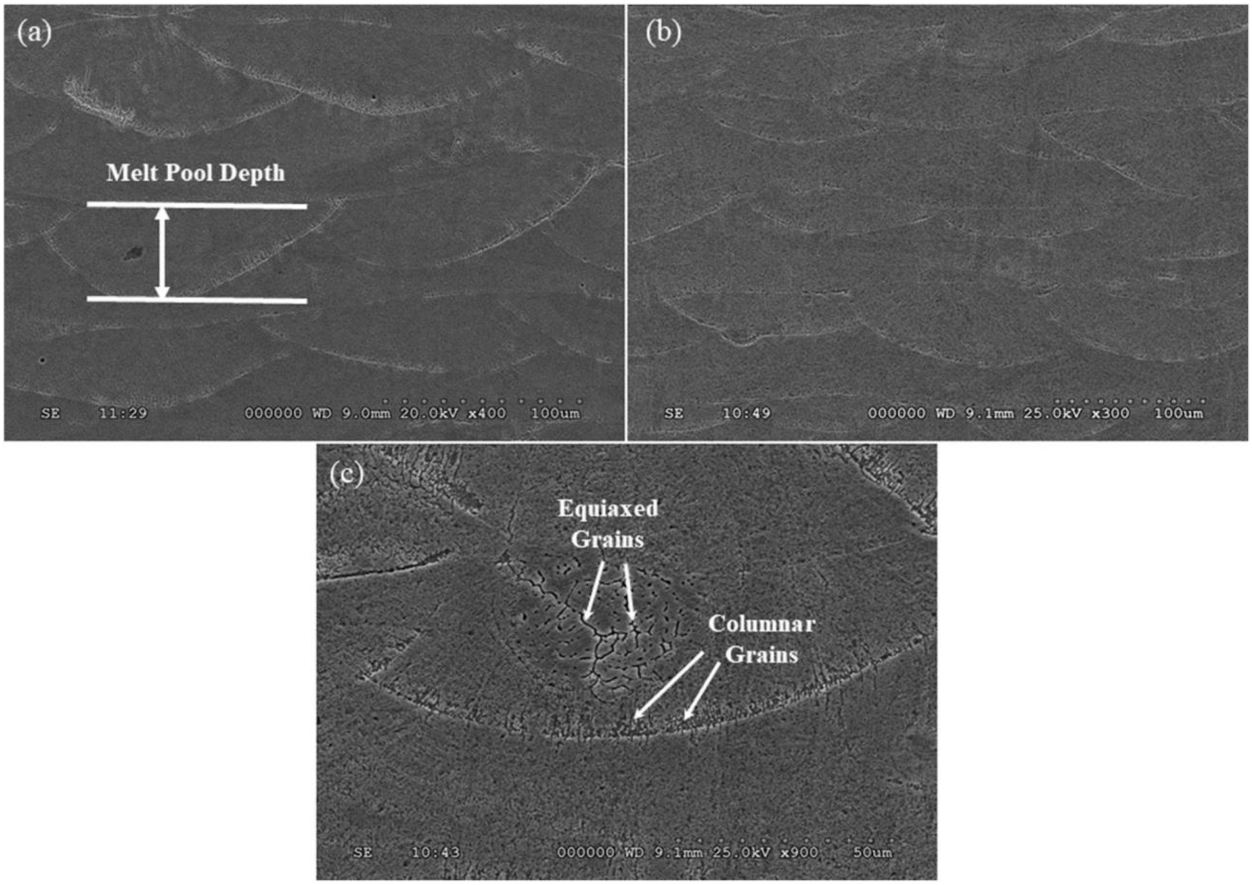

Figure 3.4.SEM Micrographs of side view of melt pools formed: a) near the substrate, b) away from the substrate, and c) magnified view of a region picked from the area away from the substrate.

3.3.1.3. Precipitates

Figure 3.5 shows precipitates formed in regions near and away from the surface when viewed from the top of the sample. Ni-rich (Ni_2Ti) precipitates were observed in both regions near and away the surface as shown in Figure 3.5 a and b, respectively. However, larger precipitates were found in areas near the surface compared to areas away the surface. When it comes to the Ti-rich (Ti_2Ni) precipitates, they are found only in the areas near the surface. Figure 3.5c clearly shows both Ni-rich and Ti-rich precipitates in an area near the surface providing the size comparison between the two with Ni-rich and Ti-rich precipitates shown in white and black respectively.

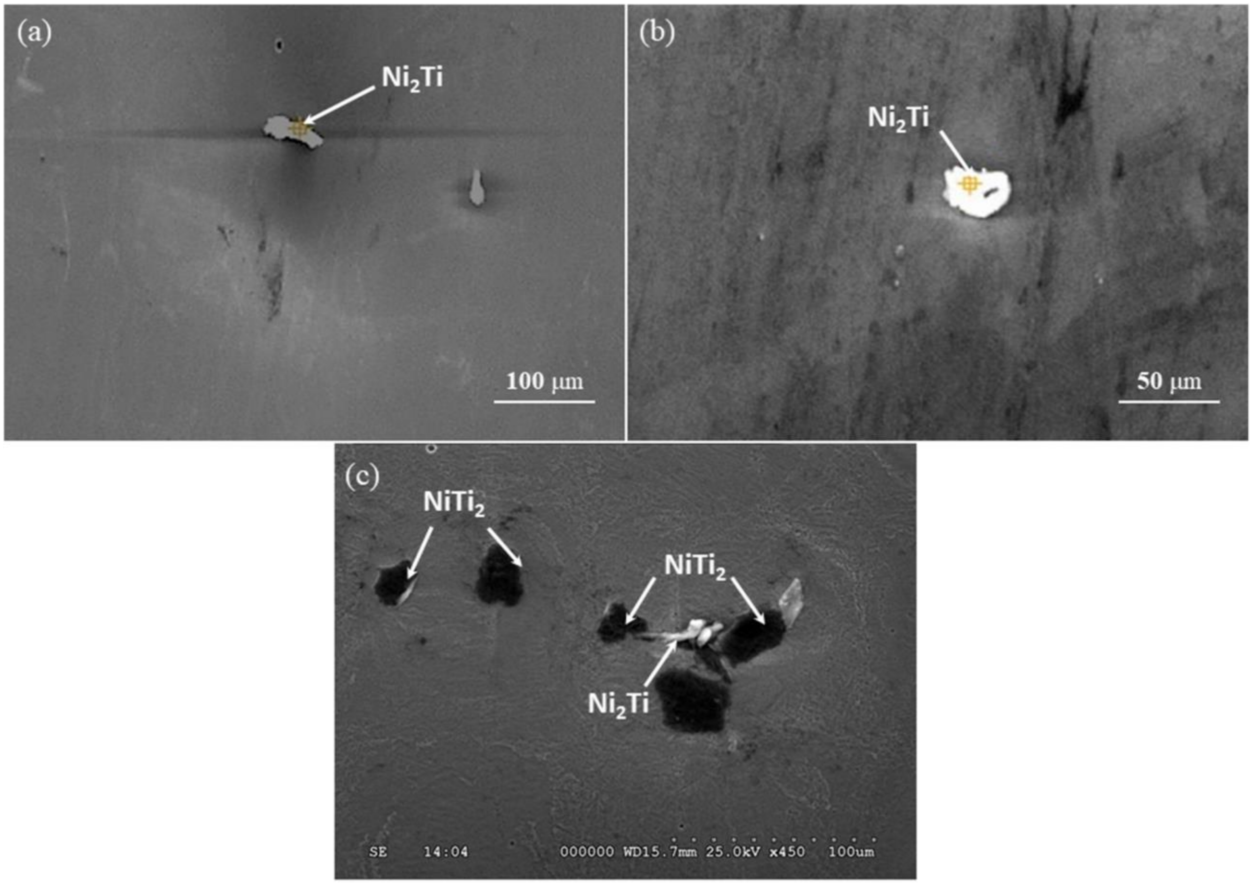

Figure 3.5.Ni-rich precipitates observed in top surface of the sample at areas: a) near the surface b) away from the surface c) Both Ni-rich and Ti-rich precipitates found at an area near the surface.

The same precipitates were found when viewed from the side of the sample. Like the area near the surface, both Ni-rich and Ti-rich precipitates were observed at the region near the substrate (Figure 3.6). The highest congestion of precipitates was found in this region compared to the other areas. On the other hand, the congestion of precipitates was insignificant for regions away from the substrate.

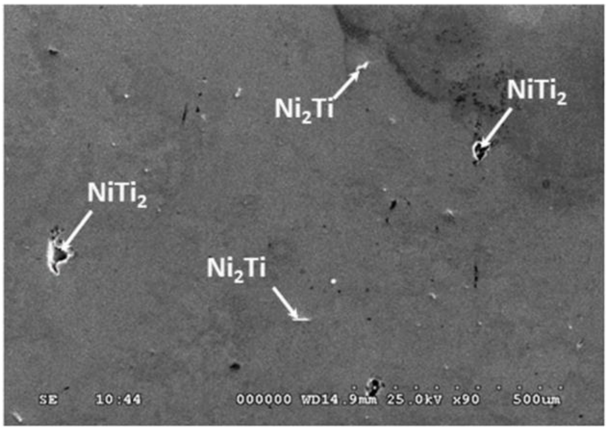

Figure 3.6.Precipitates formed at an area near the substrate.

3.3.1.4. Microstructure defects

Figure 3.7 shows different kinds of defect including small and large cracks near the surface of the sample when viewed from the top. Cracks formed at the area near the surface are found to derivate from disparate origins. As shown in Figure 3.7a, rough surfaces with small cracks are formed in the area near the surface. A magnified image from the area near the surface shows the crack initiated right at the surface and then propagated in different directions. On the other hand, a deeper crack was formed without any sign of propagation from the surface with smaller cracks being observed in the vicinity of this larger crack (Figure 3.7b). According to the scale of the picture, the average length of the visible cracks in this area is roughly 15 µm. Figure 3.7c shows an example of a large crack observed at the surface with the length of the crack being found to be approximately 100 µm. Additionally, crack growth in this region was found to have deeper sections on the side near the surface filled with un-melted powder.

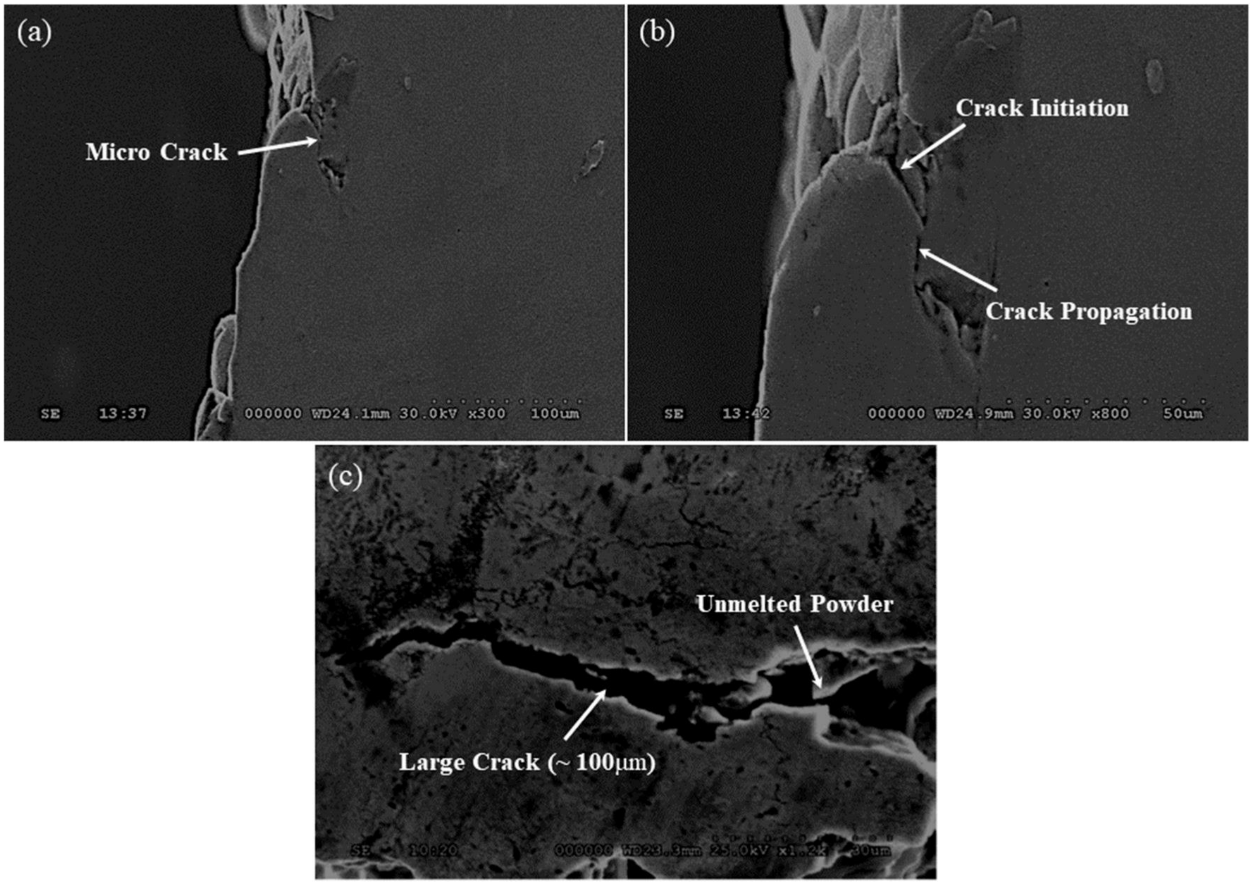

Figure 3.7.Top view SEM micrographs of defects including a) cracks formed near the surface b) magnified region at (a) c) a large crack formed at the surface.

Less number of defects observed in areas away from the surface compared to the regions near the surface. An example of an un-melted region formed in the area away from the surface shown in Figure 3.8a with Figure 3.8b showing a magnified view of the defect. As can be seen, narrow holes located around the deformation formed a small gap. One can infer that due to the irregular shape of the defect, it is originated from the process parameters applied during the fabrication. However, it should be noted that no large crack was observed in areas away from the surface.

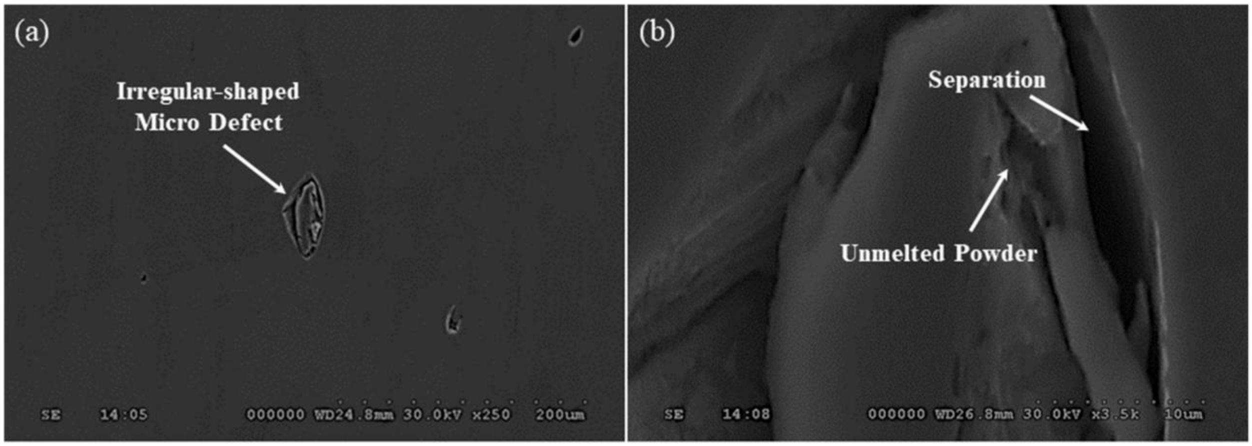

Figure 3.8.a) an irregular-shaped defect formed away from the surface and b) magnified image of defect at (a).

The defects formed at areas near and away from the substrate can be compared by looking at the side view shown in Figures 3.9 and 3.10 where much more precipitates found near the substrate. As can be seen, cracks with the length of more than 100 μm formed near the substrate while the origins of the cracks were found to be different from each other. As shown in Figure 3.9a, existence of defects plays an important role in growth of the crack propagated from the surface of the sample toward the middle area. In contrast, the origin of the crack shown in Figure 3.9b is different as it does not originate right at the surface and a gap between crack and the un-melted region can be seen. It should be noted that regardless of origin of cracks, the small cracks can be seen in both figures are indicative of the improper quality and high tendency for the formation of cracks near the substrate. Besides cracks, formation of numerous defects in some regions can be attributed to the leftover un-melted powders formed in those areas. A case in point is lack of fusion defects which are originated from partially melted areas. Figure 3.9c represents a huge un-melted region at the substrate where high density of impurities and un-melted powders are typically found.

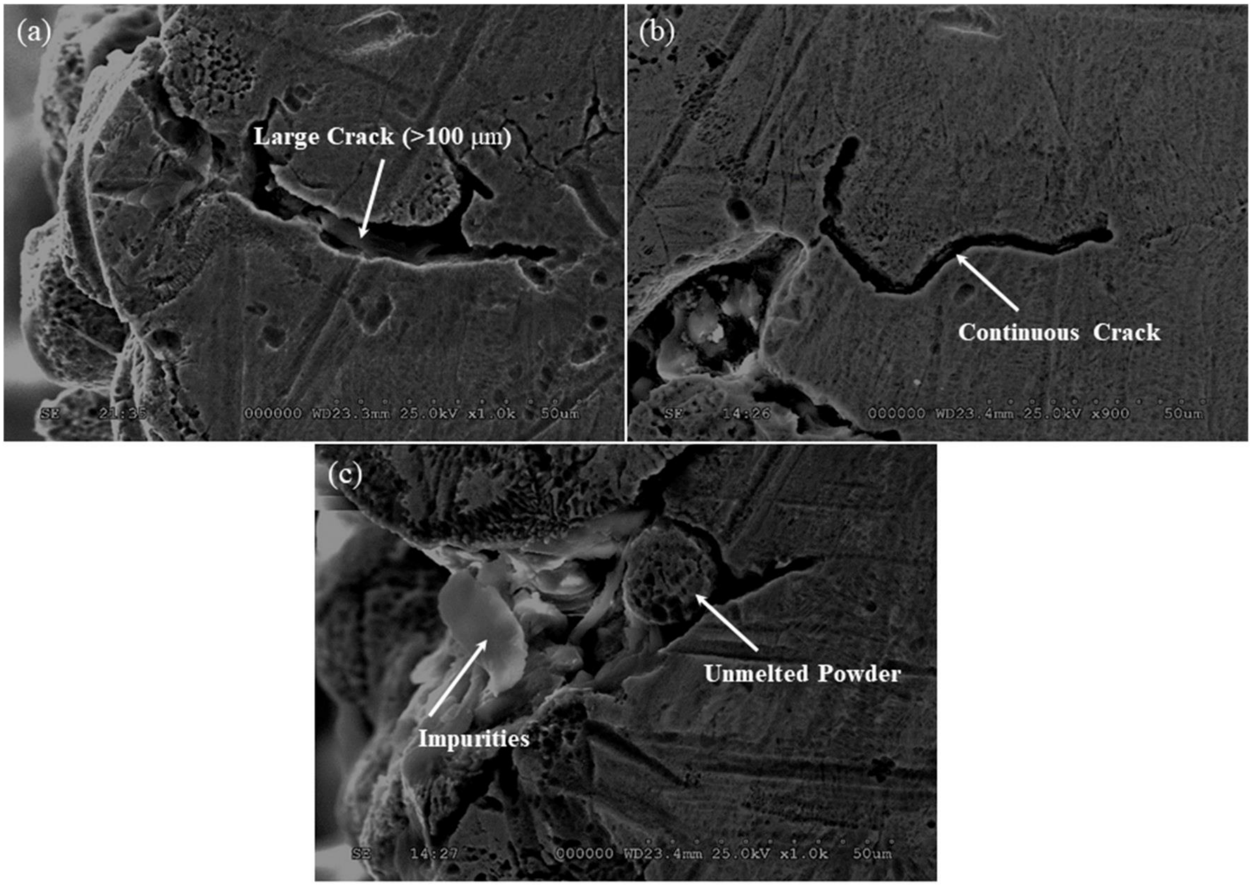

Figure 3.9.SEM micrographs of a & b) cracks formed at the substrate, and c) un-melted area with impurities found near the substrate.

In comparison, the number of defects observed far from the substrate was significantly lower. Defects observed in this area are shown in Figure 3.10 where considerably higher quality with significantly less number of defects were seen. Moreover, based on the defects observed, the length of the cracks in this area (Figure 3.10a) is relatively lower than ones formed in the region near the substrate. Furthermore, it is evident that the cracks formed in the area away from the substrate are not as deep as of these formed near the substrate as the previously fabricated layers can be easily seen for these cracks. Un-melted areas are more scarce in regions away from the substrate, however, cracks initiated from un-melted areas were observed in a few cases (Figure 3.10b). The length of the cracks and the density of defects found in the area away from the substrate are markedly lower compared to those found at areas near the substrate. Upon further investigation, it can be concluded that the formation of precipitates can result in the initiation of other defects like cracks.

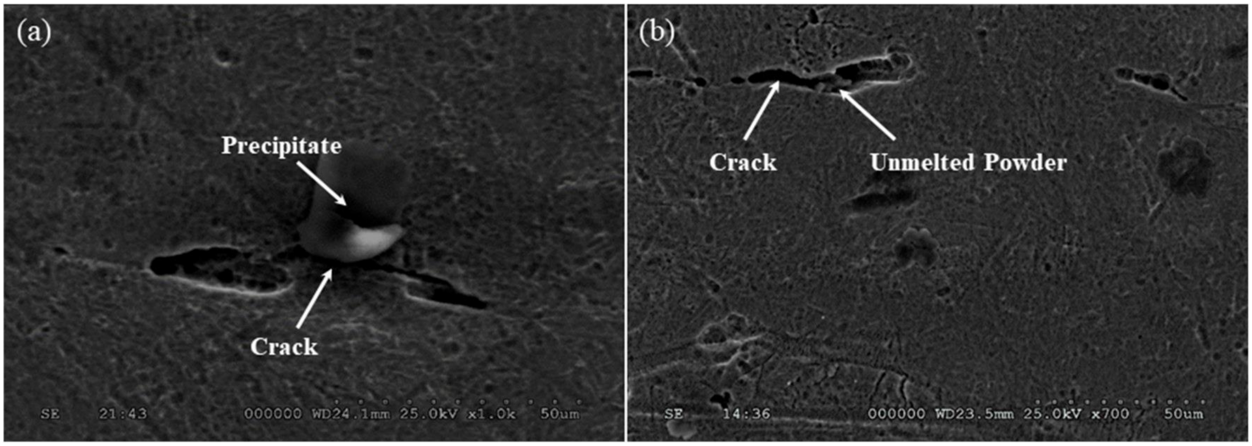

Figure 3.10.SEM micrographs of defects observed in the areas away from the substrate: a) small crack formed due to the precipitate b) crack formed with un-melted powders.

3.3.2. X-ray diffraction (XRD) analysis

The XRD spectrogram extracted from the top surface of the sample is shown in Figure 3.11. While presence of NiTi austenite and martensite with Ni_2Ti and $NiTi_2$ secondary phases were observed, there is no sign of formation of other intermetallic phases (Ni_3Ti, $NiTi_3$, Ni_4Ti_3). Moreover, no peaks associated to free titanium or nickel were found. Figure 3.11a represents the result for the region near the surface. According to this spectrogram, it is possible to have Ni_2Ti and $NiTi_2$ phases formed in this area with these secondary phases sharing properties and structures with the main NiTi phase. Nitinol proper alloy most likely includes two phases; an austenitic and a martensite phase with cubic lattice and monoclinic lattice structures respectively. When it comes to the area away from the surface, the composition is more uniform as fewer precipitates limited to only Ni_2Ti secondary phase can be observed. Although the sharpest peak belongs to the austenite phase again, the presence of martensite phase is considerably higher since the intensity of the monoclinic phase is markedly higher than that of the area near the surface.

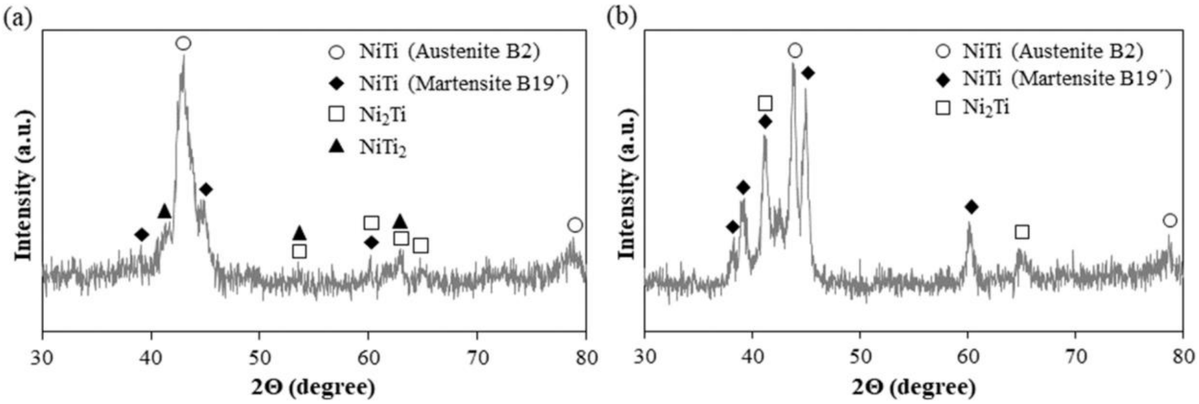

Figure 3.11.XRD spectrogram extracted from top surface of the sample shows presence of main and secondary phases at regions: a) near the surface b) away from the surface.

Looking into the side surface of the sample, we focus on two areas; near the substrate and away from it. The area near the substrate showed the similar pattern observed for the area near the surface in top view with both Ni_2Ti and $NiTi_2$ intermetallic phases being found for this region (Figure 3.12a). However, as can be seen in Figure 3.12b, only the main austenite and martensite phases were found for the area away from the substrate with no indication of formation of secondary phases. The proportion of these main phases is found to be similar to the ratio observed for the area near the surface of the top view.

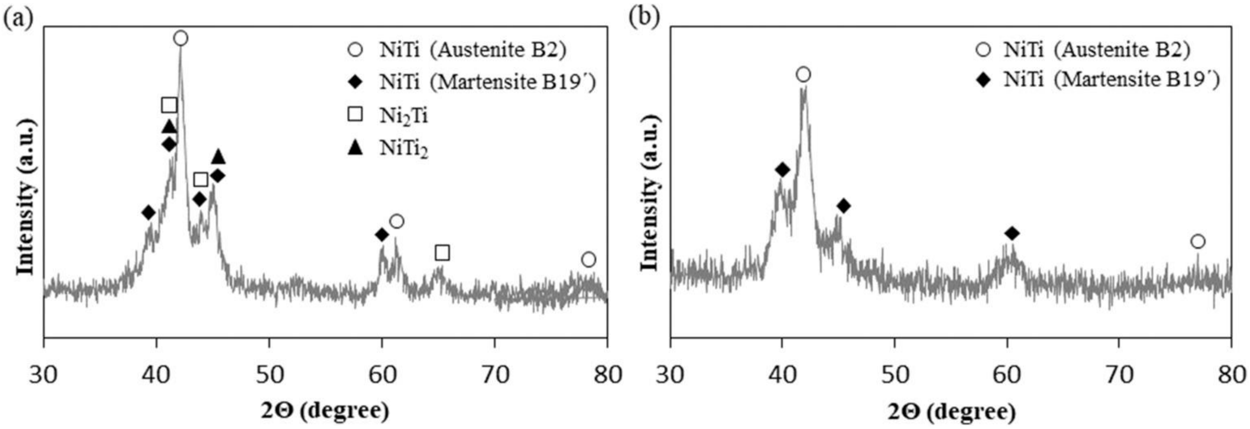

Figure 3.12.XRD spectrogram from side surface of the sample with a) presence of both Ni_2Ti and $NiTi_2$ secondary phases at area near the substrate b) Nitinol austenite and martensite without secondary phases at area away from the substrate

3.3.3. Microhardness analysis

Figure 3.13a and b provides Vickers Hardness values extracted from the top and side surface of the sample, respectively. 28 different points of each surface (top and side) was selected for indentation test in order to cover various regions of the sample. Looking into Figure 3.13a, it is evident that, regardless of some minor fluctuations, a trend can be observed between the data collected. The highest hardness value of 560 belongs to the point located in vicinity of the center of the sample, while the point near the surface shows a considerably lower value of 259 with the lowest hardness being observed for the point located near the corner with a value of 235.

Looking to the Figure 3.13b, we can compare the hardness values along the building direction. As can be seen, the minimum hardness values occur at points near the substrate, whereas an upward trend is visible as one moves along the building direction. The maximum value is found to be occurred at the center of the sample where harness value reaches to the peak of 560 with a downward trend being seen as moving towards the top surface of the sample. However, this trend ending at top surface shows higher values for this area (303 HV) compared to ones observed for points near the substrate (220 HV).

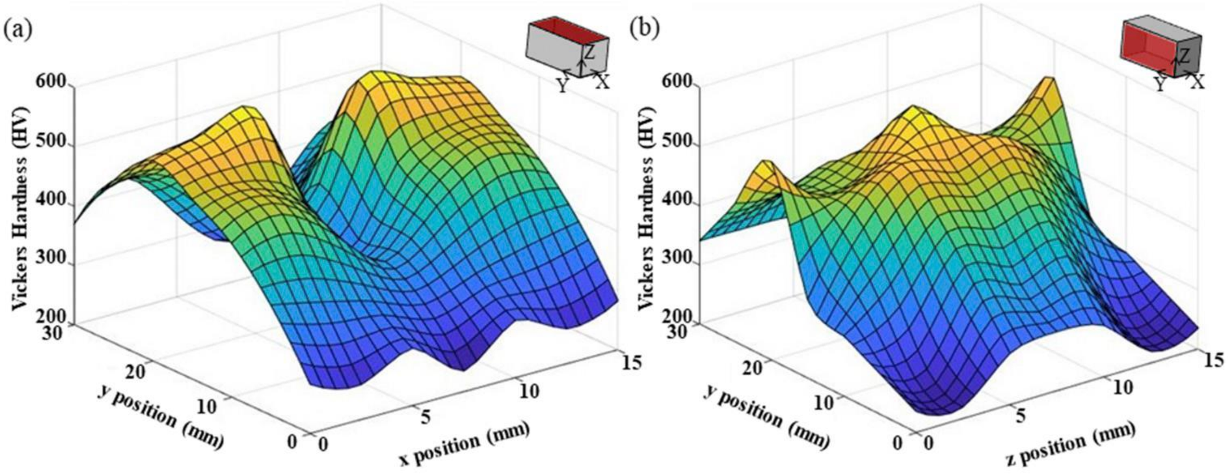

Figure 3.13.Microhardness results extracted from a) top surface and b) side surface (The highlighted planes in red color show the view direction).

3.4. Discussion

This study investigates the variation in microstructural and metallurgical properties in different areas of sample fabricated through the LPBF method. Results were extracted from the plane perpendicular (top view) and parallel (side view) to the build direction. In the top view, the areas near and away from the surface were investigated, while areas near and away from the substrate were analyzed for the side view.

In this study, the variation in grain size and structure in the two planes (perpendicular and parallel to the build direction) are observed. In the top view, smaller grains with an equiaxed structure were found in the area near the surface compared to larger grains observed in areas away from the surface. This observation can be attributed to the difference in cooling rate which accounts for the main criteria for grain size where higher cooling rate results in shorter growth time bringing about smaller grains and vice versa [18]. For layers near the surface, the associated cooling rate is higher due to its method of heat transfer. At the surface, these layers have a higher rate of heat transfer due to the significant role of convection and conduction as well. However, for the layers away from the surface, conduction is the dominant mechanism for heat transfer and the portion of convection drops substantially, thus the cooling rate is not as high as the layers found closer to the surface. Therefore, because of lower local cooling rate, grains form away from the surface become coarser in size compared to those formed in the layers near the surface [19]. Due to the important role of grain size in the mechanical properties of a part, we may expect the areas near the surface to exhibit higher strength and more ductile properties brought on by the finer grains that were observed. However, this is not the only criterion that should be considered as some other factors like the formation of defects and cracks affect the mechanical properties considerably. In the side view, the area near the substrate contained grains with a fine, equiaxed structure whereas the area away from the substrate contained columnar grain with cellular structure. In addition to the grain size and structure, the aspect ratio and orientation of the grains varied widely between the two regions as well. The area near the substrate was observed to have smaller grain but with a higher aspect ratio with greater elongation in the longitudinal direction. The two main factors that can affect the grain morphology include the solidification rate and thermal gradient of the layers [20]. Here, higher solidification rates can play a more impactful role than the temperature gradient in inducing an equiaxed grain structure. In other words, the higher cooling rates will most likely produce an equiaxed structure regardless of the temperature gradient present which is consistent with studies recommending surface cooling or supercooling of the layers to achieve an equiaxed morphology [21,22]. In this study, we have a drastic change in temperature between the build plate and the first layer of the part leading to a relatively high temperature gradient. With this information, one can infer that the equiaxed structure near the substrate is present largely because of the high temperature gradient between the hot first layer and relatively cool build platform. Conversely, it has been shown that grains in additively manufactured parts exhibit the spread of large columnar grains along the build direction over many layers in areas with lower solidification rates and high temperature gradients [21]. These findings are consistent with those shown in Figure 3.2b where columnar-dominant structures and grain elongation along the build direction were observed in the areas away from the substrate in which the cooling rate is significantly lower. It should be noted that equiaxed grains typically demonstrate more uniform mechanical properties whereas columnar grains are associated with anisotropic mechanical properties [18]. With this information, we can deduce that the areas away from the substrate will exhibit more anisotropic properties whereas the areas near the substrate will have more uniform properties.

The geometry of the melt pools greatly affects the local solidification rate and the shape of the subsequent grains formed in the fusion zone. As demonstrated in Figure 3.3, the areas away from the surface had smaller but more organized melt pools in comparison to those found near the surface. The size of the melt pool will be affected largely by the process parameters chosen which can have a drastic effect on the quality of the part such as the microstructure [23,24]. However, because the same process parameters have been applied throughout the entire part, these variations must be attributed to other factors. First, the melt pool size can be affected by the cooling rate. Due to the presence of conduction and convection, the areas near the surface, as mentioned before, have higher rates of cooling; thus, the penetrated area affected by the molten powder which constitutes the melt pool is restricted because of its shortened expansion time. This implies that the time allowed for the melt pool to penetrate to the previously manufactured layers is shortened and therefore will be less elongated in the vertical direction. This results in wider melt pools in the top view as the melt pools will mostly elongate horizontally, and shallower melt pools in the side view as is evidenced in Figures 3.3 and 3.4. Additionally, due to a mixture of convection and conduction at the top layers near the surface, the irregularly sized and shaped melt pools are logical. Second, due to the scanning nature of the laser used in LPBF, the energy input is suddenly stopped near the borders which in turn creates anisotropic heating of the boundaries whereas the area near the center is covered in a more uniform manner creating a homogeneous heating of the section. This can also produce larger and more uniform pools for areas away from the surface as opposed to those formed near the surface. For this reason, when observed from the side (as in Figures 3.4a and b), we see a deeper penetration of the melt pools into adjacent layers in the area away from the substrate as opposed to those near the substrate. It should be noted, that there is a strong correlation between the size of the melt pools and the local grain size and structure of the part as it affects the temperature gradient during the cooling and solidification phase. The shallower melt pools produce a downward flow of heat transfer during the solidification phase, opposite to the build direction, whereas the heat transfer for deeper melt pools depend on the local position and orientation of the melt pool boundary [18]. In the former, growth of columnar grains occur during the solidification of the melt pool as the bottom boundary moves upward, whereas the larger melt pools exhibited steady columnar grain growth whereby the movement of the orientation of the temperature gradient determines the direction of growth. Additionally, the size of the columnar grains can be directly affected by the depth of the melt pools which can be seen in Figure 3.4c where columnar grain growth is limited by the melt pool boundaries which in turn affect the overall grain size during solidification.

Precipitation during the build process could have a major impact on several factors of the final printed part including transformation temperatures and strain, critical stress for transformation, matrix composition, and the shape memory response of the alloy [25]. Figure 3.5 shows the formation of precipitates viewed from the top of the sample. As can be seen in the figure, only Ni-rich precipitates were found in the regions away from the surface whereas both Ni-rich and Ti-rich precipitates were observed in the regions near the surface. The microstructure of the material after solidification can contain an abundance of precipitates largely in part due to the rapid cooling in the highly localized melt pools leading to a non-equilibrium solidification during the additive manufacturing process [18]. Due to the effect of convection as well as conduction, the areas near the surface have more irregular features due to lack of equilibrium state compared to the areas away from the surface which leads to higher variations of precipitates near the surface. This scenario persists in the near the substrate. Due to the higher thermal gradient caused by the sudden change in temperature between the substrate and the first few layers, this region will take a relatively long time to reach a steady state condition. Thus, as is demonstrated in Figure 3.6, this region has non-uniform heat transfer and results in the formation of various precipitates. In comparison, the area away from the substrate contained no precipitates where the solidification rate is more uniform. Additionally, it has been found that epitaxial solidification can bring about enhancements in continuity and bonding as well as decreasing the intermetallic phases found between layers [26–28]. This most likely contributes to the lack of precipitates in the region away from the substrate in our findings where columnar grain growth was observed due to epitaxial solidification. It is of great importance to examine the individual contributions that each precipitate may have on the properties of the sample. In previous studies, it has been noted that the formation of Ni-rich precipitates produces a shift of the matrix composition to a higher titanium content (i.e., Ni depletion) that generally results in higher transformation temperatures [29]. In comparison, Ti-rich precipitates typically produce lower transformation temperatures. Additionally, Ni-rich precipitates have been linked to a reduction in fracture stress and strain due to the hindering of plasticity deformation [6].

Porosity and crack formation are among the most common structural defects found in AM fabricated NiTi [6]. Many factors may be attributed to the process of LPBF and additive manufacturing as a whole. As the process involves the melting of powder, a great assumption is made that the powder is evenly distributed and packed in an optimal manner for fabrication. Due to the fact that this is an idealization, one of the sources of pore generation comes from poor packing density of the metal powder which allows for entrapped gas to persist and create vacancies within the finished part [30]. Additionally, insufficient energy input during melting can results in sporadic areas where the powder has not completely melted leaving behind diamond-shaped pores. This lack of overlap between two or more adjacent metal powder particles is commonly referred to as a ‘lack of fusion (LOF) zone’ [31]. These factors cannot be excluded from the present discussion but are constant between all regions of the printed samples as the process parameters and the powder were the same throughout. It is possible that as defects begin to arise, the propensity for more defects to emerge may increase therefore as the sample is built, we may expect to see a higher amount of pores and cracks regardless of whether or not the process parameters and powder are the same. There are several contributing factors to the formation of cracks in fabricated NiTi parts [32,33]. One of these contributing factors is residual stress which is common to additive manufacturing due to the high temperature gradients inherent in the process. Crack initiation is visible in the areas near the surface, as is demonstrated by Figure 3.7, which can be again explained by the high temperature gradient where we expect to see higher quantities of residual stress. This leads to the inevitable formation of micro-cracks which in turn propagate and affect other areas as well. These cracks are typically limited to just micro-cracks as larger cracks are deterred from formation due to the rapid cooling which prevents their propagation [32,33]. However, there are instances where the temperature gradient results in high enough residual stresses that these effects overcome the effects of rapid cooling and wide cracks at the surface can form as is seen in Figure 3.7c where a crack of 100 μm in length can be observed. These longer cracks are hazardous as they can harbor un-melted powders due to the discontinuity in material. In observing the areas away from the surface, there were no obvious crack formations found as there is a lower temperature gradient in these areas with a more uniform condition. Nevertheless, some small, irregularly shaped defects can be found in a few cases. Misorientation is another factor in the formation of cracks and their propagation as has been shown before [34]. As depicted in Figure 3.1, the grains found at near the surface of the sample were found to be equiaxed and smaller in size resulting in a higher number of grain boundaries where misorientations can be more readily found. The grains in the regions away from the surface were found to be comparatively larger and therefore contained less grain boundaries which would lead to a lower probability of finding misorientations leading to cracks. This may be another explanation for the reduced number of cracks seen in the areas away from the surface compared to those near the surface. In most cases, there were two observable types of porosities within AM NiTi parts [35]. The first of these two porosities is a result of mixtures of the NiTi powder with trapped ambient gas which forms spherical-shaped porosities. However, there are different possible reasons for the defect found in Figures 3.8a and b which includes a region of separation, identified as an irregularly-shaped porosity, with a deposit of un-melted powder as a result of this porosity. This defect was most likely caused by unoptimized process parameters. Due to the low quantity of defects found similar to this example, the former is most likely the cause. It should be noted that there were considerably fewer defects found in the areas away from the surface where no visible cracks were found compared to the areas near the surface. From a side view, more defects were found near the substrate in comparison to the area away from the substrate. As mentioned previously, the high temperature gradient found between the substrate and the first layers of the sample causes sufficiently high residual stress to form large cracks. Figures 3.9a and b shows large, continuous cracks that were form at and near the substrate respectively, with their overall length exceeding 100 μm. Figure 3.9c shows that the widths of these cracks are large enough to allow for the isolated accumulation of non-melted powders and impurities. In comparison, the area away from the substrate contained less defects, and those that were found were smaller in size. A few tiny cracks were found in this area, shown in Figures 3.10a and b, and are most likely present due to the existence of the formation of precipitates and impurities. Although these cracks are small, the widths are still large enough to harbor un-melted powder. It has been found that attempting to force epitaxial growth through optimized process parameters may lead to a reduction in these defects [36]. As previously mentioned, columnar grain growth is common in areas away from the substrate where this type of grain growth is caused by epitaxial solidification in the layers leading to a reduction of defects in the area away from the substrate. This can be attributed to the fact that misorientation between columnar grains which formed parallel to the building direction is less than equiaxed like grains oriented randomly. With similar logic discussed before, the formation of more cracks near the substrate compared to regions away from the substrate seems reasonable.

Figures 3.11 and 3.12 showcase the results of the XRD analysis from the top and side view respectively. Firstly, the observations made in the precipitates section are consistent with those found in the XRD results which help confirm the existence of the particular precipitates found in both. Figure 3.11 shows the main phases of austenite and martensite of the top surface where one can see that the peak intensity for austenite is higher than that of martensite in both areas observed which is in agreement with previous studies [37–39]. However, the peak intensity of austenite near the surface is sharper than the intensity away from the surface. The variation in austenite phase intensity is a contributing factor in transformation temperature. Higher laser speeds resulting in higher cooling rates were found by Speirs et al. [37] to decrease the transformation temperatures. Due to these findings, coupled with the higher cooling rate near the surface, one can deduce that the transformation temperature is lower in this area which facilitates the formation of austenite phases. With the same logic, sharper peaks for the austenite phase are found for the area near the substrate as opposed to the area away. The formation of martensitic phase is also justifiable for all of the areas observed as Dadbakhsh et al. [40] have found that this phase can be formed after the fabrication of NiTi through LPBF without preheating.

The results obtained for microhardness ranged from 235 to 560 HV and from 220 to 560 HV for the top surface and side surface of the sample respectively which are consistent with the results generated by Shishkovsky et al. [39]. As can be seen in Figure 3.13a, values of hardness were found to be lower in the points collected near the surface and gradually rises until reaching a peak near the center of the sample. Previous studies have shown that optimizing the process parameters of a material can result in a crack and pore free structure, and as a result, drastically improving the microhardness [6]. In observing the region away from the surface, we found significantly less defects compared to the area near the surface which may help explain our results showing higher hardness values in the area away from the surface. A similar trend is evident in the side view where the hardness values were found to increase as one moves away from the substrate towards the middle, once again predicted by the higher number of defects found near the substrate.

Major deviations from the average for the area near the substrate are most likely explained by the enormous heat dissipation from the substrate to the build plate [39].

3.5. References

1. X. Wang, S. Kustov, J. Van Humbeeck, A short review on the microstructure, transformation behavior and functional properties of NiTi shape memory alloys fabricated by selective laser melting, Materials 11 (9) (2018) 1683.

2. J. Van Humbeeck, Damping capacity of thermoelastic martensite in shape memory alloys, J. Alloy. Comp. 355 (1–2) (2003) 58–64.

3. A. Bansiddhi, T. Sargeant, S.I. Stupp, D.C. Dunand, Porous NiTi for bone implants: a review, Acta Biomater. 4 (4) (2008) 773–782.

4. A. Dehghanghadikolaei, H. Ibrahim, A. Amerinatanzi, M. Hashemi, N.S. Moghaddam, M. Elahinia, Improving corrosion resistance of additively manufactured nickel–titanium biomedical devices by micro-arc oxidation process, J. Mater. Sci. 54 (9) (2019) 7333–7355.

5. K. Otsuka, X. Ren, Physical metallurgy of Ti–Ni-based shape memory alloys, Prog. Mater. Sci. 50 (5) (2005) 511–678.

6. M. Elahinia, N.S. Moghaddam, M.T. Andani, A. Amerinatanzi, B.A. Bimber, R. F. Hamilton, Fabrication of NiTi through additive manufacturing: a review, Prog. Mater. Sci. 83 (2016) 630–663.

7. N.S. Moghaddam, A. Jahadakbar, A. Amerinatanzi, M. Elahinia, Recent Advances in Laser-Based Additive Manufacturing, Laser-Based Additive Manufacturing of Metal Parts, CRC Press, 2017, pp. 1–24.

8. W.E. Frazier, Metal additive manufacturing: a review, J. Mater. Eng. Perform. 23 (6) (2014) 1917–1928.

9. T. Watanabe, S. Tsurekawa, The control of brittleness and development of desirable mechanical properties in polycrystalline systems by grain boundary engineering, Acta Mater. 47 (15–16) (1999) 4171–4185.

10. Y. Kok, X.P. Tan, P. Wang, M. Nai, N.H. Loh, E. Liu, S.B. Tor, Anisotropy and heterogeneity of microstructure and mechanical properties in metal additive manufacturing: a critical review, Mater. Des. 139 (2018) 565–586.

11. T. Bormann, B. Müller, M. Schinhammer, A. Kessler, P. Thalmann, M. de Wild, Microstructure of selective laser melted nickel–titanium, Mater. Char. 94 (2014) 189–202.

12. E. Liverani, S. Toschi, L. Ceschini, A. Fortunato, Effect of selective laser melting (SLM) process parameters on microstructure and mechanical properties of 316L austenitic stainless steel, J. Mater. Process. Technol. 249 (2017) 255–263.

13. C. Do Lee, Effects of microporosity on tensile properties of A356 aluminum alloy, Mater. Sci. Eng. A 464 (1–2) (2007) 249–254.

14. S. Shiva, I. Palani, S. Mishra, C. Paul, L. Kukreja, Investigations on the influence of composition in the development of Ni–Ti shape memory alloy using laser based additive manufacturing, Opt. Laser. Technol. 69 (2015) 44–51.

15. H. Karaca, S. Saghaian, G. Ded, H. Tobe, B. Basaran, H. Maier, R. Noebe, Y. Chumlyakov, Effects of nanoprecipitation on the shape memory and material properties of an Ni-rich NiTiHf high temperature shape memory alloy, Acta Mater. 61 (19) (2013) 7422–7431.

16. Y. Li, D. Gu, Parametric analysis of thermal behavior during selective laser melting additive manufacturing of aluminum alloy powder, Mater. Des. 63 (2014) 856–867.

17. N.S. Moghaddam, S.E. Saghaian, A. Amerinatanzi, H. Ibrahim, P. Li, G.P. Toker, H. E. Karaca, M. Elahinia, Anisotropic tensile and actuation properties of NiTi fabricated with selective laser melting, Mater. Sci. Eng. A 724 (2018) 220–230.

18. T. DebRoy, H. Wei, J. Zuback, T. Mukherjee, J. Elmer, J. Milewski, A.M. Beese, A. Wilson-Heid, A. De, W. Zhang, Additive manufacturing of metallic components–process, structure and properties, Prog. Mater. Sci. 92 (2018) 112–224.

19. Z. Wang, T.A. Palmer, A.M. Beese, Effect of processing parameters on microstructure and tensile properties of austenitic stainless steel 304L made by directed energy deposition additive manufacturing, Acta Mater. 110 (2016) 226–235.

20. W. Kurz, B. Giovanola, R. Trivedi, Theory of microstructural development during rapid solidification, Acta Metall. 34 (5) (1986) 823–830.

21. F. Yan, W. Xiong, E. Faierson, Grain structure control of additively manufactured metallic materials, Materials 10 (11) (2017) 1260.

22. Y. Zhang, L. Wu, X. Guo, S. Kane, Y. Deng, Y.-G. Jung, J.-H. Lee, J. Zhang, Additive manufacturing of metallic materials: a review, J. Mater. Eng. Perform. 27 (1) (2018) 1–13.

23. J. Beuth, J. Fox, J. Gockel, C. Montgomery, R. Yang, H. Qiao, E. Soylemez, P. Reeseewatt, A. Anvari, S. Narra, Process mapping for qualification across multiple direct metal additive manufacturing processes, in: Proceedings of SFF Symposium, Austin, TX, Aug, 2013, pp. 12–14.

24. J. Gockel, J. Beuth, K. Taminger, Integrated control of solidification microstructure and melt pool dimensions in electron beam wire feed additive manufacturing of Ti-6Al-4V, Addit. Manuf. 1 (2014) 119–126.

25. S. Saedi, A.S. Turabi, M.T. Andani, N.S. Moghaddam, M. Elahinia, H.E. Karaca, Texture, aging, and superelasticity of selective laser melting fabricated Ni-rich NiTi alloys, Mater. Sci. Eng. A 686 (2017) 1–10.

26. J.M. Walker, Additive Manufacturing towards the Realization of Porous and Stiffness-Tailored NiTi Implants, University of Toledo, 2014.

27. B.V. Krishna, S. Bose, A. Bandyopadhyay, Fabrication of porous NiTi shape memory alloy structures using laser engineered net shaping, J. Biomed. Mater. Res. Part B: Applied Biomaterials: An Official Journal of The Society for Biomaterials, The Japanese Society for Biomaterials, and The Australian Society for Biomaterials and the Korean Society for Biomaterials 89 (2) (2009) 481–490.

28. N.S. Moghaddam, S. Saedi, A. Amerinatanzi, A. Hinojos, A. Ramazani, J. Kundin, M.J. Mills, H. Karaca, M. Elahinia, Achieving superelasticity in additively manufactured NiTi in compression without post-process heat treatment, Sci. Rep. 9 (1) (2019) 41.

29. C. Haberland, M. Elahinia, J. Walker, H. Meier, J. Frenzel, Additive Manufacturing of Shape Memory Devices and Pseudoelastic Components, American Society of Mechanical Engineers Digital Collection, 2014.

30. B. Zhang, Y. Li, Q. Bai, Defect formation mechanisms in selective laser melting: a review, Chin. J. Mech. Eng. 30 (3) (2017) 515–527.

31. T. Vilaro, C. Colin, J.-D. Bartout, As-fabricated and heat-treated microstructures of the Ti-6Al-4V alloy processed by selective laser melting, Metall. Mater. Trans. A 42 (10) (2011) 3190–3199.

32. R.F. Hamilton, T.A. Palmer, B.A. Bimber, Spatial characterization of the thermalinduced phase transformation throughout as-deposited additive manufactured NiTi bulk builds, Scr. Mater. 101 (2015) 56–59.

33. Y. Yang, Y. Huang, W. Wu, One-step Shaping of NiTi Biomaterial by Selective Laser Melting, Lasers in Material Processing and Manufacturing III, International Society for Optics and Photonics, 2008, p. 68250C.

34. E. Chauvet, P. Kontis, E.A. J€agle, B. Gault, D. Raabe, C. Tassin, J.-J. Blandin, R. Dendievel, B. Vayre, S. Abed, Hot cracking mechanism affecting a non-weldable Ni-based superalloy produced by selective electron beam melting, Acta Mater. 142 (2018) 82–94.

35. B. Song, X. Zhao, S. Li, C. Han, Q. Wei, S. Wen, J. Liu, Y. Shi, Differences in microstructure and properties between selective laser melting and traditional manufacturing for fabrication of metal parts: a review, Front. Mech. Eng. 10 (2) (2015) 111–125.

36. R. Li, J. Liu, Y. Shi, L. Wang, W. Jiang, Balling behavior of stainless steel and nickel powder during selective laser melting process, Int. J. Adv. Manuf. Technol. 59 (9–12) (2012) 1025–1035.

37. M. Speirs, X. Wang, S. Van Baelen, A. Ahadi, S. Dadbakhsh, J.-P. Kruth, J. Van Humbeeck, On the transformation behavior of NiTi shape-memory alloy produced by SLM, Shape Memory and Superelast. 2 (4) (2016) 310–316.

38. A. Domashenkov, M. Doubenskaia, I. Smurov, M. Smirnov, A. Travianov, in: Selective Laser Melting of NiTi Powder, Lasers in Manufacturing Conference, 2017, p. 2017.

39. I. Shishkovsky, I. Yadroitsev, I. Smurov, Direct selective laser melting of nitinol powder, Phys. Procedia 39 (2012) 447–454.

40. S. Dadbakhsh, B. Vrancken, J.-P. Kruth, J. Luyten, J. Van Humbeeck, Texture and anisotropy in selective laser melting of NiTi alloy, Mater. Sci. Eng. A 650 (2016) 225–232.

41. C.A. Biffi, P. Bassani, M. Nematollahi, N. Shayesteh Moghaddam, A. Amerinatanzi, M.J. Mahtabi, M. Elahinia, A. Tuissi, Effect of ultrasonic nanocrystal surface modification on the microstructure and martensitic transformation of selective laser melted nitinol, Materials 12 (19) (2019) 3068.

42. M. Nematollahi, K.S. Baghbaderani, A. Amerinatanzi, H. Zamanian, M. Elahinia, Application of NiTi in assistive and rehabilitation devices: a review, Bioengineering 6 (2) (2019) 37.

4. THE EVOLUTION OF MICROSTRUCTURE AND COMPOSITION HOMOGENEITY INDUCED BY BORDERS IN LASER POWDER BED FUSED PARTS

4.1. Introduction and overview

Nickel-based superalloys are one of the most widely used materials over the past five decades as they play a significant role in industrial applications such as energy production, aerospace, and aeronautical applications [1–4]. Due to the high strength and remarkable corrosion resistance behaviors, they are utilized in turbine blades, engine components, combustors, and nuclear power plant parts [5,6]. Inconel718 (i.e., IN718) is one of the most researched nickel-based superalloys for industrial applications. Excellent mechanical properties coupled with high creep, corrosion, and fatigue resistance at high temperatures allow this alloy to be used in extreme temperature conditions up to 700 °C [4,7,8]. The desired mechanical properties have been achieved from conventionally fabricated IN718 in forms such as casting, forging, wrought and powder metallurgy [9,10]. However, these techniques are limited to simple geometries such as cylinder tubes, plates, and wires. Along with progress in manufacturing industry, the demand for fabrication of complex parts with high precision and excellent mechanical properties at elevated temperatures have been increased. Newer manufacturing techniques like Additive manufacturing (AM) offer a feasible solution and allow fabrication of near-net shape customized parts without the need for costly tools, molds, or casting dies [4,11,12]. From both scientific and industrial aspects, fabrication of IN718 parts using AM has drawn noticeable attention during the last decade [13–18]. Laser powder bed fusion (LPBF) is the most widely used AM technique that has been employed to manufacture highly complex parts with good accuracy [5,19–21]. This technique can produce fully dense IN718 parts (close to 99.7%) by selectively melting the metal powder spread on the build plate. In this case, laser acts as a heat source which traces the digital data of the part geometry [5]. Following that, the molten powders are combined to make a solidified layer. This process is repeated layer by layer until the part is fabricated [22–25]. However, there is still a need to improve the mechanical properties of the LPBF-fabricated IN718 components [9].

The unique multi-scale microstructure of LPBF-fabricated parts is one of the most important features which can be adjusted along with texture to achieve desired mechanical properties [9]. As a laser-based fabrication method, the LPBF technique has several processing parameters (laser power, scanning speed, hatch distance, and powder layer thickness), forming the Volumetric Energy Density (VED), which has a high influence on the microstructure, texture and thus the overall properties of the fabricated parts. As the microstructure and texture of LPBF-fabricated IN718 parts can be altered by changing the process parameters, several studies have been focused on how the microstructure/texture affects the performance of the as-built IN718 parts [4,9,10,14,18,26–28]. Moussaoui et al. [29] showed that an increase in VED during the LPBF fabrication of IN718 samples results in more elongated dendrite grain structures having a tendency to orient parallel to the build direction. They also concluded that the level of porosity can be reduced through an increase in the VED. Nadammal et al. [30] investigated the effect of hatch distance on the microstructure and texture of LPBF-manufactured IN718. It was revealed that hatch distance as a process parameter has a strong influence on the microstructure and texture. A ten-fold increase in hatch distance (decrease in VED) resulted in a reduction in texture intensity (100) by a factor of 2. In another study performed by Lu et al. [28], different island scanning strategies were selected for the fabrication of IN718 samples. It was concluded that components fabricated by larger island scanning strategies result in higher density whereas severe cracks were observed for the sample processed by smaller island sized scan strategy. The effect of scan speed on the microstructure and densification level of the IN718 samples were investigated in another study [31]. The authors concluded that a wide range of scanning speed (from 100 to 1600 mm/s) can be applied to fabricate parts successfully. However, the highest density level (99.7%) occurred when the laser scanning speed of 800 mm/s was employed. Popovich et al. [32] showed that with an increase in layer thickness (decrease in VED), the size of the cellular dendritic structures of LPBF-fabricated IN718 samples increases, and the likelihood of the formation of columnar grain structure increases.

Apart from controllable process parameters, a better understanding of the physics behind the LPBF process is the key for prediction and optimization of microstructure and texture of parts. As the LPBF technique is a high-temperature process, the heat transfer that occurs during fabrication can be one of the most important physical parameters to be considered. In a study conducted by Wang et al. [33] on the microstructure of LPBF-fabricated IN718, a phase filed model was used to simulate the process. It was revealed that the temperature gradient plays a significant role in the growth of dendrites and a higher temperature gradient lead to a higher growth speed of dendrites. However, the LPBF process is not only limited to the powder melting step, but also can be affected by the mode of solidification and cooling process. In the study performed by Zhang et al. [34], a physical model including heat transfer and fluid flow was used to simulate the thermofluidic field of melt pools for the LPBF process of IN718. It was shown that convective heat transfer has more influence over the shape of the melt pool compared to conduction heat transfer, with the contribution of convection in heat dissipation more than one order magnitude larger. They also found that convective heat flux affects the width of the melt pool, while conductive heat flux plays a role in regulating the dimensions of the depth and the width of the melt pool. In another study performed by Balbaa et al. [35], the effect of process parameters on the stability of the melt pools was investigated during the LPBF process of IN718 alloy. It was found that the cooling rate of the molten material dominantly affect the generation of residual stress, with higher cooling rate resulting in higher magnitude of stress. Gong et al. [36] studied the influence of build height on the microstructure and composition of LPBF processed IN718. They observed less formation of Laves phase but more uniform distribution of finer grains at the bottom layers, which was attributed to the higher cooling rate at this region.

In the study [37] discussed in the previous chapter, for the first time, insights on the spatial heat transfer conditions experienced by different areas of the under-processed part was provided during the LPBF process. It was revealed that the regions near the surfaces of the part are more affected by the convection heat transfer mode compared to the areas located at the middle. On the other hand, conduction was seen to play a more crucial role for the regions away from the surfaces. This variation in the heat transfer condition was found to be responsible for the different cooling rate experienced by different regions of the LPBF- fabricated part, and thereby resulting in microstructural inhomogeneity throughout the part. This study, for the first time, aims to implement a novel strategy in LPBF fabrication of IN718 parts to achieve a more unified microstructure and composition throughout the part. This approach is based on the design and fabrication of a border surrounding the main part during the LPBF fabrication. It is hypothesized that such border, if designed appropriately, would mitigate the undesirable convention heat transfer mode in the areas near the surface of the LPBF-fabricated parts and result in microstructure homogeneity. To this aim, a series of cubic samples surrounded by cubic borders are fabricated by considering different gaps between border and main sample.

4.2. Materials and methods

4.2.1. Powder Preparation and Fabrication

Gas atomized IN718 powder supplied by EOS North America (Pflugerville, TX, USA) was used in the fabrication of IN718 samples in this study. Fig. 4.1a shows the Scanning Electron Microscopy (SEM) micrograph of the fresh IN718 powder. Image J [38] software was used to determine the particle size of the fresh powder and a histogram of the particle-size distribution was obtained as seen in Fig. 4.1b. The average powder particle size was found to be 12 μm. Further analysis of the fresh IN718 powder revealed that the powder particles were mostly spherical in shape.

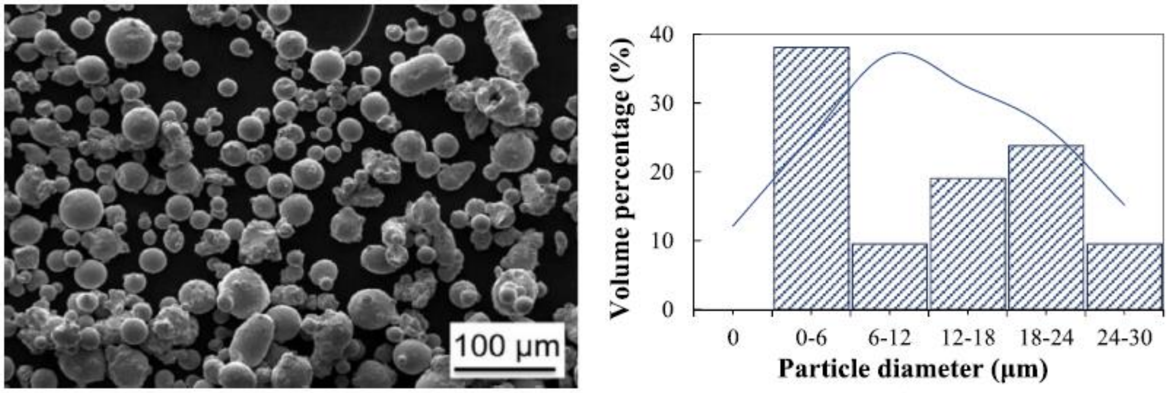

(a) (b)

Figure 4.1.Scanning electron microscope (SEM) micrograph of fresh powder; (b) particle size distribution of EOS supplied IN718 powder.

Cubic samples of dimensions 9 mm × 9 mm × 6 mm with the surrounding borders, as depicted in Fig. 4.2a, were designed in Solidworks (Dassault Systemes, Vélizy-Villacoublay, France). Since the focus of this work was to study the influence of the gap distance between the main sample and its associated border, different gap distances of 0.5 mm and 2 mm were considered. A cubic sample without border was also designed to serve as the reference sample in this study. An EOS M290 laser powder-bed fusion process printer (EOS GmbH, Electro Optical Systems, Krailling, Germany) having a build volume of 250 mm × 250 mm × 325 mm and fitted with a 400 W Ytterbium fiber laser was used to fabricate the parts. The samples were fabricated with a laser power of 285 W, a hatch distance of 110 μm, a scan speed of 960 mm/s, a layer thickness of 40 μm and the stripes scan strategy with a hatch angle of 67°, as recommended by the manufacturer. For the samples fabricated with border, the main part and the border were fabricated at the same time because the laser scanned both segments as a single part. The scan strategy is broken down by the software to first run the laser tracks on the infill of the cube and the border concurrently. Then the laser traces the contour of the border and cube simultaneously (Fig. 4.2b). The build plate was maintained at 80 °C during fabrication to reduce the overall thermal gradient, particularly within the first few layers. As it can be seen from Fig. 4.2c, a cubic sample without border is fabricated and this will serve as the reference sample in this study. Fig. 2d shows the sample fabricated with border at a gap distance of 2 mm. As the focus of this study is the main cubic sample and not the borders, the sample fabricated with a border at 0.5 mm distance will be addressed as gap 0.5 and the sample fabricated with a border at a distance of 2.0 mm will be addressed as gap 2.0 throughout the study. The parameters of the samples such as sample name, dimensions, geometry, and distance between the sample and its border is mentioned in Table 4.1.

Table 4.1.The geometry and dimensions of the fabricated samples

Sample No./Name	**Type of Geometry**	**Sample Dimensions (mm)**	**Border Dimensions (mm)**	**Gap Between Sample and Border (mm)**
Reference sample	Cubic	9×9×6 (w×l×h[1])	-	-
Gap 0.5 sample	Cubic	9×9×6 (w×l×h)	6×2 (H×t[2])	0.5
Gap 2.0 sample	Cubic	9×9×6 (w×l×h)	6×2 (H×t)	2.0

1: w, l and h are width, length, and height of the main sample, respectively.
2: H and t are height and thickness of the border, respectively.

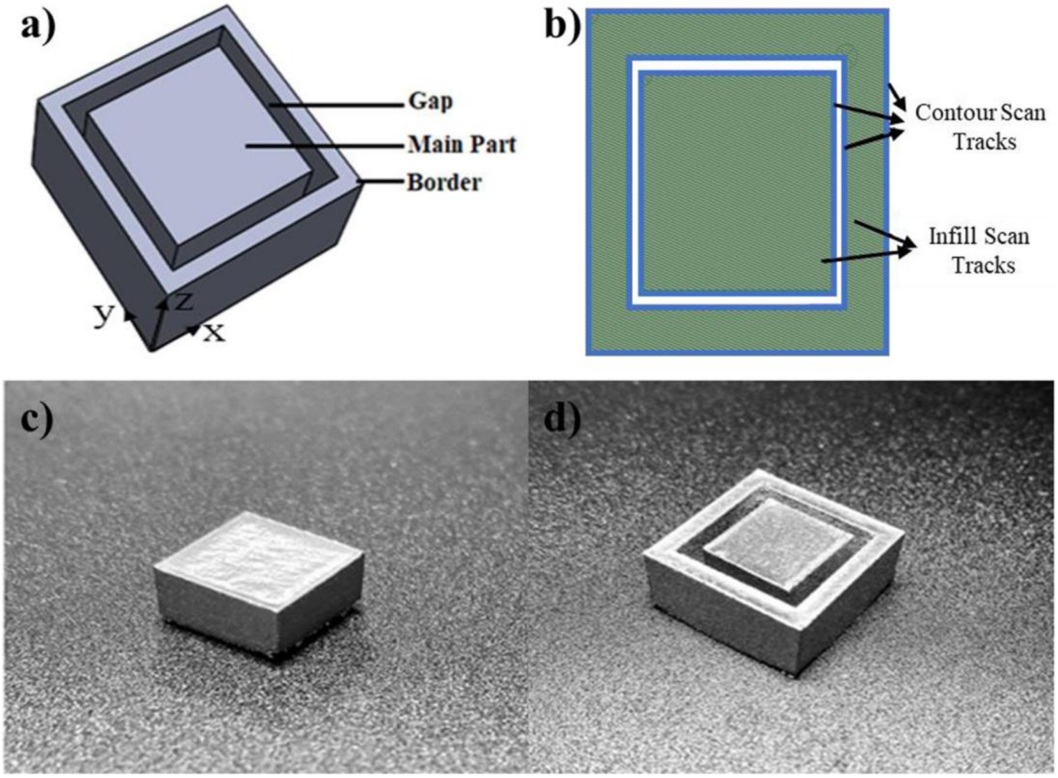

Figure 4.2.a) schematic of sample with border, b) infill and contour scan tracks for the main sample and border c) sample fabricated without border (reference sample) d) sample fabricated with border with 2 mm gap between the main sample and the border.

4.2.2. Experimental Procedure

In this study, a Nikon labophot-2 optical microscope (Nikon Instruments Inc., Melville, New York, U.S.A.) equipped with digital camera and a Hitachi S-3000N variable pressure electron microscope (Hitachi, Santa Clara, California, U.S.A.) were used to generate optical images and SEM results, respectively. To prepare the samples for microstructure analysis, they were first mounted on epoxy resin and then grinded and polished by E-prep 4TM (Allied High Tech Products Inc., Rancho Dominguez, California, U.S.A.) with power head through individual force mode. A series of silicon carbide (SiC) abrasive discs (320 to 1200 Grit size) were used to grind the specimens where water is used as the coolant liquid. The scratch pattern was inspected after each grinding step using a metallographic microscope XJP-H100 (Amscope, Irvine, CA). In each step, the grinding was repeated until a uniform pattern obtained for the scratches. Polishing process was performed through two steps. DiaMat polishing cloth with 1 µm diamond suspension was used to polish the samples at the initial step. Final polished surface was obtained using 0.04 µm colloidal silica suspension on a Red Final C polishing cloth. The samples were cleaned using Micro Organic Soap, rinsed with isopropyl alcohol and dried by compress air before etching. Prior to microstructural analysis, the samples were etched by Kalling's 2 Reagent (cupric chloride, hydrochloric acid, and ethanol).

Bruker D8 Advance X-ray diffractometer (Bruker AXS LLC, Madison, Wisconsin, U.S.A.) was used to determine the crystal and compositional structures of the samples. The Cu k-alpha X-ray source with wavelength of 1.5418 Å was used in the X-Ray Diffraction analysis. Step intervals of 0.04° and scan speed of 1sec/step were applied with 2ϴ varying between 30° and 100°. For the Vickers hardness measurement, a LECO LM 300 AT Micro Hardness Tester (LECO, St. Joseph, Michigan, U.S.A.) was used and 1Kg force was applied for 10 seconds.

4.3. Results

4.3.1. Microstructure analysis

4.3.1.1. Melt Pools

The melt pools of the gap 0.5, gap 2.0 and the reference samples were characterized with the help of an optical microscope at the center of the polished surface of the samples as seen in Fig. 4.3. The width and depth of the melt pools were measured using the ImageJ software and a significant difference in the dimensions were observed among the samples. The average width and depth of the melt pools are reported in Table 4.2. The deepest and widest melt pools were noted for the gap 0.5 sample as the border is fabricated relatively close to the main cubic sample which helps in the merger of smaller melt pools and thus expanding them to form deeper and wider melt pools. The optical micrograph of the gap 2.0 sample revealed the presence of narrow and deep melt pools. Observing the micrographs for the reference sample, narrow, shallow, and irregular melt pools can be seen. Comparing the samples fabricated with and without borders, it is clear that the samples fabricated with borders have uniform melt pools. Further analyzing the gap 0.5

and gap 2.0 samples revealed that as the gap between the main sample and the border decreases, the depth and the width of the melt pool increases significantly.

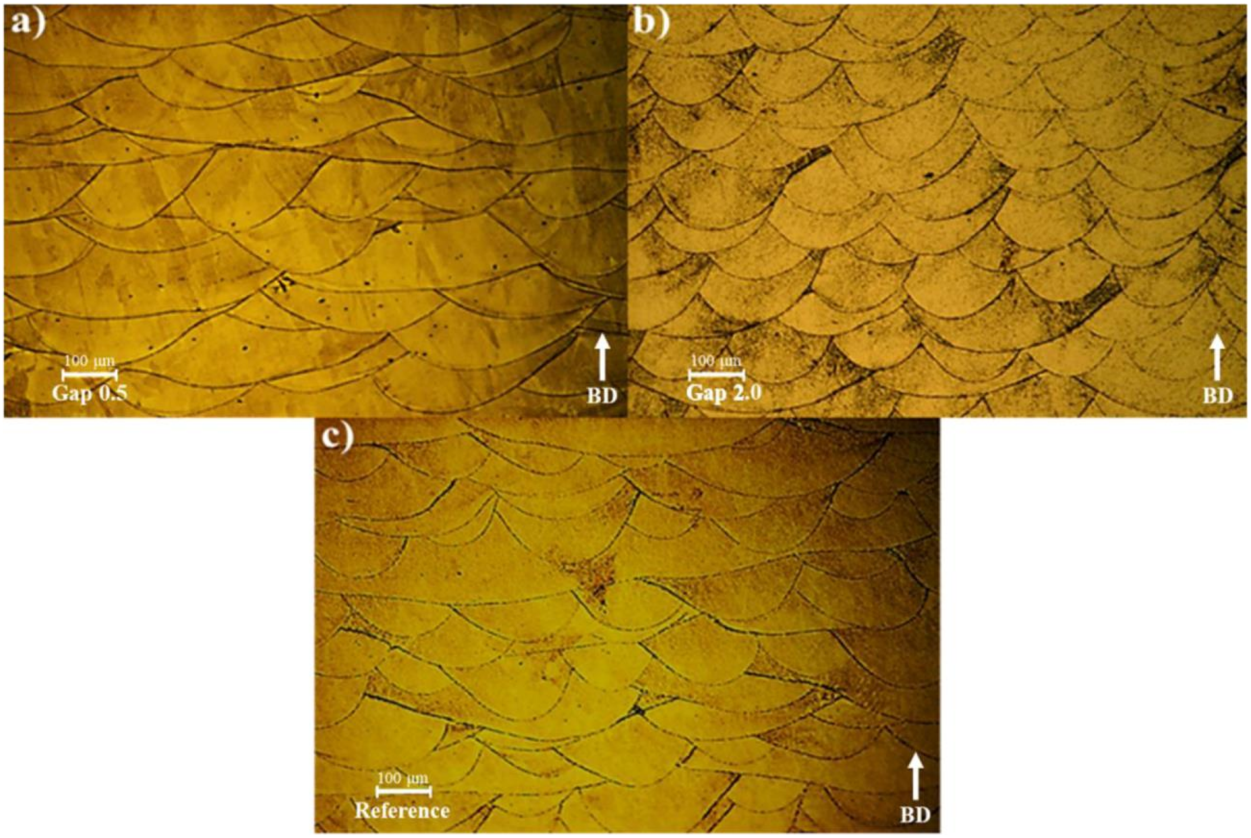

Figure 4.3.Optical microscopy of melt Pools for a) gap 0.5 sample b) gap 2.0 sample and c) reference sample.

Table 4.2.Melt pools dimensions extracted by Image J *software for three samples*

	Gap 0.5	Gap 2.0	Reference Sample
Average Melt Pool Width (µm)	378.5 ± 14.1	254.5 ± 8.2	274.1 ± 12.6
Average Melt Pool Depth (µm)	109 ± 4.5	102.6 ± 3.7	94.1 ± 4.2

SEM micrographs of the melt pools of the as-built IN718 samples are presented in Fig. 4.4 This figure helps us in observing the difference in structure of the melt pool boundaries. Analysis of Fig. 4.4a for the gap 0.5 sample exhibits a strong cohesive behavior between the melt pool boundaries. While the melt pool boundaries of gap 2.0 sample seen in Fig. 4.4b are found to have discontinuities along their boundaries. Fig. 4.4c reveals the melt pool boundaries for the reference sample and it can be seen that the melt pools boundaries are highly irregular. Thus, comparing the effect of the gap between the samples and its borders, it is evident that as the gap reduces, the melt pool boundaries become more cohesive and continuous in nature.

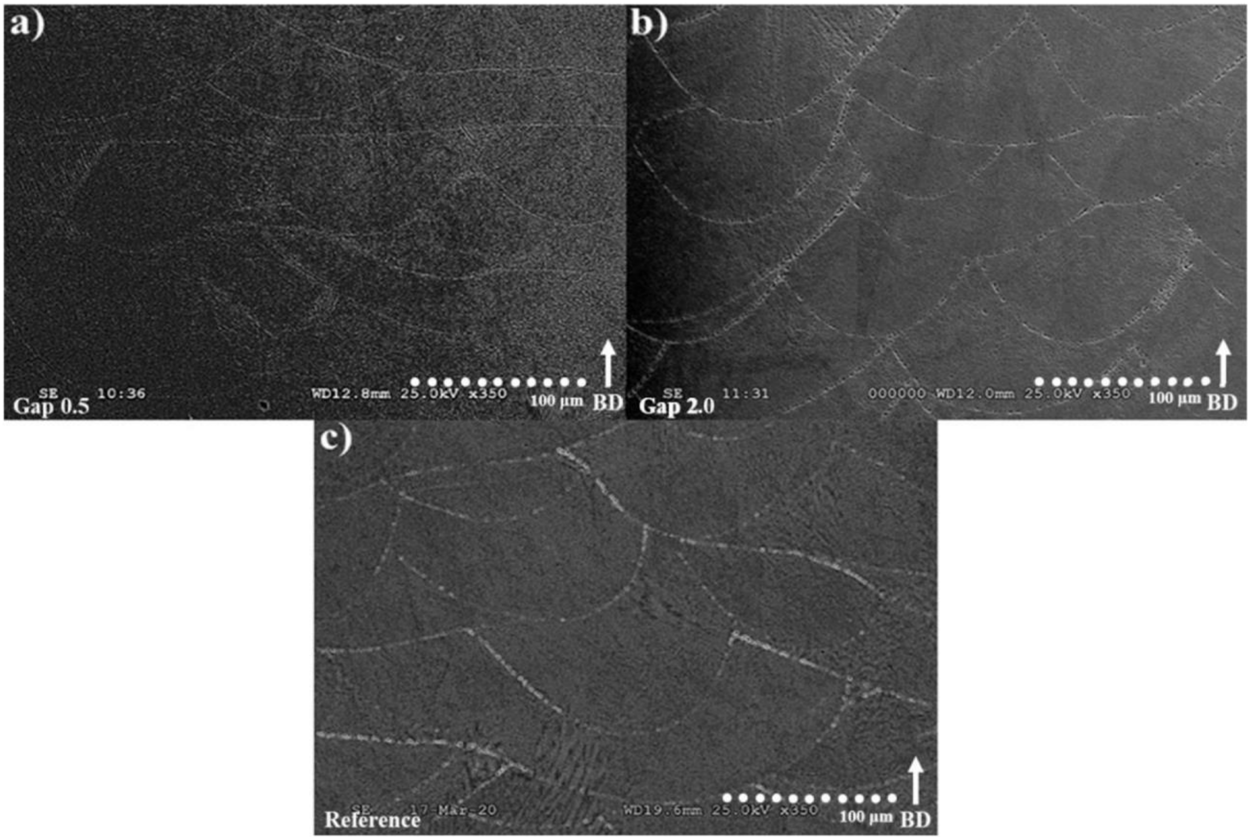

Figure 4.4.Scanning electron microscopy of melt Pools for a) gap 0.5 sample 1 b) gap 2.0 sample and c) reference sapmle.

4.3.1.2. Grain size and grain structure

Fig. 4.5a, b and c show columnar grains for gap 0.5, gap 2.0 and reference samples at the center of the polished surface of the as- built IN718 parts. Straight elongated grains can be found for both the samples fabricated with border. We can observe coherent grain boundaries with the grains oriented parallel to the build direction for the gap 0.5 sample while the gap 2.0 sample has tilted columnar grains with discontinuous boundaries. The aspect ratio of gap 0.5 sample was found to be greater than 1 as they are longer in the building direction. From Fig. 4.5c, we notice an increase in the irregularity of the boundaries for the reference sample as their grains are randomly oriented. The grains in the reference sample are shorter and tend to have an equiaxed structure.

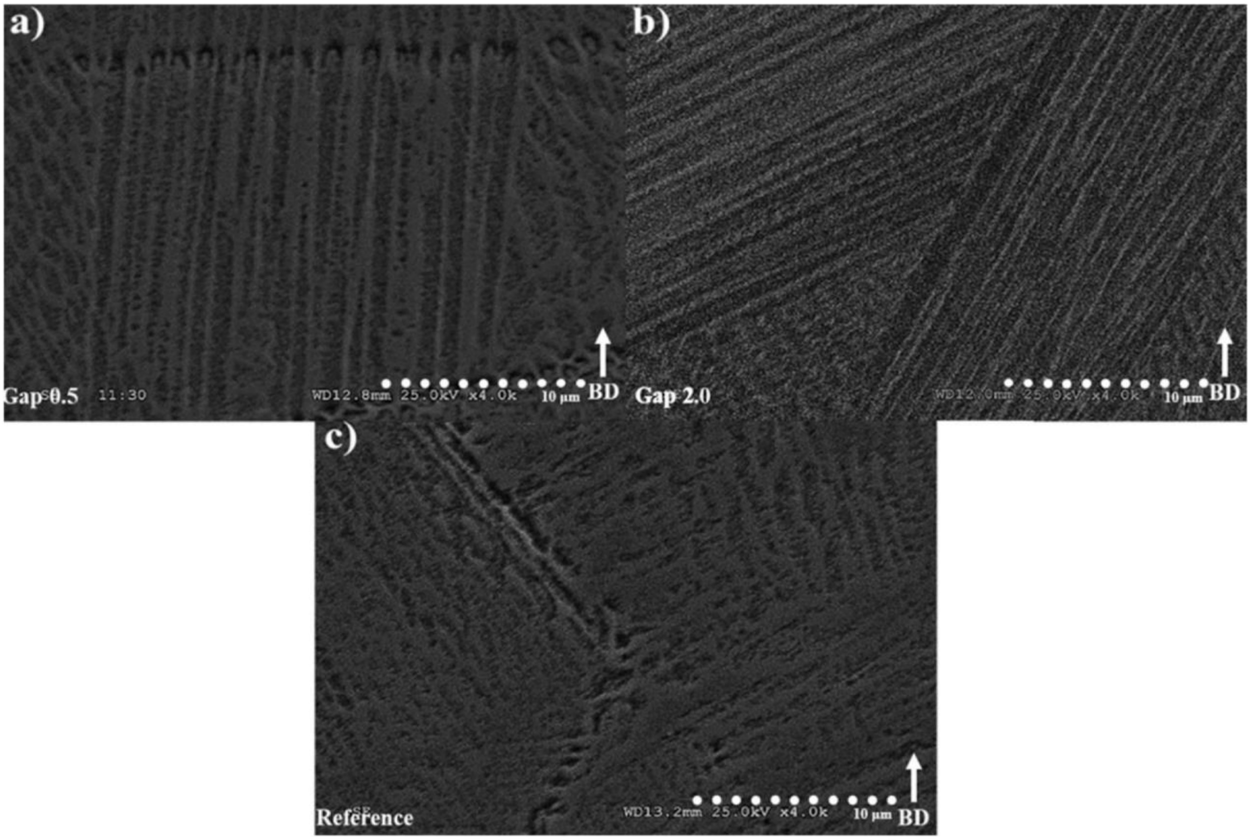

Figure 4.5.Scanning electron microscopy of columnar grains for a) gap 0.5 sample b) gap 2.0 sample and c) reference sample

The grain boundaries of the LPBF-fabricated IN718 samples were determined at the center of the polished surface of the samples with the help of SEM micrographs as shown in Fig. 4.6. The grain boundaries can be spotted due to remarkable change in texture and positioning of the dendrites. Gap 0.5 sample has grains oriented along the build direction as presented in Fig. 4.6a. Whereas, for the gap 2.0 sample, the grains are randomly orientated as observed in Fig. 4.6b. The reference sample consists of arbitrarily oriented grains as seen in Fig. 4.6c. It is worth noting that the reference sample has the smallest grains as the heat is dissipated faster compared to that of the other two samples fabricated with borders. Thus, we observe comparatively elongated grains in gap 0.5 and gap 2.0 samples.

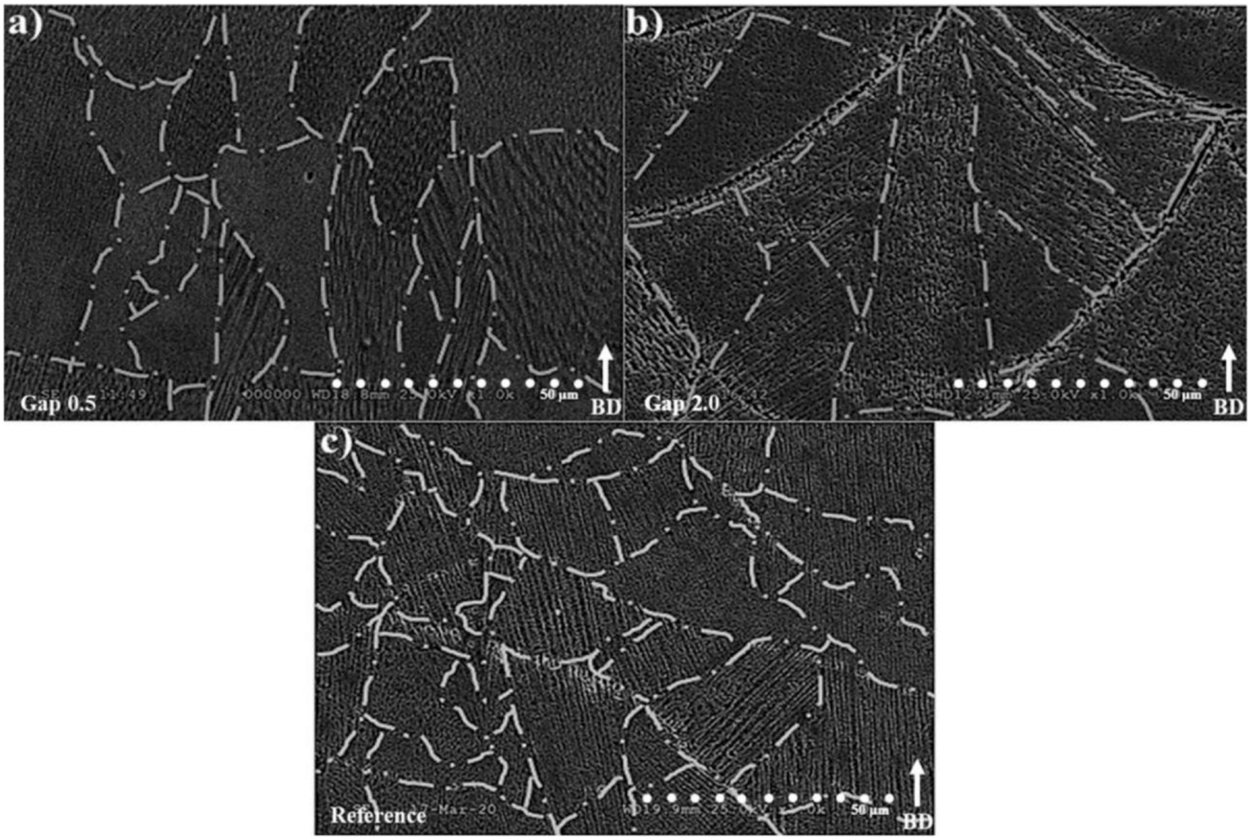

Figure 4.6.Scanning electron microscopy of grains for a) gap 0.5 sample b) gap 2.0 sample and c) reference sapmle.

4.3.1.3. Defects

The surface porosity of the fabricated samples at the center of the polished surface of the samples was determined with the help of SEM micrographs and their values were calculated using the ImageJ software. The porous areas in Fig. 4.7 are marked with white arrows. Firstly, the gap 0.5 sample had the least number of pores and had an average surface porosity of 0.072%. The observation of Fig. 4.7b reveals that sample gap 2.0 has the higher number of pores with an average surface porosity of 0.090%. The reference sample fabricated without borders revealed numerous tiny pores with highest average surface porosity of 0.103%.

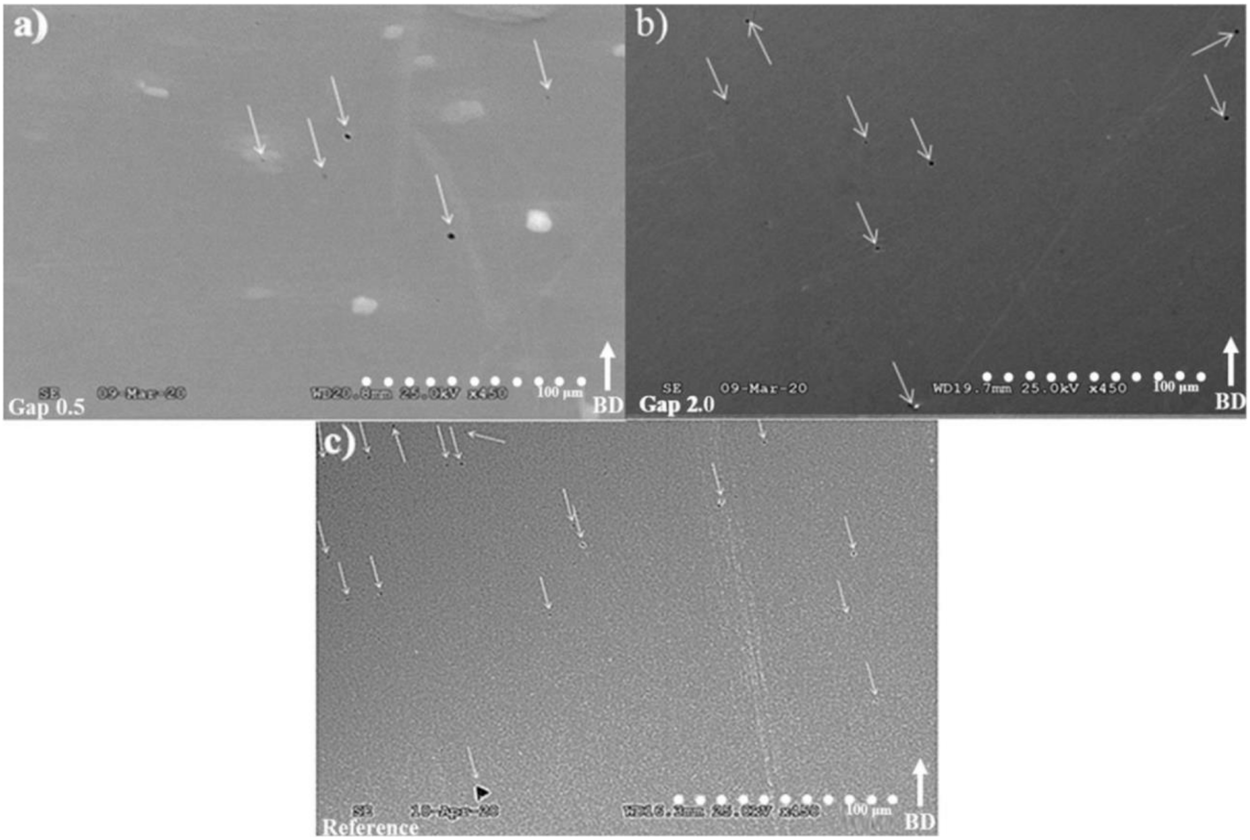

Figure 4.7.Porous areas formed for a) gap 0.5 sample b) gap 2.0 sample and c) reference sample

4.3.1.4. Precipitates

The SEM micrographs of the samples revealed the formation of precipitates corresponding to the possible phases of the IN718 alloy. As shown in Fig. 4.8, each phase is identified by a number for all the three samples. The presence of the Ni-Cr-Fe solid solution with Face Centered Cubic (FCC) Structure (γ phase), Ni_3Nb with Body-Centered Tetragonal (BCT) crystal structure (γ″ phase), MC-type carbide ((Nb,Ti)C) with FCC crystal structure and Ni3Nb with orthorhombic crystal structure (δ phase) is shown by numbers 1–4, respectively. The precipitates observed in this study are in agreement with the results reported in the literature. All the four phases (γ, γ″, MC-type carbide, and δ) detected for the samples have been reported by Seede et al. [40] for the IN718 LPBF-processed parts. In the similar study on IN718, the presence of MC-type carbide and δ phase was revealed using the microstructural analysis [29]. However, similar to the current study, the authors failed to detect the formation of γ′ phase under SEM as higher resolution is required. Also, Calandri et al. [4] used Energy Dispersive Spectroscopy (EDS) analysis to confirm the formation of carbides in the matrix phase. Similarly, EDS elemental maps confirmed the presence of MC-type carbide and δ phases in LPBF-fabricated IN718 alloy. However, as noticed in the current study, the formation of Laves phase was not found in the microstructure of the samples [5]. According to the results obtained in the current study, the level of formation of γ″ phase was found most for the gap 0.5 sample followed by the gap 2.0 sample, with a more uniform distribution for these samples compared to the reference sample. Conversely, carbide and δ phase were observed more for the reference sample as against the other samples.

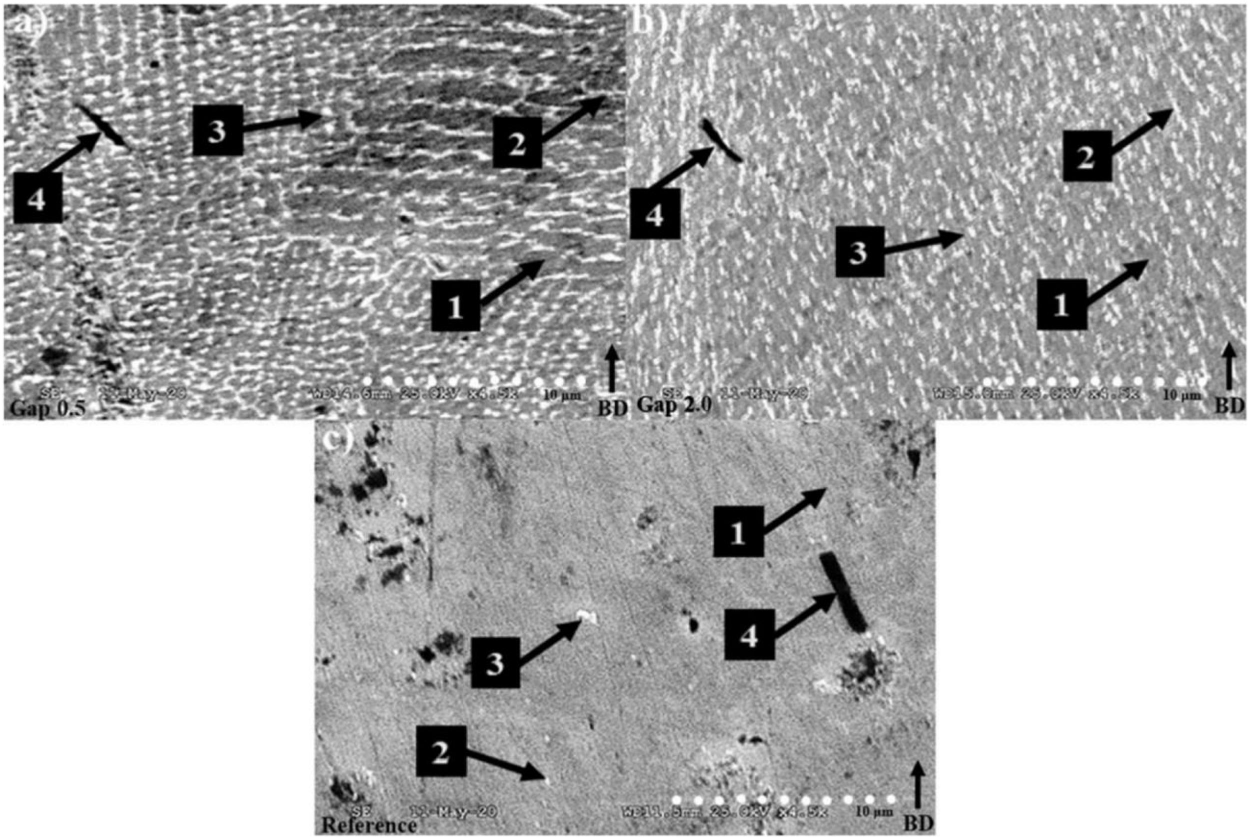

Figure 4.8.Precipitates formed in a) gap 0.5 sample b) gap 2.0 sample and c) reference sample (Numbers 1 to 4 correspond γ, γ″, MC carbide and Lave phases respectively)

4.3.2. X-Ray Diffraction (XRD) Analysis

Fig. 4.9 shows XRD diffractograms of the three samples with the formation of γ, γ′ and γ″ phases being extracted for all the three samples. The orientation of phases is depicted with miller indices next to each phase. The formation of phases is similar for all three samples, with no apparent peaks of δ and MC-type carbide phases being present. However, all these phases were observed in SEM micrographs. This is because the XRD analysis cannot detect the phases present at very low volume ratio of the specimen. Moreover, the corresponding peaks of the Laves phase are not clear in the XRD diffractograms. It is worth noting that the main peak for the gap 2.0 is different from those of gap 0.5 and reference sample, with γ, γ′, γ″ (200) and γ, γ′ (111)/γ″ (112) phases identified for the dominant peaks of gap 0.5, gap 2.0 and the reference sample, respectively.

Based on the intensity level shown in Fig. 4.9, the γ (200) peak which corresponds to the columnar grains formed parallel to the building direction, is highest for the gap 2.0 sample followed by gap 0.5 sample. However, a better texture analysis can be performed using the volume ratio based on the results obtained from the diffraction of phases. In this case, by ignoring the secondary phases, the area under the γ (111) and γ (200) peaks were calculated for each sample. The ratio of γ (200) to γ (111) was 1.26, 0.79 and 0.61 for gap 0.5 sample, gap 2.0 sample and reference sample, respectively. It should be noted that, this outcome is different but more accurate than the intensity comparison as it includes the volume ratio of the specimen.

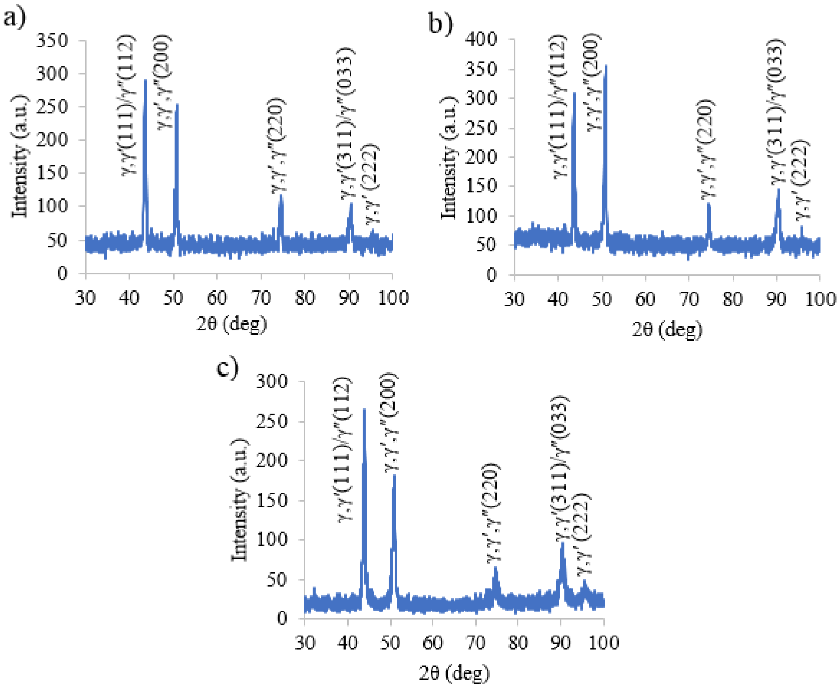

Figure 4.9.The XRD diffractograms of a) gap 0.5 sample b) gap 2.0 sample and c) reference sample

The effect of different heat transfer condition and solidification rate undergone by samples during the fabrication, can be observed through the shift of the γ peaks. In this case, all three samples were scanned with higher scan speed (sec/step) and finer increment for angles 2θ between 49° and 52° and the exact position of the second peak was extracted. The outcome is depicted in Fig. 4.10 where the shift of the (200) peak is visible for all three samples. For the samples fabricated with a border, the position of the peaks is shifted to the right compared to the peak of the reference sample. The highest change in peak position is visible for the gap 0.5 sample. The similar variation in peak position is reported for the heat-treated nickel-based alloys in previous studies [4,41]. This variation is caused by a change in the lattice constant of the γ phase. The lattice constant can be calculated using the Bragg's law (equation below) and the relation between the interplanar distance and the lattice parameter:

$$n\lambda = 2d \sin\theta$$

The λ, d and θ are the wavelength of the X-ray used in the XRD analysis, the interplanar distance and the angle of diffraction, respectively.

The value of the γ lattice constant is plotted in the Fig. 4.11 for the three samples. For each sample, the lattice constant was calculated using the average of the interplanar distance values extracted from the five peaks. The highest lattice parameter belongs to the reference sample, which is slightly more than gap 2.0 sample, with the least value being calculated for the sample with gap 0.5. This variation in the lattice parameter value confirms the peaks' mismatch observed in Fig. 4.10 where a larger shift in peak positions occurred between gap 0.5 and the reference sample.

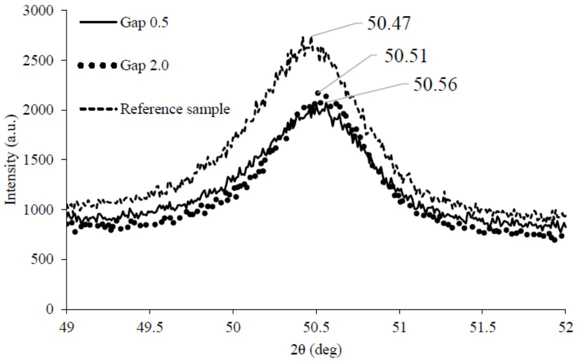

Figure 4.10.The variation in (002) peak position in the XRD diffractograms extracted for three samples

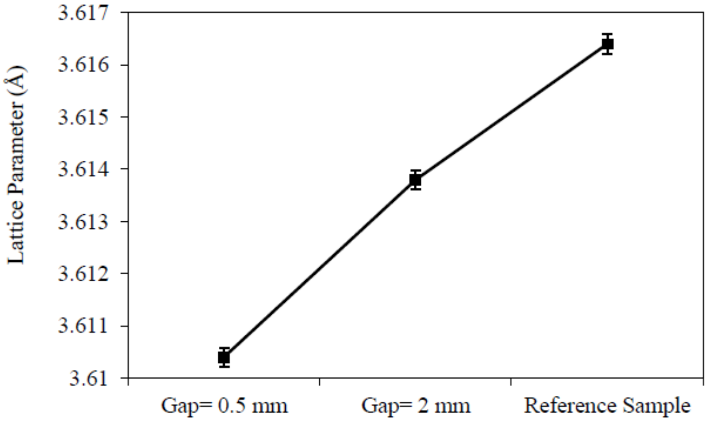

Figure 4.11.Lattice constant of the γ phase extracted from the XRD diffractograms of the samples.

4.3.3. Vickers Hardness

Fig. 4.12 represents the Vickers hardness values of the fabricated samples along the build direction (Side surface). The samples fabricated with border resulted in significantly higher Vickers hardness values of 336 HV and 330 HV for the gap 0.5 and gap 2.0 samples, respectively. However, the reference sample fabricated without border yielded an average Vickers hardness value of 306 HV. Thus, it can be observed that as the distance between the border and the main sample decreases, the Vickers hardness values increase.

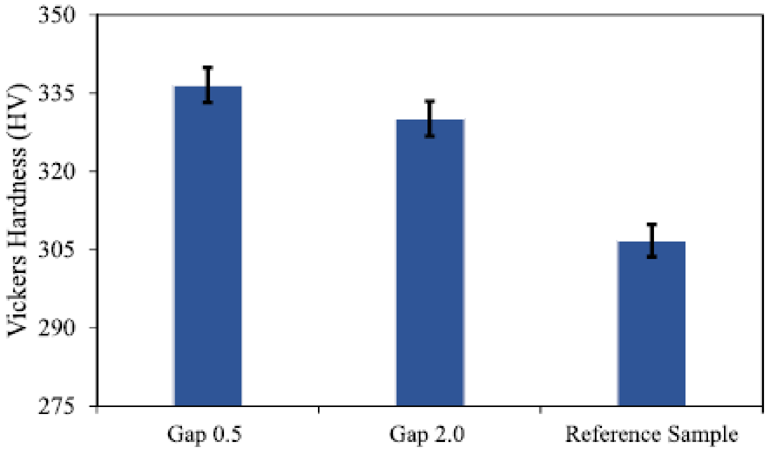

Figure 4.12.The average value of the Vickers Hardness for three samples

4.4. Discussion

This study investigates the effect of controlling the convective heat transfer near the surface areas on the microstructure and composition of LPBF-fabricated IN718 parts. It is hypothesized that a higher level of homogeneity in microstructure and composition can be achieved among different regions of the LPBF-processed part using a border surrounding the main part. To test this hypothesis, samples surrounded by borders with different gap values were fabricated and their microstructure and properties were compared with a sample which was built with the same process parameters but without a border. For all samples, results were generated from the plane parallel to the build direction and far from the border (side view).

The size and shape of the melt pools were characterized using optical and SEM micrographs for all three samples, as can be seen in Figs. 4.3 and 4.4. The average dimensions of the width and depth of the melt pools were generated for each sample with the help of the *Image J* software from the optical micrographs. Based on the average values shown in Table 4.2, deeper melt pools were observed for the gap 0.5 sample, whereas shallower pools belonged to gap 2.0 and reference samples, respectively. This can be attributed to the different heat transfer conditions and cooling rate experienced by samples during the fabrication process. For gap 0.5 and gap 2.0 samples which are surrounded by a border, heat transfer is restricted in the lateral direction (perpendicular to the build direction) while reference sample can undergo heat dissipation in both lateral and vertical (parallel to the build direction) directions freely. Therefore, for samples surrounded by border, heat transfer occurs more along the build direction compared to reference sample. This leads to a steeper thermal gradient in the build direction which allows the melted powder to penetrate deeper. Consequently, overlapping of the melt pools can occur and formation of new melt pools with bigger dimensions is possible (Fig. 4.13). Fewer melt pools per unit area exists due to the merging of smaller melt pools. This outcome is consistent with previous studies by Mostafa et al. [4] and Jia and Gu [13], where they reported the formation of deeper and wider pools due to a steep thermal gradient and laser overlapping [5,14].

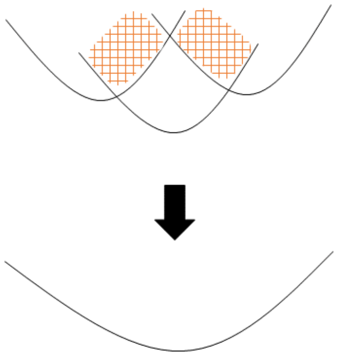

Figure 4.13.Overlapping of melt pools results in formation of bigger pools (overlapped regions are highlighted)

Regarding the effect of the gap between the main sample and the border on the melt pools' dimensions, the same logic can be followed. As the gap between the main sample and border is reduced, the heat generated by laser is confined for longer time and heat dissipation rate is reduced. The smaller the gap, the longer the solidification time in the horizontal direction and the more time molten metal can penetrate vertically. In other words, when the gap is smaller, the ratio of heat transfers in the vertical direction (build direction) to the lateral direction is higher compared to larger gap values. Therefore, for the sample fabricated with smaller gap (gap 0.5 sample), bigger melt pools are formed as conditions are better for the melt pools to merge. It should be noted that the thermal gradient can affect the level of homogeneity of the melt pools. Higher thermal gradient in the build direction compared to the other directions brings about more regular melt pools. As a result, more regular melt pools can be observed for gap 0.5 sample which experienced the steepest thermal gradient in build direction. It has been shown that the melt pool geometry plays a significant role in grain size and grain structure. In this case, the flow of heat transfer opposite to the build direction occurs for the shallower melt pools during the solidification process, while for deeper melt pools the heat transfer is controlled by the local orientation of the melt pool boundary [11]. Moreover, melt pool boundaries can affect the microscopic slipping under loading conditions, fracture mode, level of anisotropy, and ductility of LPBF-processed parts [42]. Therefore, different dimensions and orientations of melt pools formed in the samples fabricated in this study, can lead to different mechanical properties. A case in point is fracture of LPBF-fabricated parts under tensile loading which originates from cracks formed at the melt pool boundaries [42]. One can infer that with larger melt pools formed in the samples fabricated with border, the probability of failure under tensile loading would be decreased. It should be noted that in terms of width, gap 0.5 sample has also widest pools which can be attributed to the overlapping of pools. However, wider pools were found for the reference sample in comparison with gap 2.0 sample. It can be inferred that overlapping didn’t occur completely for the gap 2.0 sample, but still elongation in vertical direction because of the higher thermal gradient resulted in deeper but narrower pools with respect to the reference sample.

Regardless of the dimensions, the structure of the melt pool boundaries (MPB) is visible in SEM micrographs. As can be seen in Fig. 4.4, melt pools are separated with stronger boundaries for gap 0.5 sample compared to the other two samples, with discontinuity being formed along the boundaries particularly for reference sample. The difference observed between the structure of the MPBs is rooted in the fabrication process of LPBF. Generally, the way that a part is fabricated through LPBF method is a cumulative process of laser scanning tracks and melting the powders which forms melt pools. Thus, some of the melt pools formed in the previous layers remelt and solidify repetitively due to the heat penetration into the bottom layers. These areas are called Heat Affected Zones (HAZ) which was also reported in previous studies [43–45]. Near the HAZ, the boundary of melt pools can be broken and extended as some areas may experience overlapping of melt pools. Consequently, new boundaries are formed with different structures compared to the initially formed boundaries. As discussed before, the formation of new melt pools originated from overlapped initial melt pools and this tends to happen more for gap 0.5 sample. Thus, we expect to see a different structure for MBS’ between samples, with stronger and weaker bonds corresponding to higher and lower possibility of overlapping being formed as MPBs for gap 0.5 and reference samples, respectively. As mentioned earlier, the tensile strength of LPBF-processed samples are dependent on the bonding quality of the pools, and it can affect the mechanical properties. Considering only this feature, higher tensile strength is expected for the gap 0.5 sample.

The microstructure of the samples fabricated in this study are columnar grains that line up relatively parallel to the build direction as shown in Fig. 4.5. This outcome is consistent with results mentioned by previous studies [14,29,42,46,47]. Due to the complexity of the LPBF process and phase transformations occurring during solidification, besides the process parameters, build geometry/layout combined with heat transfer condition are several factors that can affect the grain size, structure, and orientation [48]. Formation of columnar grains can also be attributed to the high thermal gradient towards the baseplate as the heat dissipation through conduction is the dominant mode of heat transfer during LPBF. The alignment of columnar grains is more parallel to the build direction for gap 0.5 sample, while there is an inclination for the two other samples. As mentioned previously, high thermal gradient parallel to the build direction is the main cause for formation and elongation of columnar grains in this direction. As a result, we can expect to see a higher level of alignment parallel to the build direction for high thermal gradient. Based on the condition of fabrication, gap 0.5 sample experiences higher thermal gradient towards the baseplate since the lateral heat transfer is more limited in this case due to the less gap value between the sample and border. Therefore, less inclination in grain orientation can be seen for gap 0.5 sample. This is also consistent with the previous observations where it is reported that columnar grains may orient with the angle of 35–40° to the building direction in lower power or low thermal gradient conditions [47]. However, this is not the only difference that can be found from Fig. 4.5. Stronger bonds are formed between grain boundaries for gap 0.5 sample whereas discontinuities can be observed in columnar dendrites for the other samples. With the confinement of heat in gap 0.5 sample, an increase in the amount of heat and power is transferred through build direction, high temperatures are maintained for longer periods within the melt pool. This can bring about more internal energy and thermodynamic potential leading to stronger epitaxial growth which results in the formation of stronger grain boundaries. This phenomenon is reported by Jia and Gu [14] where they found disconnected dendrite structure for lower energy density and strong bonding in columnar architectures for higher energy density. When it comes to the structure of the grains, a combination of cellular and band structure can be observed for the columnar grains formed in gap 0.5 sample while grains in two other samples have dendritic structure. It has been revealed that at certain growth rates, increase in temperature gradient results in structural transformation from dendritic to cellular. Therefore, it makes sense if we see more of a cellular structure in some regions for gap 0.5 sample which undergoes the highest thermal gradient. However, formation of band structure is a little more complex. Formation of band structures requires several steps including conversion of regular cell structure into elongated cell structure and finally formation of columnar cells into bands. Zhou et al. [49] investigated this phenomenon for 316 L steel fabricated by LPBF and were in the opinion of inability of current theoretical statements in justifying this transformation. They claimed that this phenomenon has nonlinear self-organization behavior, and it can be attributed to a high Marangoni convection that happens at the front of the solid-liquid interface. They proved that for a high temperature gradient, the molten fluid can flow at the melt pool edge area and band-like structure can be formed from the pool's edge toward the center. They observed this structure at the horizontal plane while the same thing can occur in the vertical direction. However, as they mentioned, since the temperature gradient in melt pools are asymmetrical and can vary based on the conditions, cellular, columnar cells, and band-like structure can be formed simultaneously. This explains the formation of band-like structures in areas of gap 0.5 sample which has the highest thermal gradient with cellular grains surrounding the band structure. It should be noted that, to the knowledge of authors, this is the first time that this phenomenon is discussed for IN718 LPBF-fabricated samples.

Fig. 4.6 shows the representative grains for the three samples in a broader area, with the potential grain boundaries being specified by white dotted lines. The different growth orientation between dendrites or different structure in sub-grains was used to define boundaries. Due to the competitive growth between grains, some grains stopped growth after colliding with adjacent grains. Grains formed in gap 0.5 and gap 2.0 samples possess higher aspect ratio than reference sample. This is because of elongation of grains in the building direction and formation of more columnar structures in samples surrounded by border. This observation can be attributed to the fact that higher thermal gradient in building direction experienced by samples confined with borders provides conditions for growth of grains in the same direction. Moreover, the alignment of grains parallel to the building direction can be observed more in gap 0.5 sample which undergoes the highest thermal gradient. This is consistent with previous observations in which the high temperature gradient results in an epitaxial solidification phenomenon that is required for grain growth beyond the melt pools' boundaries [29]. In terms of structure, a combination of cellular and dendritic structure can be observed for gap 0.5 sample compared to the other samples where the dendritic structure is the dominant structure. This is consistent with the previous observations discussed here. When it comes to the grain size, finer grains formed in reference sample when compared to the samples surrounded by border. This result was expectable since we know as the solidification rate increases, the grain size decreases. For reference sample, the heat can dissipate faster as it is not confined laterally and therefore the epitaxial solidification cannot continue for a long time. Thus, finer grains are formed in this case. On the other hand, between samples surrounded by border, gap 0.5 sample (smaller gap) has finer grains. We know that the morphology and size of grains are affected by two main factors, solidification rate and temperature gradient [50]. Therefore, different combinations of cooling rate and temperature gradient result in various grain size. As mentioned before, less value of gap results in higher thermal gradient in the building direction. The smaller average grain size observed for the sample fabricated with less border's gap can be attributed to the higher thermal gradient experienced by this sample. However, more investigation is needed to explore the exact phenomenon for this case. It should be noted that grain size can directly affect the mechanical properties as the high correlation has been reported between strength and yield stress with the grain size (Hall–Petch relationship) [51]. A lower strength is expected for the samples fabricated with border, but due to the reduction in grain boundaries, an improvement in ductility can be achieved.

Fig. 4.7 shows the representative pictures for the three samples, with surface porosities were shown by white arrows. In this case, gap 0.5 and reference samples had the least and most value of surface porosity, respectively. It has been shown that formation of porous areas in LPBF process rooted in accumulation of molten metal due to the high value of dynamic viscosity [14]. As the flowability of the molten fluid increases, the probability of pore formation decreases. Based on the similar logic discussed throughout this section, higher thermal gradient in the building direction provides more flowability for the molten liquid and it can flow smoothly. On the other hand, the possibility of cooling in all directions exists for reference sample can lead to the non-homogeneity in thermal gradient and preventing a smooth flow for the molten liquid. Hence, looking at the side parallel to the building direction, the level of densification for reference sample is less than two other samples. The low level of porosity was observed for gap 0.5 and gap 2.0 samples compared to reference sample can be reported as a significant outcome resulted from the innovative condition of fabrication considered in this study. It has been revealed that one of the major disadvantages of the LPBF technique is manufacturing parts with a high level of porosity [18]. However, in this study, it was shown that the level of densification can be improved by limiting the convection heat transfer.

Fig. 4.8 represents the formation of different precipitates in all three samples. Based on the results, the main γ phase and three secondary phases of γ″, MC carbide and δ phases were identified for all the samples. However, the level of precipitation and distribution of the phases were different among the samples. The γ″ phase (Ni3Nb with BCT crystal structure), which is one of the secondary phases accounts for the main strengthening phase [52], was observed to form in higher level with more uniform distribution in the samples fabricated with border. This implies higher strength and hardness properties for these samples. On the other hand, higher level of formation of carbide and δ phase was seen for the reference sample. It has been revealed that formation of these phases is detrimental for mechanical and corrosion properties [53]. The less formation of these phases in the samples fabricated with borders can be attributed to the heat accumulation during the fabrication process. It has been reported that exposing IN718 samples to high temperatures for longer time delays the formation of δ phase into the matrix. It also leads to the Nb separation removal, which is the main element for the formation of carbides [54]. This thermal condition was experienced more by the samples fabricated with border and thus less precipitation of δ and carbides can be expected. The γ (111) and γ (200) phases were identified as the dominant phases of all three samples based on the XRD data shown in Fig. 4.9. This outcome is widely reported in the literature [5,6,40,55]. The overlapping of (002) and (022) γ″ peaks with γ phase at the same orientation is evidence of formation of the precipitates in a columnar microstructure parallel to the principal γ phase. This phenomenon has been mentioned in the previous studies [5,6]. However, the formation of columnar microstructure parallel to the building direction can be investigated through comparison of γ (200) and γ (111) phases, with higher γ (200) volume percentage showing a stronger columnar structure in the vertical plane (parallel to the build direction). Based on the ratio of γ (200) to γ (111) phase calculated for each sample, gap 0.5 sample has the strongest columnar structure with the volume portion of γ (200) phase exceeding that of γ (111). In contrast, the weakest columnar structure belongs to reference sample with the ratio of around 60 percentages. This is consistent with the observations discussed in this study where more columnar grains formed in gap 0.5 sample due to the higher thermal gradient in vertical direction. We know that formation of columnar grains leads to the anisotropic behaviors in sample, but higher strength in the direction of grain growth.

The dissolution of secondary phases into the γ phase results in increasing the lattice constant of the matrix. As shown in Fig. 4.11, the maximum lattice constant is obtained for the reference sample. It has the highest amount of dissolved secondary phases, but a smaller number of precipitates. Conversely, a reduction in lattice parameter can be seen for the samples fabricated with border which implies more level of precipitation. In other words, higher level of precipitation associates with decrease in the lattice constant leading to the decrease in the interplanar distance. Since the wavelength is constant in the Bragg's law equation, with decrease in the interplanar distance, the angle of diffraction should be increased. This outcome is visible in the Fig. 4.10 where the peaks correspond to the gap 0.5 and gap 2.0 samples shifted to the right side which shows increase in the diffraction angle and can be inferred as more precipitation level. This change in the proportion of phases can lead to change in strength and ductility of the samples.

A comparison between the samples fabricated with border and reference sample reveals a greater microhardness value for the former. It has been reported that the hardness of IN718 alloy is mainly attributed to the precipitation of BCT γ″ and FCC γ′ phases, with the effect of γ″ phase being dominant due to the larger misfit with γ phase [55]. This can be observed for the gap 0.5 sample with highest level of precipitation (due to the reduction in lattice parameter) and highest hardness value, followed by gap 2.0 sample. Also, it has been reported that with increase in overlap between the melt pools, more localized reheating occurs cyclically which resembles the heat treatment process. This, in turn, facilitates the dispersion of fine γ″ particles more evenly in these areas [6,18,56] and results in higher hardness values. A similar scenario takes place in the current study, where the overlapping of melt pools and higher local temperature was observed for the samples fabricated with border. Consequently, smaller but more even distributed γ″ phases form in the areas surrounded by the border which results in higher hardness values. It should be noted that as these secondary phases precipitate more evenly but in smaller size among the γ matrix, the XRD analysis may fail to detect all these fine particles. Moreover, formation of more columnar grains elongated parallel to the building direction can be considered as another factor affects the hardness value. Since there is a direct relationship between formation of columnar grains and microhardness value [40], greater hardness value is expected to be seen for gap 0.5 and gap 2.0 samples with more columnar grain structure.

4.5 References

1. J.J. Beaman, J.W. Barlow, D.L. Bourell, R.H. Crawford, H.L. Marcus, K.P. McAlea, Process methods, Solid Freeform Fabrication: A New Direction in Manufacturing, Springer, US, 1997, pp. 23–49.

2. C.K. Chua, K.F. Leong, C.S. Lim, Rapid prototyping process chain, Rapid Prototyp. (2010) 25–34.

3. M. Kiriti, T. Himanth Kumar, R. Bharath Bhushan, F. Behzad, M. Narges Shayesteh, A. Amirhesam, Study on the influence of post-processing parameters over microstructure and metallurgical properties of NiTi alloy, in: Proc.SPIE, 2020.

4. M. Calandri, S. Yin, B. Aldwell, F. Calignano, R. Lupoi, D. Ugues, Texture and microstructural features at different length scales in inconel 718 produced by selective laser melting, Materials 12 (2019) 1293.

5. A. Mostafa, I. Picazo Rubio, V. Brailovski, M. Jahazi, M. Medraj, Structure, texture and phases in 3D printed IN718 alloy subjected to homogenization and HIP treatments, Metals 7 (2017).

6. K.N. Amato, S.M. Gaytan, L.E. Murr, E. Martinez, P.W. Shindo, J. Hernandez, S. Collins, F. Medina, Microstructures and mechanical behavior of Inconel 718 fabricated by selective laser melting, Acta Mater. 60 (2012) 2229–2239.

7. A. Thomas, M. El-Wahabi, J. Cabrera, J. Prado, High temperature deformation of inconel 718, J. Mater. Process. Technol. 177 (2006) 469–472.

8. B. Pieraggi, J.-F. Uginet, Fatigue and creep properties in relation with alloy 718 microstructure, The Minerals, Metals & Materials Society, (1998).

9. S. Holland, X. Wang, J. Chen, W. Cai, F. Yan, L. Li, Multiscale characterization of microstructures and mechanical properties of Inconel 718 fabricated by selective laser melting, J. Alloy. Compd. 784 (2019) 182–194.

10. V.A. Popovich, E.V. Borisov, V. Heurtebise, T. Riemslag, A.A. Popovich, V.S. Sufiiarov, Creep and Thermomechanical Fatigue of Functionally Graded inconel 718 Produced by Additive Manufacturing, Springer International Publishing, Cham, 2018, pp. 85–97.

11. T. DebRoy, H.L. Wei, J.S. Zuback, T. Mukherjee, J.W. Elmer, J.O. Milewski, A.M. Beese, A. Wilson-Heid, A. De, W. Zhang, Additive manufacturing of metallic components – process, structure and properties, Prog. Mater. Sci. 92 (2018) 112–224.

12. L.E. Murr, E. Martinez, K.N. Amato, S.M. Gaytan, J. Hernandez, D.A. Ramirez, P.W. Shindo, F. Medina, R.B. Wicker, Fabrication of metal and alloy components by additive manufacturing: examples of 3D materials science, J. Mater. Res. Technol. 1 (2012) 42–54.

13. L.E. Murr, Metallurgy of additive manufacturing: examples from electron beam melting, Addit. Manuf. 5 (2015) 40–53.

14. Q. Jia, D. Gu, Selective laser melting additive manufacturing of Inconel 718 superalloy parts: densification, microstructure and properties, J. Alloy. Compd. 585 (2014) 713–721.

15. Y.-L. Kuo, S. Horikawa, K. Kakehi, The effect of interdendritic δ phase on the mechanical properties of Alloy 718 built up by additive manufacturing, Mater. Des. 116 (2017) 411–418.

16. X. Gong, K. Chou, Microstructures and mechanical behavior of Inconel 718 fabricated by selective laser melting, Acta Mater. (2015) 461–468.

17. L.E. Murr, E. Martinez, S.M. Gaytan, D.A. Ramirez, B.I. Machado, P.W. Shindo, J.L. Martinez, F. Medina, J. Wooten, D. Ciscel, U. Ackelid, R.B. Wicker, Microstructural architecture, microstructures, and mechanical properties for a nickel-base superalloy fabricated by electron beam melting, Metall. Mater. Trans. A 42 (2011) 3491–3508.

18. Z. Wang, K. Guan, M. Gao, X. Li, X. Chen, X. Zeng, The microstructure and mechanical properties of deposited-IN718 by selective laser melting, J. Alloy. Compd. 513 (2012) 518–523.

19. R. Bharath Bhushan, F. Behzad, S. Nahid, A. Amirhesam, M. Narges Shayesteh, Analysis of the deviation in properties of selective laser melted samples fabricated by varying process parameters, in: Proc.SPIE, 2020.

20. R. Bharath Bhushan, F. Carolina, A. Amirhesam, M. Narges Shayesteh, A framework for the optimization of powder-bed fusion process, in: Proc.SPIE, 2021.

21. B.B. Ravichander, A. Amerinatanzi, N. Shayesteh Moghaddam, Study on the effect of powder-bed fusion process parameters on the quality of as-built IN718 parts using response surface methodology, Metals 10 (2020).

22. C. Yan, L. Hao, A. Hussein, D. Raymont, Evaluations of cellular lattice structures manufactured using selective laser melting, Int. J. Mach. Tools Manuf. 62 (2012) 32–38.

23. A. Gebhardt, F.-M. Schmidt, J.-S. Hötter, W. Sokalla, P. Sokalla, Additive manufacturing by selective laser melting the realizer desktop machine and its application for the dental industry, Phys. Procedia 5 (2010) 543–549.

24. H. Qi, M. Azer, A. Ritter, Studies of standard heat treatment effects on microstructure and mechanical properties of laser net shape manufactured INCONEL 718, Metall. Mater. Trans. A 40 (2009) 2410–2422.

25. A. Maamoun, J. Xue, M. Elbestawi, S.C. Veldhuis, The effect of selective laser melting process parameters on the microstructure and mechanical properties of Al6061 and AlSi10Mg alloys, Materials 12 (2019) 12.

26. X. Gong, X. Wang, Z. Jones, K. Cooper, J. Cole, K. Chou, Characterization of Microstructure and Mechanical Property of Inconel 718 from Selective Laser Melting, 2015.

27. T. Trosch, J. Strößner, R. Völkl, U. Glatzel, Microstructure and mechanical properties of selective laser melted Inconel 718 compared to forging and casting, Mater. Lett. 164 (2016) 428–431.

28. Y. Lu, S. Wu, Y. Gan, T. Huang, C. Yang, L. Junjie, J. Lin, Study on the microstructure, mechanical property and residual stress of SLM Inconel-718 alloy manufactured by differing island scanning strategy, Opt. Laser Technol. 75 (2015) 197–206.

29. K. Moussaoui, W. Rubio, M. Mousseigne, T. Sultan, F. Rezai, Effects of selective laser melting additive manufacturing parameters of Inconel 718 on porosity, microstructure and mechanical properties, Mater. Sci. Eng. A 735 (2018) 182–190.

30. N. Nadammal, S. Cabeza, T. Mishurova, T. Thiede, A. Kromm, C. Seyfert, L. Farahbod, C. Haberland, J.A. Schneider, P.D. Portella, G. Bruno, Effect of hatch length on the development of microstructure, texture and residual stresses in selective laser melted superalloy Inconel 718, Mater. Des. 134 (2017) 139–150.

31. J.-P. Choi, G.-H. Shin, S. Yang, D.-Y. Yang, J.-S. Lee, M. Brochu, J.-H. Yu, Densification and microstructural investigation of Inconel 718 parts fabricated by selective laser melting, Powder Technol. 310 (2017) 60–66.

32. A.A. Popovich, V. Sufiiarov, E. Borisov, I. Polozov, D.V. Masaylo, Design and manufacturing of tailored microstructure with selective laser melting, Mater. Phys. Mech. 38 (2018) 1–10.

33. X. Wang, K. Chou, Microstructure simulations of Inconel 718 during selective laser melting using a phase field model, Int. J. Adv. Manuf. Technol. 100 (2019) 2147–2162.

34. D. Zhang, P. Zhang, Z. Liu, Z. Feng, C. Wang, Y. Guo, Thermofluid field of molten pool and its effects during selective laser melting (SLM) of Inconel 718 alloy, Addit. Manuf. 21 (2018).

35. M. Balbaa, S. Mekhiel, M. Elbestawi, J. McIsaac, On selective laser melting of Inconel 718: densification, surface roughness, and residual stresses, Mater. Des. 193 (2020) 108818.

36. X. Gong, K. Chou, Microstructures of Inconel 718 by Selective Laser Melting, in: The Minerals, Metals & Materials Society (eds) In Proceedings of the TMS 2015 144th Annual Meeting & Exhibition, Springer, 2015.

37. B. Farhang, B.B. Ravichander, F. Venturi, A. Amerinatanzi, N. Shayesteh Moghaddam, Study on variations of microstructure and metallurgical properties in various heat-affected zones of SLM fabricated, Nickel. Alloy, Mater. Sci. Eng.: A 774 (2020) 138919.

38. W. Rasband, ImageJ, in, National Institutes of Health and the Laboratory for Optical and Computational Instrumentation, Wisconsin.

39. ASTM, Standard Test Methods for Vickers Hardness and Knoop Hardness of Metallic Materials, in.

40. R. Seede, A. Mostafa, V. Brailovski, M. Jahazi, M. Medraj, Microstructural and microhardness evolution from homogenization and hot isostatic pressing on selective laser melted inconel 718: structure, texture, and phases, J. Manuf. Mater. Process. 2 (2018).

41. F. Zhang, L. Levine, A. Allen, M. Stoudt, G. Lindwall, E. Lass, M. Williams, Y. Idell, C. Campbell, Effect of heat treatment on the microstructural evolution of a nickel-based superalloy additive-manufactured by laser powder bed fusion, Acta Mater. 152 (2018) 200–214.

42. W. Shifeng, L. Shuai, W. Qingsong, C. Yan, Z. Sheng, S. Yusheng, Effect of molten pool boundaries on the mechanical properties of selective laser melting parts, J. Mater. Process. Technol. 214 (2014) 2660–2667.

43. M. Garibaldi, Laser Additive Manufacturing of Soft Magnetic Cores for Rotating Electrical Machinery: Materials Development and Part Design, University of Nottingham, 2018.

44. J.-P. Kruth, M. Badrossamay, E. Yasa, J. Deckers, L. Thijs, J. Humbeeck, Part and material properties in selective laser melting of metals, In Proceedings of the16th International Symposium on Electromachining, ISEM 2010, (2010).

45. T. Jokisch, A. Marko, S. Gook, Ö. Üstündag, A. Gumenyuk, M. Rethmeier, Laser Welding of SLM-Manufactured Tubes Made of IN625 and IN718, Materials (Basel, Switzerland), 12 (2019) 2967.

46. T. Raza, J. Andersson, L.-E. Svensson, Microstructure of selective laser melted alloy 718 in As-manufactured and post heat treated condition, Procedia Manuf. 25 (2018) 450–458.

47. P. Tao, H. Li, B. Huang, Q. Hu, S. Gong, Q. Xu, The crystal growth, intercellular spacing and microsegregation of selective laser melted Inconel 718 superalloy, Vaccum 159 (2019) 382–390.

48. M. Kirka, F. Medina, R. Dehoff, A. Okello, Mechanical behavior of post-processed inconel 718 manufactured through the electron beam melting, Process, Mater. Sci. Eng. A 680 (2016).

49. X. Zhou, Y. Zhong, Z. Shen, W. Liu, The surface-tension-driven Benard conventions and unique sub-grain cellular microstructures in 316L steel selective laser melting, Appl. Phys. 32 (2018).

50. W. Kurz, B. Giovanola, R. Trivedi, Theory of microstructural development during rapid solidification, Acta Metall. 34 (1986) 823–830.

51. A.V. Sergueeva, V. Stolyarov, R. Valiev, A. Mukherjee, Advanced mechanical properties of pure titanium with ultrafine grained structure, Scr. Mater. 45 (2001) 747–752.

52. M.J. Donachie, S.J. Donachie, Superalloys: A Technical Guide, ASM International, 2002.

53. S.H. Fu, J.X. Dong, M.C. Zhang, X.S. Xie, Alloy design and development of INCONEL718 type alloy, Mater. Sci. Eng. A 499 (2009) 215–220.

54. H. Dastgerdi, M. Ostad Shabani, Y. Shajari, The effect of cooling rate on the solutionizing of IN718 superalloy produced via selective laser melting (SLM) method, 3 (2019) 17–22.

55. X. Li, J.J. Shi, C.H. Wang, G.H. Cao, A.M. Russell, Z.J. Zhou, C.P. Li, G.F. Chen, Effect of heat treatment on microstructure evolution of Inconel 718 alloy fabricated by selective laser melting, J. Alloy. Compd. 764 (2018) 639–649.

56. D. Zhang, W. Niu, X. Cao, Z. Liu, Effect of standard heat treatment on the microstructure and mechanical properties of selective laser melting manufactured Inconel 718 superalloy, Mater. Sci. Eng. A 644 (2015) 32–40.

5. INNOVAITIVE FABRICATION DESIGN FOR IN-SITU MARTENSITE DECOMPOSITION AND ENHANCED MECHANICAL PROPERTIES IN LASER POWDER BED FUSED Ti6Al4V ALLOY

5.1. Introduction and overview

Titanium (Ti) and its alloys possess a wide range of properties that make them highly suitable for various applications. These properties include exceptional corrosion resistance, a high strength-to-weight ratio, and remarkable fracture toughness [1-4]. The aerospace and marine industries have long leveraged these properties to their advantage [1, 5-7]. In addition, the biomedical field has shown a keen interest in titanium alloys due to their biocompatibility, as they can be used for producing hard tissue replacements and cardiovascular devices, thereby improving the quality of life for patients [1, 8-11]. Among the titanium alloys, Ti6Al4V, also known as Ti64, is one of the most versatile and extensively used in these industries. This alloy not only exhibits the aforementioned properties but is also cost-effective while providing a performance comparable to that of other titanium alloys [12-15].

Although conventional methods such as casting, forging, and powder metallurgy can yield Ti64 components with comparable mechanical properties [16-20], they are often limited by restricted forging temperature ranges, deficient formability, high material and equipment costs, and inefficient machining times, making it difficult to fabricate complex geometries [21, 22]. To address these challenges, Additive Manufacturing (AM) has emerged as a promising solution, allowing for the fabrication of near-net-shaped components using materials like Ti64, while still maintaining superior or comparable strength levels [23, 24]. Among the AM techniques, Laser Powder Bed Fusion (LPBF) is particularly suitable for manufacturing complex 3D geometries requiring precision, and has been extensively utilized for producing a variety of metallic materials [25-29], with Ti64 being a popular candidate [30-34]. LPBF has the capability to produce Ti64 components that exhibit a wide range of distinct crystallographic phases and microstructures, resulting in a more efficient and productive manufacturing process [22]. Given the growing popularity of LPBF as an AM method, numerous studies have been conducted to analyze the composition, microstructure, and mechanical properties of LPBF Ti64.

The field of LPBF Ti64 fabrication has been extensively researched, with multiple studies exploring ways to improve the mechanical properties of the produced components by adjusting the processing parameters. One example of such research is the study conducted by Khorasani et al. [35] which examined the correlation between laser process parameters, density, and hardness of Ti64. The researchers found that laser power had a direct impact on the hardness and density of the material, whereas the relationship between scanning speed and these properties was inverse. Maleki et al. [36] used a neural network model to optimize the process parameters and enhance the mechanical properties of Ti64. The analysis revealed that the laser process parameters had the same effect on yield and ultimate tensile strengths, with scanning speed having the most significant impact on the variation of yield and ultimate tensile strengths, followed by laser power and hatch spacing. In a study conducted by Plessis [37], The formation of defects in LPBF Ti64 was examined under the influence of process parameters. The study found that increasing laser power resulted in more keyhole formations, while higher scanning speeds offered a safer processing window for avoiding pore formation. However, despite these studies' efforts to optimize the processing parameters for LPBF Ti64 fabrication, there are limits to adjusting the material's properties due to the microstructure's inability to change.

In recent years, attention has shifted towards techniques aimed at promoting decomposition of needle-shaped α′ martensite and hence improving the final mechanical properties of LPBF processed Ti64 [38-42]. For instance, Liu et al. [43] achieved improvements in both tensile strength and ductility of LPBF processed Ti64 by tailoring the process parameters to limit α′ martensite formation. A similar study by Xu et al. [44] obtained in-situ martensitic decomposition by fine-tuning the LPBF fabrication parameters, particularly the laser focal offset distance, resulting in strong and ductile Ti64 parts. Heat treatment has also been investigated as a way to promote decomposition and improve the mechanical properties of LPBF-fabricated Ti64 [45-48]. Nevertheless, this method has been found to be time-consuming and expensive, and may even lead to a loss of strength for the part [45, 47, 49, 50]. While the studies on promoting decomposition of ′ martensite have shown improvements in the mechanical properties of LPBF-processed

Ti64, they have required significant optimization of process parameters and machine-dependent variables using design-of-experiment approaches and trial-and-error attempts. Despite these efforts, the resulting level of improvement may not meet the set requirements of critical industries, indicating a need for further research in this area.

In our previous study on spatial heat transfer conditions during LPBF [51], we found that regions near the surfaces of fabricated parts experience more convection heat transfer, resulting in microstructural inhomogeneity. To address this issue, we designed a border surrounding the main part during LPBF in another study [52] to control heat transfer and achieve a more homogeneous microstructure and composition. Building upon this success, we conducted a new study to investigate the potential of this method for in-situ martensitic transformation during LPBF of Ti64, with the goal of improving its mechanical properties, such as microhardness and ductility, without compromising ultimate tensile strength. This approach involves designing the border to mitigate undesirable convection heat transfer near the part surfaces, which could lead to in-situ martensitic transformation, thereby improving the mechanical properties of the Ti64 parts. Our study aims to contribute to the development of LPBF processing techniques that can improve the mechanical properties of critical components used in various industries.

5.2. Fabrication and Experimental Procedure

5.2.1. Powder Preparation and Fabrication

In this study, gas-atomized Ti64 (grade 5) powder was obtained from EOS North America (Pflugerville, TX, USA) for sample fabrication. Prior to fabrication, the powder underwent particle size analysis using scanning electron microscopy (SEM), as shown in Figure 5.1. The SEM images were analyzed using Image J software to determine the distribution of the powder, revealing an average particle size of approximately 22 m [53]. Moreover, the powder analysis indicated that the majority of the particles had a spherical shape, which is favorable for achieving a high packing density during LPBF processes [54, 55]. The spherical shape of the powder particles can also improve flowability, reduce powder accumulation, and enhance uniformity during the powder deposition process, ultimately leading to improved mechanical properties of the fabricated parts [56, 57].

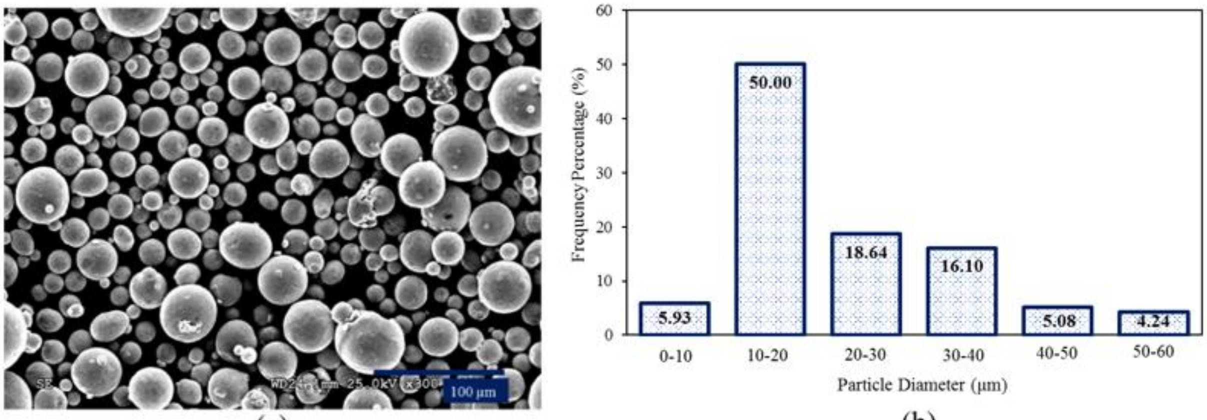

(a) (b)

Figure 5.1.Characterization of EOS Ti64 Grade 5 powder through (a) SEM micrograph and (b) particle size distribution analysis.

Samples were designed using Solidworks (Dassault Systemes, Vélizy-Villacoublay, France) in cube shapes with dimensions of 9 mm × 9 mm × 9 mm and dog-bone specimens with specific dimensions according to the ASTM E8/E8M standard [58], as shown in Figures 5.2 and 5.3. To study the influence of the surrounding borders with different gap distances between the main sample and its associated border, a range of gap values of 0.5, 1.0, 2.0, 3.0, and 4.0 mm were considered for the samples. Samples with the same geometry but without a border were also designed as Reference samples. Table 5.1 summarizes the parameters of all the samples, including sample name, dimensions, geometry, and distance between the sample and its border. These parameters were carefully chosen to ensure that the results of the study are reliable and can be easily compared and reproduced in future research. Since the microstructure observed in the samples Gap 3.0 and Gap 4.0 closely resembled that of the Reference sample, it was determined that the Reference sample would be selected for the mechanical properties analysis as a representative of these specimens.

The fabrication process was performed using an EOS M290 LPBF process printer (EOS GmbH, Electro Optical Systems, Krailling, Germany) with a 400 W Ytterbium fiber laser. The process parameters recommended by the manufacturer, including a laser power of 285 W, hatch distance of 110 µm, scanning speed of 960 mm/s, layer thickness of 40 μm, and stripes scanning strategy with a hatch angle of 67°, were applied for all the samples. The samples were fabricated in an argon atmosphere to prevent oxidation of the Ti64 powder. The temperature of the build plate was maintained at 80 °C during the fabrication process to reduce the thermal gradient within the first few layers. For samples surrounded by a border, both the main part and the border were laser scanned and fabricated at the same time as a single part. To ensure the effectiveness of the heat transfer control at the border, a standardized approach was adopted for all samples in the present study. The fabrication process involved first constructing the border for each sample, followed by the fabrication of the associated main part. This consistent methodology was applied to maintain uniformity and accurately assess the impact of the border on heat transfer. The as-built specimens were removed from the building plate using a wire Electrical Discharge Machining (EDM) cutter (EDM Network, Inc., Sugar Grove, IL, USA).

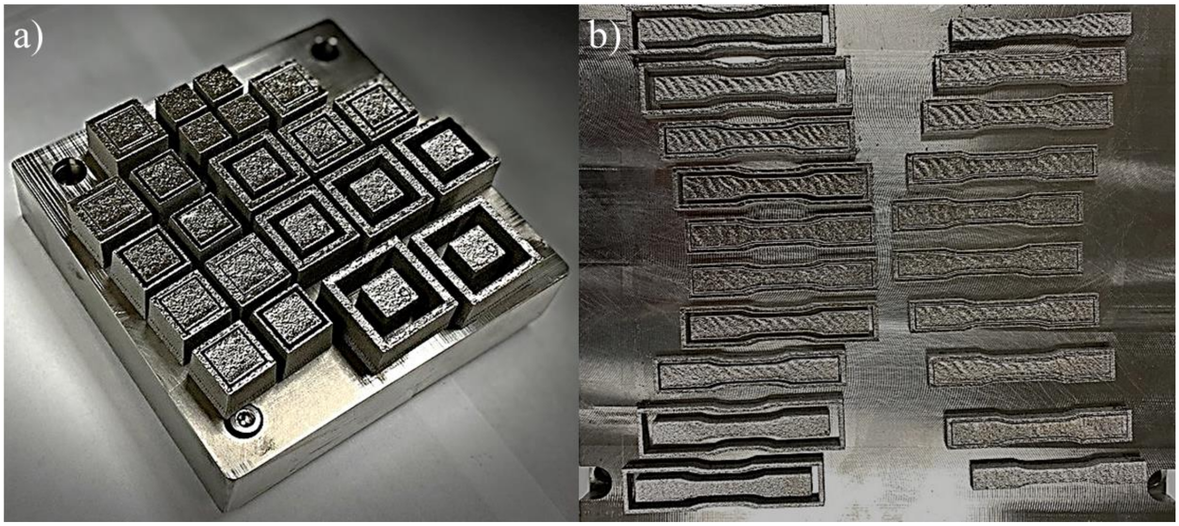

Figure 5.2.LPBF-built samples designed for (a) microstructural analysis and (b) tensile testing.

Table 5.1.Geometry and dimensions of fabricated samples.

Sample Name	Type of Geometr y	Sample Dimensions (mm)	Border Dimensions/ Thickness (mm)	Gap Between Sample and Border (mm)
Ref. (Reference sample)	Cubic	9×9×9 (w×l×h_1)	-	-
Gap 0.5	Cubic	9×9×9 (w×l×h)	9×2 (H×t_2)	0.5
Gap 1.0	Cubic	9×9×9 (w×l×h)	9×2 (H×t)	1.0

Gap 2.0	Cubic	9×9×9 (w×l×h)	9×2 (H×t)	2.0
Gap 3.0	Cubic	9×9×9 (w×l×h)	9×2 (H×t)	3.0
Gap 4.0	Cubic	9×9×9 (w×l×h)	9×2 (H×t)	4.0
Ref. (Reference sample)	Dog-bone	As depicted	-	-
Gap 0.5	Dog-bone	As depicted	2×2 (H×t)	0.5
Gap 1.0	Dog-bone	As depicted	2×2 (H×t)	1.0
Gap 2.0	Dog-bone	As depicted	2×2 (H×t)	2.0

1: w, l and h are width, length, and height of the main sample, respectively.
2: H and t are height and thickness of the border, respectively.

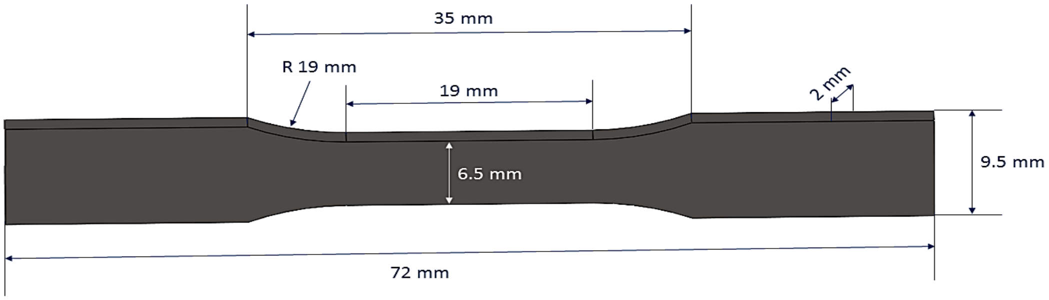

Figure 5.3.Schematic representation of tensile samples used in this study.

5.2.2.Experimental Procedure

For microstructure analysis, the cubic samples were sectioned using a TECHCUT 5™ precision low-speed cutter (Allied High-Tech Products, Inc., Rancho Dominguez, CA, USA), with the cutting plane parallel to the build direction. An area of 3 by 3 mm at the center of the cutting section, close to the border, was used for microstructural analysis for all the samples. Scanning Electron Microscopy (SEM) was performed using a Hitachi S-3000 N variable pressure (Hitachi, Santa Clara, CA, USA). To prepare the samples for SEM, they were first mounted into a mixture of epoxy resin and hardener, followed by grinding and polishing using an E-prep 4™ polisher (Allied High-Tech Products Inc., Rancho Dominguez, CA, USA). The grinding process was conducted using carbide (SiC) abrasive disks ranging from 180 to 1200 Grit sizes. The surface of the samples was checked for scratch patterns using magnifier lenses of a metallographic microscope XJP- H100 (Amscope, Irvine, CA, USA), and the grinding was repeated for each step until a uniform scratch pattern was achieved. The first polishing step was performed on a DiaMat polishing cloth with frequent addition of 1 μm diamond suspension droplets. For the final polishing step, 0.04 μm colloidal silica suspension was spread on a Red Final C polishing pad. After polishing, samples were rinsed in Micro Organic Soap, cleaned using isopropyl alcohol, and finally dried by compressed air. Prior to microstructural tests, samples were etched for a few seconds using Kroll's Reagent (1–3 mL HF, 2–6 mL HNO3, 100 mL water).

A Bruker D8 Advance X-ray diffractometer (Bruker Corporation, Madison, WI, USA) was used to perform compositional analysis of the samples. The Cu K-alpha X-ray source had a wavelength of 1.5406 Å, a current of 40 mA, and a voltage of 40 kV. Measurements were taken at room temperature with step intervals and scan speeds of 0.04° and 1 s/step, respectively, as 2Ɵ varied between 30° and 70°. The volume fraction of each phase was calculated using equation below [59], where Ai represents the total integrated area of each phase and ∑Ai is the total area of all phases. XRD diffractograms were analyzed and the integrated area of each phase was calculated using X'Pert HighScore Plus software (Malvern Panalytical Ltd, Westborough, MA, USA) equipped with ICDD PDF-2 databases (International Centre for Diffraction Data, Newtown Square, PA, USA).

$$V_{f,i} = \frac{A_i}{\sum A_i}$$

Vickers hardness measurements were taken at 10 marked locations along the build direction, and their average values were reported for all samples. The measurements were conducted using a LECO LM 300 AT Micro Hardness Tester (LECO, St. Joseph, MI, USA) with an indentation force of 1 kg, and the indentation was applied for 10 seconds in accordance with ASTM E92 standard [60].

The tensile tests were conducted using a Shimadzu EHF E-series (100 KN) machine equipped with a 4830 Servo Controller (Shimadzu Scientific Instruments, Inc., Missouri City, TX, USA) at a constant loading rate of 1.2 mm/min. Digital image correlation (DIC) was employed to obtain full-field strain measurements and evaluate localized strains during the tests. A random, high-contrast speckle pattern of black micron-sized speckles on a white basecoat was used for the DIC analysis. The specimen surface displacements and strains were calculated by tracking the light intensity patterns corresponding to the speckle pattern using a Grasshopper3 GS3-U3-23S6M CCD camera (FLIR Systems, Inc., Santa Barbara, CA, USA) with a pixel array of 1920×1200 pixels. The VIC-3D® correlation software (Correlated Solutions, Inc., Irmo, SC, USA) was used for image processing and correlation analysis. A region of interest covering the entire gauge length of the samples was selected for analysis, with a subset size and step size of 9 mm and 1 mm, respectively, to achieve the highest accuracy.

5.3. Results

5.3.1. Microstructure analysis

5.3.1.1. Porosity Analysis

The level of residual porosity for all the samples was analyzed by examining SEM micrographs taken from 20 different areas of each sample. Figure 5.4 shows a representative SEM image for the Reference and Gap 0.5 samples, which respectively had the highest and lowest porosity values. Using data analysis, we calculated the average porosity percentage for all the samples, as shown in Figure 5.5. While there was relatively high variation among each sample, the average porosity percentage followed a general trend. Specifically, we observed an increase in the level of porosity with an increase in the gap distance between the sample and border. However, regardless of the gap distance, the average rate of residual porosity was lower for all the samples fabricated with a border compared to that of the Reference sample. Notably, for the Gap 4.0 sample, some micrographs showed the formation of pores that were greater than the average porosity calculated for the Reference sample.

We also calculated the average pore size for all the samples, which is shown in Figure 5.6. Similar to the residual porosity, we found a general trend for the size. However, the average pore size for the Gap 0.5 sample was significantly smaller than all the samples, with only minor variation being observed for the rest of the samples fabricated with a border. Regardless of the gap distance, the Reference sample possessed the highest average pore size. Overall, the results suggest that the use of borders during LPBF process can significantly reduce the occurrence of porosity and improve the quality of fabricated parts, with the optimal gap distance being 0.5 mm.

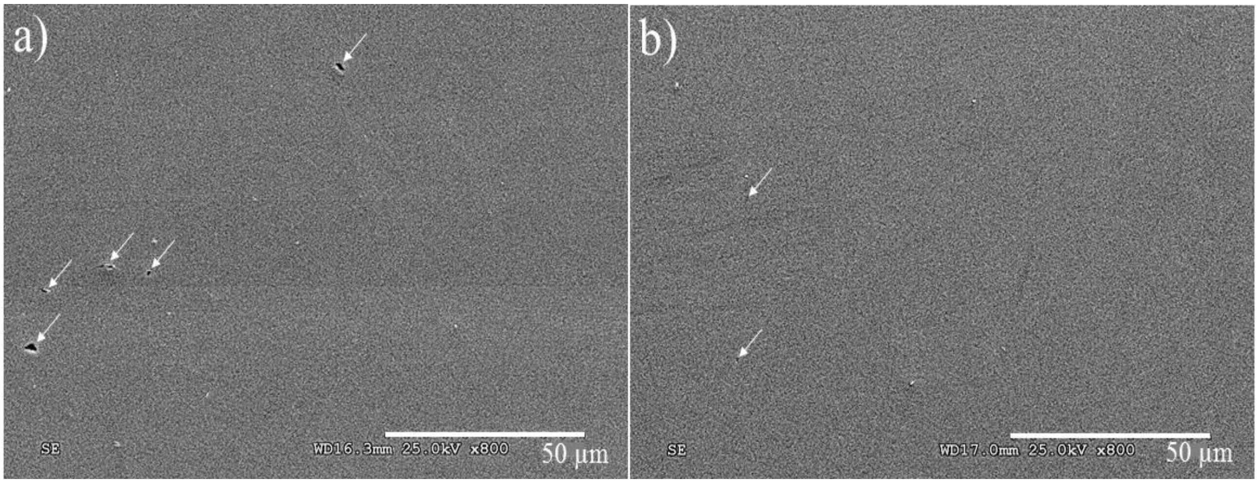

Figure 5.4.Representative scanning electron microscopy (SEM) micrographs showing the distribution of pores for the a) Reference, and b) Gap 0.5 samples.

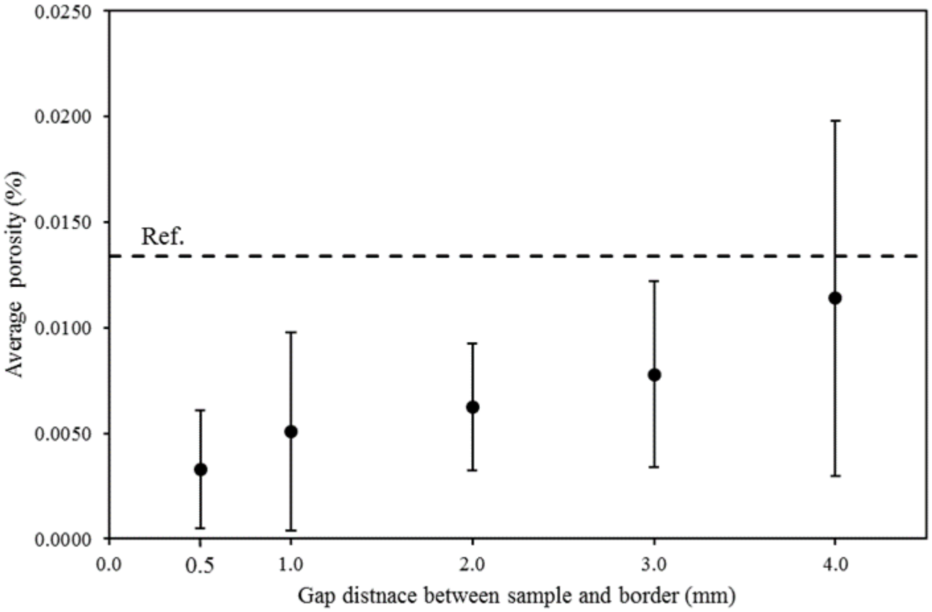

Figure 5.5.Comparison of average porosity levels between samples fabricated with various gap distances between the sample and border, and the Reference sample.

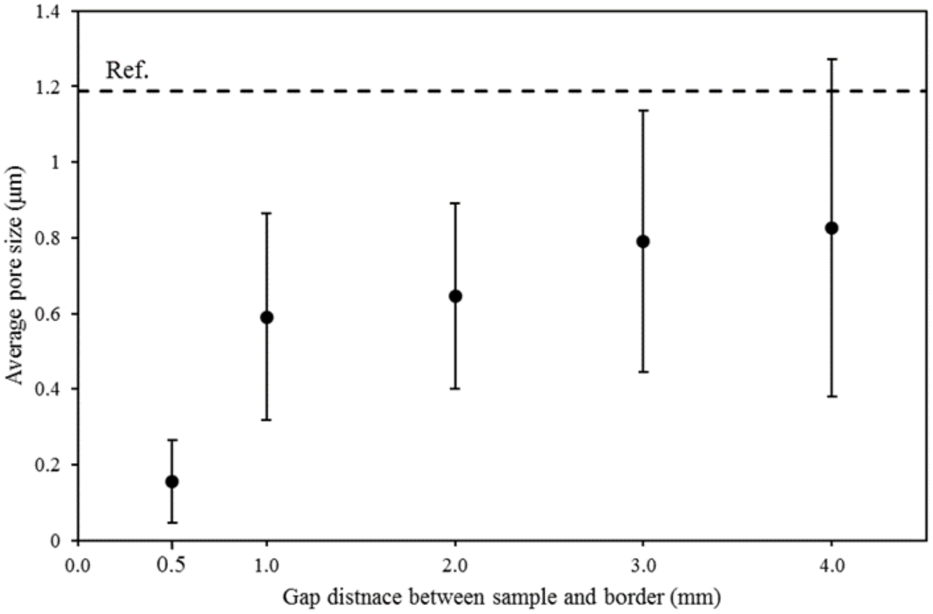

Figure 5.6.Examining the correlation between pore size and gap distance between the sample and border, as compared to the Reference sample.

5.3.1.2. Lath Thickness Analysis

The microstructure of the samples was examined in detail by capturing SEM images from 20 different regions of each sample. The resulting micrographs revealed that the morphology and proportion of the phases (i.e., α, α′, and β) varied to some extent between samples. The most significant variation was observed between the Reference and Gap 0.5 samples. The former mainly consisted of acicular α′ phase, whereas the latter contained a mixture of α + β basket-weave matrix, lamellar α, and acicular α′ (see Figure 5.7). The microstructure of the other samples fell between these two cases, with varying proportions of the different phases. Specifically, the Gap 1.0 and Gap 2.0 samples exhibited a greater prevalence of acicular-like α phase, with a reduction in the formation of α + β matrix. Additionally, the microstructure of the Gap 3.0 and Gap 4.0 samples was similar to that of the Reference sample, as almost entirely acicular α′ morphology was observed for these samples.

The impact of the border gap on the size of the α/α′ phase formed in the samples was investigated by measuring the thickness of α/α′ lamellar/acicular instances in the SEM micrographs. Figure 5.8 presents the results, which indicate that the average thickness of α/α′ increased as the gap value decreased.

Furthermore, the average lath thickness was higher for all samples fabricated with a border compared to the Reference sample. These results suggest that the border gap has a significant impact on the formation of the α/α′ phase and the microstructure of the samples.

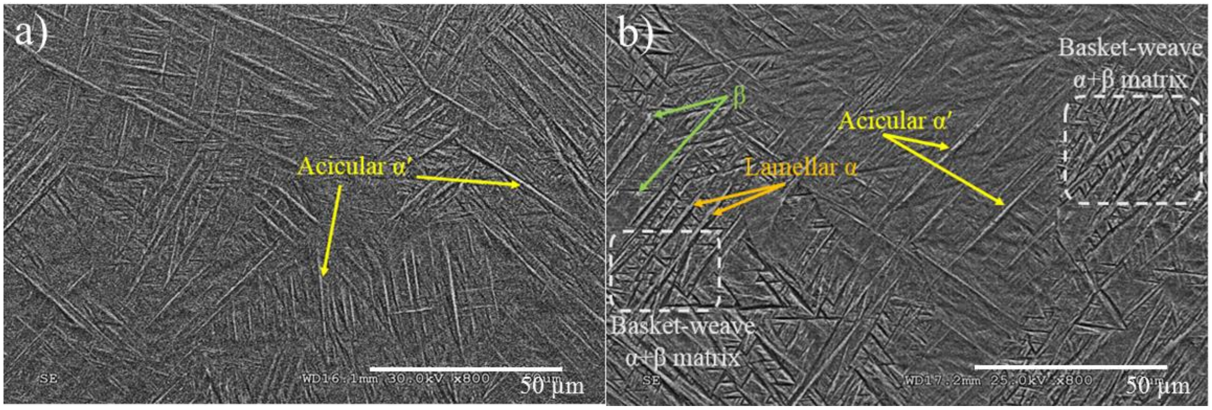

Figure 5.7.The evolution of different phases in the a) Reference and b) Gap 0.5 samples was analyzed using SEM images. The Reference sample mainly consisted of acicular α′ phase, while the Gap 0.5 sample contained a mixture of α + β basket-weave matrix, lamellar α, and acicular α′.

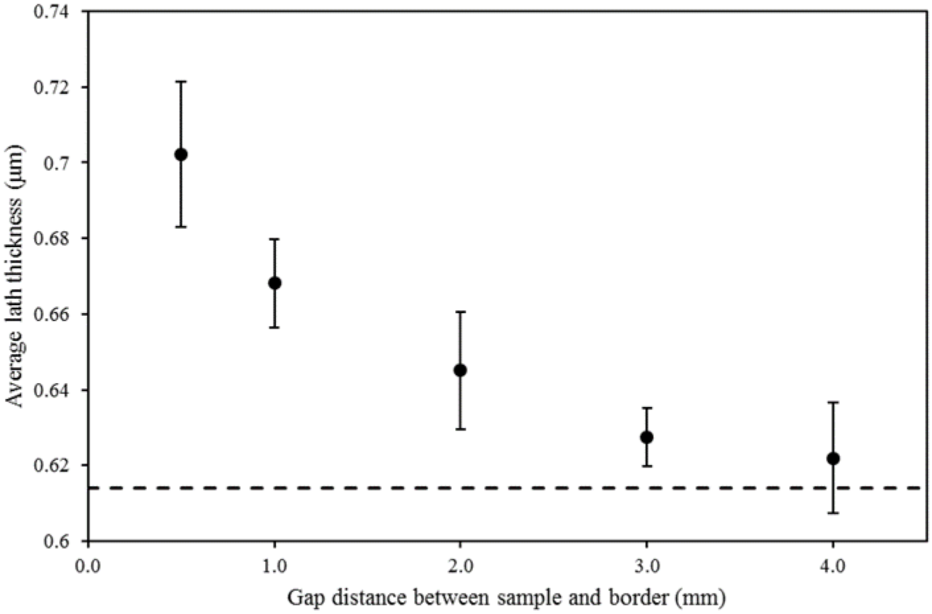

Figure 5.8.The comparison between border samples and the Reference sample reveals that the average thickness of α/α′ increases as the gap distance between the sample and border decreases.

5.3.2. Compositional analysis

5.3.2.1. Energy Dispersive Spectroscopy (EDS) Analysis

Energy Dispersive Spectroscopy (EDS) analysis was used to compare the chemical composition of all samples. While this technique provides only semi-quantitative results and cannot offer high accuracy for the chemical composition of samples, it serves the comparative purpose among samples [61]. To ensure comprehensive analysis, 30 instances of the α lamellar/α′ acicular phase were selected for each sample and the vanadium content was sleeted to be compared among samples. The results of the analysis are presented in Table 5.2, which shows that the vanadium percentage was lowest for the Gap 0.5 sample and increased as the gap value became larger. Conversely, the α/α′ needles in the Reference sample had the highest content of vanadium regardless of the gap size.

Table 5.2.Comparing Vanadium Composition in α/α′ Phase: Various Samples. The vanadium percentage exhibited an increase with increasing gap value, but remained lower compared to the Reference sample.

Sample	*V (Weight %)*
Reference	4.62 ± 0.16
Gap 0.5	3.38 ± 0.17
Gap 1.0	4.11 ± 0.15
Gap 2.0	4.30 ± 0.22
Gap 3.0	4.40 ± 0.20
Gap 4.0	4.56 ± 0.20

5.3.2.2. X-Ray Diffraction (XRD) Analysis

Figure 5.9 illustrates the X-Ray Diffraction (XRD) patterns of the Reference sample and parts fabricated with border, with the spectrographs displayed for the 2θ angles between 30 and 70°. The XRD patterns obtained from the samples showed similarity to those reported for Ti64 LPBF processed specimens [62-65]. The dominant crystallographic phase in all the samples is the hexagonal close-packed (hcp) α/α′ phase, with minor peak(s) attributed to the β-Ti phase. It should be noted that the similar lattice constant and crystal system of α and α′ phases make them difficult to distinguish using XRD data [65, 66]. Although the spectrographs for all the samples follow a similar pattern, a few differences exist between some of the samples. Comparing the position of the main α/α′ peak (around 2θ=40.5°) for all the samples, the largest discrepancy is observed between the Reference and Gap 0.5 sample. Specifically, the peak for the Gap 0.5 sample is shifted towards lower angles compared to the Reference sample, with this difference decreasing as the gap value increases. Concerning the β phase peaks, a weak peak (at 2θ=39.5°) was detected in the XRD patterns of the Reference, Gap 3.0, and Gap 4.0 samples, reflecting a low content of this phase. In contrast, the XRD pattern of Gap 0.5, Gap 1.0, and Gap 2.0 samples revealed a noticeable peak at 2θ=39.5°, indicating a higher content of the β phase in these samples. Notably, the highest content of the β phase is expected for the Gap 0.5 sample, as indicated by the additional peak attributed to the β phase (at 2θ=57.5°) present in its XRD pattern. Table 5.3 provides the β phase content of all the samples, determined by quantitative analysis of their XRD patterns.

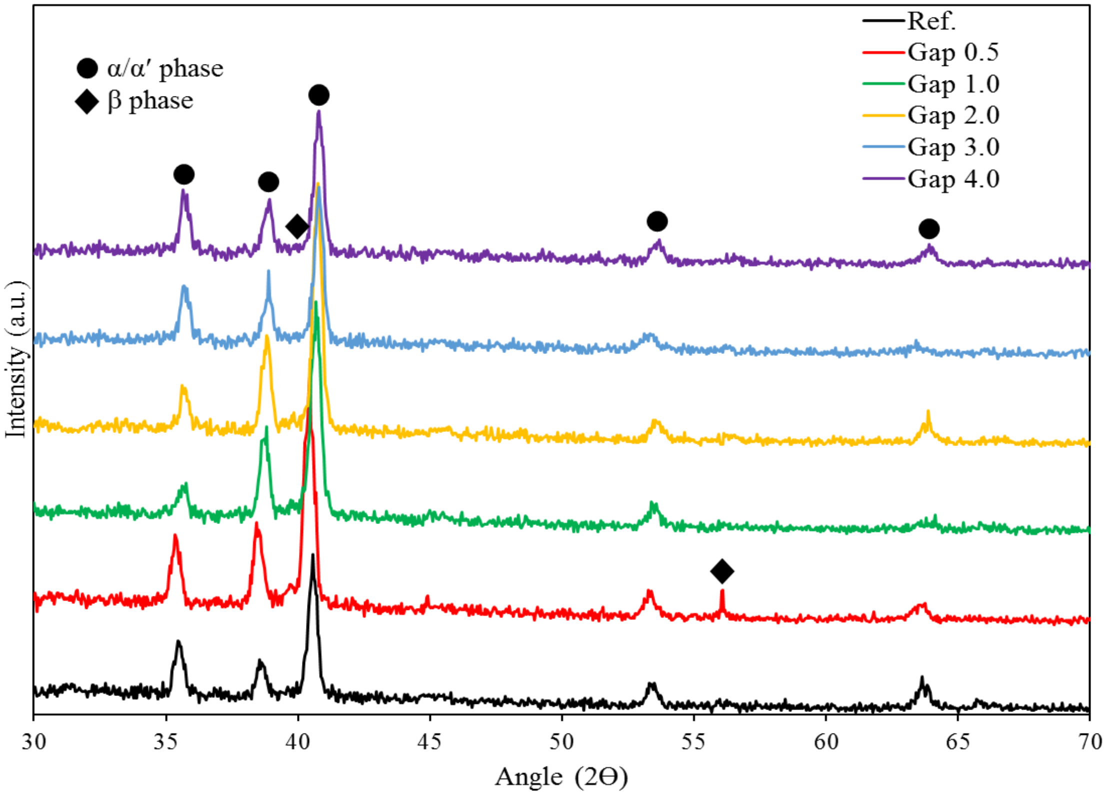

Figure 5.9.X-Ray Diffraction (XRD) spectrographs for the samples, showing slight variations in the position of the main α/α′ peak. The largest discrepancy is observed between the Reference and Gap 0.5 samples. The β phase content is higher in the border samples, with the presence of an additional β phase peak at 2θ=57.5° in the Gap 0.5 sample indicating its highest content.

Table 5.3.Quantitative analysis of the XRD patterns with their possible corresponding microstructure.

Sample	**Reference**	**Gap 0.5**	**Gap 1.0**	**Gap 2.0**	**Gap 3.0**	**Gap 4.0**
β phase (%)	0.23	4.39	2.18	1.58	0.86	0.87
Possible Structure	Full α′	α′+fine (α + β)	α′+lamellar (α + β)	α′+lamellar (α + β)	Full α′	Full α′

To determine the range of variation in the size of the crystallite size (in this case, acicular α′ or ultrafine lamellar α) and lattice parameters among the samples, the full width at half maximum (FWHM) [45] corresponding to the dominant α/α′ peak (at 2θ=40.5°) and the average ratio of c/a for the hcp structure were calculated. The Reference and Gap 0.5 samples were selected for analysis to demonstrate the range of variation. As shown in Table 5.4, the FWHM value for the Gap 0.5 sample was relatively lower, indicating a larger size of α/α′ phase for this sample compared to the Reference sample. However, there was no significant variation in the c/a ratio for any of the samples. This indicates that the deviation found in the XRD for the peak position of the samples was not significant and can be ignored [66, 67].

Table 5.4.Parameters calculated from the XRD patterns for the Reference and Gap 0.5 samples. FWHM for Gap 0.5 sample was lower, indicating larger α/α′ phase size than Reference sample. No significant c/a variation observed, so XRD peak position deviation can be ignored.

Sample/Parameter	**FWHM**	**c/a**
Reference	0.3936	1.597
Gap 0.5	0.3149	1.598

5.3.3. Vickers Hardness

The microhardness of the samples was determined by measuring the Vickers Hardness (HV) at the interest region specified in the experimental procedure. Figure 5.10 shows the average HV value of ten indentations for all the samples. The results indicate a consistent trend in the hardness of the samples. As the gap value decreased from 4 to 0.5 mm, the hardness increased slightly from 389 to 403 HV. However, the Reference sample exhibited the lowest microhardness value of 388 HV, regardless of the variation observed in the hardness values of the specimens fabricated with border. The Vickers hardness values obtained in this study fall within the range reported in previous publications [66, 68, 69].

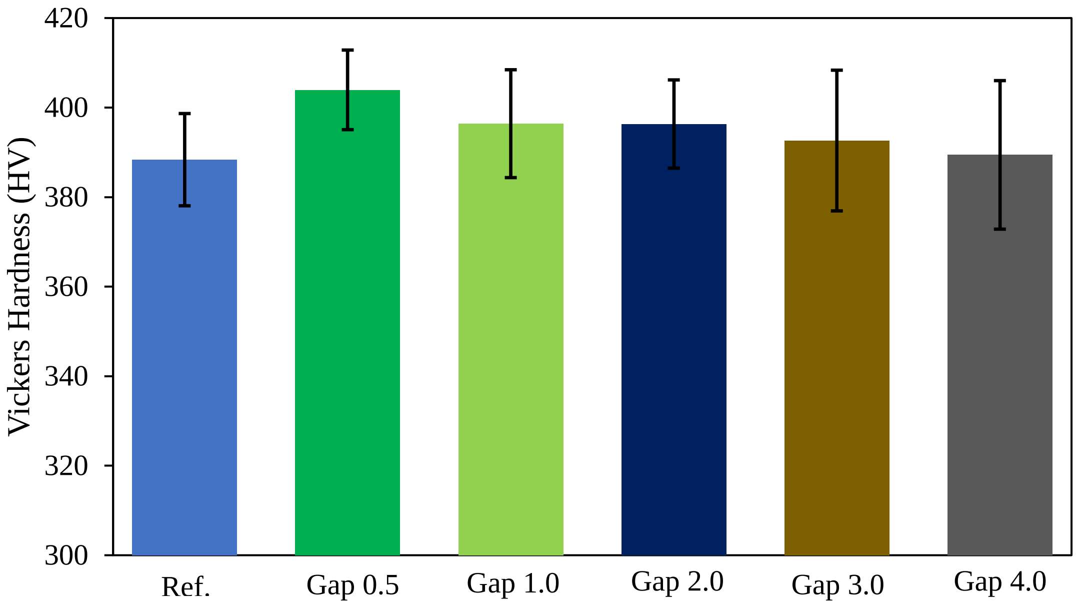

Figure 5.10.The graph illustrates the variation in the average Vickers Hardness (HV) values plotted against the gap value. The results show a slight increase in microhardness as the gap value decreased from 4 to 0.5 mm. The Reference sample had the lowest microhardness value of 388 HV.

5.3.4. Mechanical properties

The tensile testing involved the Reference sample, Gap 0.5, Gap 1.0, and Gap 2.0 samples, as shown in Figure 5.11. It is important to note that the microstructure and composition of Gap 3.0 and Gap 4.0 samples were similar to the Reference sample, hence they were not tested. Although there was a minor variation in fracture strain values, the ultimate tensile strength (UTS) values differed significantly. Table 5.5 provides the UTS values and strain at fracture for each sample. The Gap 0.5 sample exhibited an improvement of about 15% and 9% in UTS and fracture strain, respectively, compared to the Reference sample. The other two samples fabricated with border also showed slight increases in both parameters compared to the Reference sample.

The digital image correlation (DIC) technique was used to obtain a more detailed strain analysis of the samples. Specifically, the strain mapping corresponding to the last frame before fracture (100 ms before failure) was extracted for all samples. In Figure 5.12, the maximum local strain value and its location where the fracture initiated are displayed. The maximum local strain value showed a similar trend as the fracture strain, meaning that the Gap 0.5 sample had the highest maximum local strain value, followed by the samples produced with border and the Reference sample. However, the range of variation was higher for the maximum local strain value. The Gap 0.5 sample experienced a maximum local strain that was about 30% higher than that of the Reference sample and considerably higher than that of the Gap 1.0 and Gap 2.0 samples. This information provides additional insight into the behavior of the samples during tensile testing and further supports the findings of the ultimate tensile strength and fracture strain results.

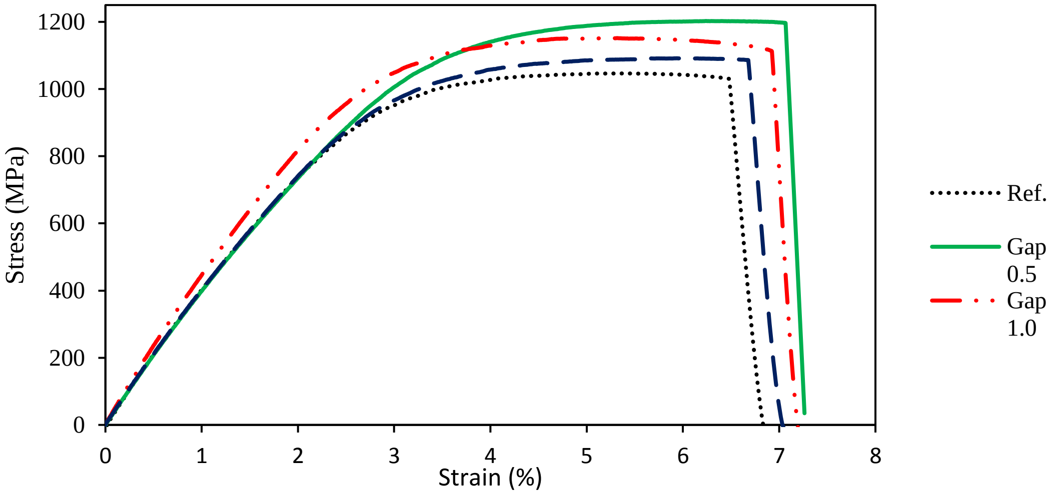

Figure 5.11.Stress-strain plots for the Reference sample, Gap 0.5, Gap 1.0, and Gap 2.0 samples in uniaxial tensile testing. Gap 0.5 sample showed an approximately 15% and 9% improvement in UTS and fracture strain, respectively, compared to the Reference sample.

Table 5.5.Tensile test parameters extracted from the stress-strain plots of the samples.

Sample	***UTS (MPa)***	***Fracture Strain (%)***
Reference	*1046.70*	*6.48*
Gap 0.5	*1202.53*	*7.07*
Gap 1.0	*1151.68*	*6.92*
Gap 2.0	*1091.20*	*6.68*

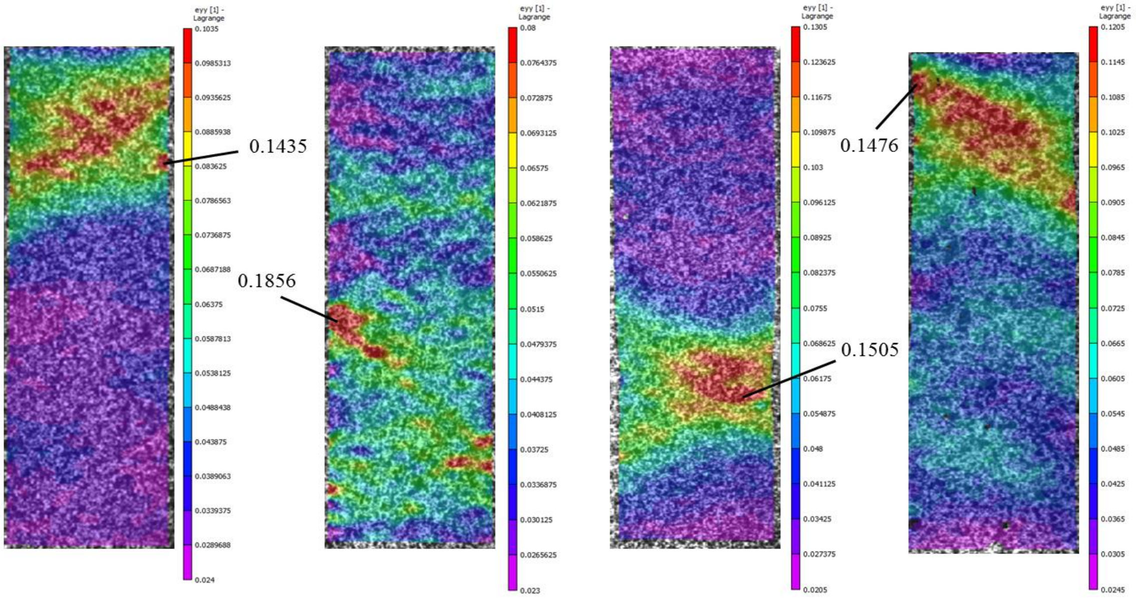

Figure 5.12.The DIC strain mappings corresponding to the frame before fracture extracted for a) Reference, b) Gap 0.5, c) Gap 1.0, and d) Gap 2.0 sample. The Gap 0.5 sample experienced a maximum local strain approximately 30% higher than that of the Reference sample and significantly higher than that of the Gap 1.0 and Gap 2.0 samples..

5.4. Discussion

The present study established that incorporating a border surrounding the main sample can effectively enhance the density level of LPBF-fabricated Ti64 samples. This was verified by SEM micrograph analysis, which demonstrated that reducing the gap size between the border and the main sample resulted in higher density and lower average pore size. The observed improvement in density was attributed to the longer maintenance of molten material at high temperature, which facilitated complete melting of powders. Interestingly, a longer period of maintaining material at elevated temperatures was achieved by reducing the gap size, despite keeping the laser power constant for all samples. This finding aligns with previous studies that reported higher density for LPBF-built Ti64 samples with increased energy input while maintaining the same laser power [65, 66, 68, 70]. Therefore, this study highlights the crucial role of optimizing process parameters, including gap size, in achieving high-quality LPBF-fabricated parts. Superior mechanical properties can be attained by eliminating residual porosity and reducing pore size, making it an important consideration to note [71, 72].

The microstructure analysis of the samples revealed a change in the proportion of the α/α′ and β phases, with the largest variation observed between the Reference and Gap 0.5 samples. This change can be attributed to the cooling rate and the temperature at which the samples undergo cyclic heating and cooling processes. In particular, the presence of a border helps maintain a higher temperature for a longer duration during the LPBF process, facilitating the formation of the β phase. Such effect is especially pronounced in the Gap 0.5 sample, where the border is closest to the sample, resulting in a slower cooling rate and higher temperature retention. This finding is consistent with previous research that has reported the formation of the β phase occurring at temperatures above 750˚C [73]. The formation of the α + β matrix in the microstructure of the Gap 0.5 sample is due to the precipitation of the β phase, which causes vanadium atoms to be expelled from the α′ phase, leading to nucleation of α along the boundaries of the α′ phase [44, 69]. This is in contrast to the fully α′ microstructure observed in the Reference sample, which resulted from a higher solidification rate that was further away from equilibrium [66]. A more detailed explanation of the variation in phases among samples is provided in the following paragraphs, where the sample composition is discussed in more detail. Studies have shown that heating and cooling cycles with higher energy density leads to the coarsening of the α/α′ phases, particularly the acicular α′ phase [33, 74-76]. The thickness of the α/α′ lath is also reported to increase significantly under heat treatment processes [77]. Research studies have observed lath coarsening for Ti64 samples when the temperature was higher during heat treatment and closer to the β transus temperature [50, 78-80]. These observations are in line with the coarsening of the α/α′ phases for the samples fabricated with a border. As the gap value between the sample and border reduces, the heat dissipation is minimized, which keeps the sample at a higher temperature during fabrication. This condition resembles what a sample undergoes during a heat treatment process and therefore supports the coarsening of the α/α′ lath for the samples surrounded by borders. It is a well-known fact that coarsening the α/α′ lath in Ti64 results in a higher level of ductility and improvement of fracture strain [65, 81, 82].

Comparison of the composition of the α/α′ phase spots in all samples revealed that the average weight percentage of vanadium decreased for the samples fabricated with a border. This finding indicates that the decrease in gap value led to a decrease in the proportion of the α′ phase, which contains a higher percentage of vanadium, and an increase in the proportion of the α phase, which contains a lower percentage of vanadium. This change in phase composition could be due to two stages of decomposition: the transformation of the β phase into α or α′ during the cooling stage [66, 83], and the decomposition of the α′ phase into α + β due to the consecutive fabrication of layers [44, 84, 85]. These findings are discussed in more detail in the following paragraph. A study by Gong et al. [61] compared the microstructure of Ti64 samples processed by LPBF and electron beam melting (EBM) and found that keeping the temperature in the EBM process at a higher level (650-700 ˚C) facilitates transformation of β to α phase, while the higher cooling rate experienced in LPBF process results in transformation to α′ phase. This is consistent with the results observed in the present study, where lower vanadium content (associated with α′ phase) was detected for samples fabricated with a border compared to the Reference sample. This suggests that by inducing a border surrounding the sample, the temperature is maintained at a higher level for a longer time, and the cooling rate is reduced, which resembles a heat treatment process to some extent, particularly for samples with lower gap sizes (Gap 0.5 and Gap 1.0 samples). Simonelli et al. [86] observed a variation in the composition of the Ti64 LPBF fabricated samples between areas with different building heights, where they used a long laser-powder interaction time and found higher fabricated layers to be rich in vanadium compared to the initial printed layers. This was attributed to the lower cooling rate applied to the initial layers, achieved by controlling the laser-material interaction time and maintaining the platform's temperature. This cooling approach exhibits resemblances to the post-annealing heat treatment process, as it facilitates the decomposition of the initial martensitic phase observed predominantly during annealing, particularly for the initial layers. In another study on Ti64 [87], applying post-treatment (hot isostatic pressing) to samples resulted in a reduction in vanadium, as observed for the samples fabricated with a border in the present study. Although the range of variation seen in the current study is not as high as applying heat treatment processes, the trend confirms that an appropriate border design can control and achieve the desired level of variation. It should be noted that the formation of the α phase with a lower level of vanadium results in lower residual stress and higher ductility [65, 86].

Upon comparing the XRD patterns of the samples, it was noticed that only Gap 0.5 possessed an additional peak corresponding to the β phase, indicating a higher content of the β phase compared to the other samples (Table 5.3). This suggests that repeated cooling and heating stages during layer-by-layer fabrication may have led to a decomposition of the α′ phase into α and β phases. This decomposition may have occurred through the transformation of α′ into (α + β) structure, or directly into the β phase by heating above the β transus temperature (995 ˚C) and changing the hcp crystal into bcc [67]. However, based on the calculated unit cell parameters, there was no significant change in the c/a ratio for the samples, indicating that the transformation of α′ into β phase was not the main mechanism of decomposition. Rather, the decomposition of α′ into (α + β) structure accounted for the main transformation. In a study by Xu et al. [44], the decomposition of α′ phase during the LPBF process was investigated, and the effects of layer thickness, focal offset distance, and energy density on the transformation of this phase were reported. They found that increasing the energy density improved the in-situ decomposition of α′ phase into ultrafine lamellar (α + β) structure. This is consistent with the findings of this study, where the Gap 0.5 sample, with the highest content of β phase and an α + β structure, was produced using a border to preserve the heat input at a higher level for a longer time. As the gap value increased, heat dissipation occurred at a higher level, resembling a lower energy density, resulting in a Full α′ structure found for the Gap 4.0 sample, similar to the Reference sample. A similar relationship between the energy density and FWHM value was reported for LPBF-fabricated Ti64 samples. Cepeda-Jiménez et al. [66] showed that the FWHM value reduced with an increase in energy density, attributed to the gradual transformation of the α′ phase into α and β phases under the effect of higher energy input. During the decomposition of the α′ phase, vanadium diffused into the matrix, resulting in the formation of α phase with a coarsened crystal structure, which was seen in the EDS results showing lower vanadium content for the Gap 0.5 sample. The reduction in FWHM value indicated the formation of a coarsened structure (α + β) induced by the border and preserved heat input at a higher level. Furthermore, the decomposition of α′ phase into α and β phases, as observed for the Gap 0.5 sample, led to a decrease in the level of lattice distortion and internal stresses [88, 89], as evidenced by the shift in the position of the dominant peak towards lower values, indicating a reduction in strain and improvement in crystallinity [67]. This may have contributed to the outstanding mechanical properties and higher ductility of the Ti64 LPBF processed parts [44], as observed in the mechanical properties of the Gap 0.5 sample in this study.

The comparison of microhardness values for the samples revealed that those fabricated with borders had higher hardness, with the Gap 0.5 sample displaying the highest value. This finding aligns with previous studies on LPBF fabricated Ti64 samples, where an increase in energy density led to a higher level of density and, in turn, a higher microhardness value [68]. Other studies have also shown that LPBF process parameter variations have a similar impact on both microhardness and density [35]. Therefore, it was expected that the samples with borders, which had a higher density level, would have a higher hardness value. However, it is important to consider the effect of α/α′ lath thickness on microhardness, as an increase in thickness typically results in a reduction in hardness [65]. In addition, in-situ martensitic decomposition can also influence the hardness value. For example, studies have shown that heat-treated Ti64 samples with finer α grains, resulting from in-situ transformation of α′ to α phase, have improved hardness compared to fully martensitic as-built samples [77]. Additionally, a microstructure containing both α and α′ phases instead of fully α′ phase has been found to increase the microhardness of Ti64 [69]. Taking these findings into account, the higher level of density and martensitic decomposition found in the samples fabricated with borders (specifically, the Gap 0.5 sample) exceeded the effect of lath thickening and resulted in an increase in the microhardness value.

The stress-strain curves of the samples indicate that the parts fabricated with border exhibit higher tensile strength and elongation compared to the Reference sample. The use of borders also results in more ductile behavior, as confirmed by DIC analysis, which showed a considerably higher local fracture strain for the Gap 0.5 sample. It is known that the mechanical properties of Ti64 depend on the thickness of its constituent phases, the level of defects, and the size of the α/α′ phases [50, 69, 90, 91]. It is well-established that increasing the thickness of the α/α′ lath in Ti64 results in lower strength but higher ductility [44, 65, 77, 92]. However, the effect on strength and ductility is not equal. In fact, Galarraga et al. [93] found that coarsening the α/α′ phases has a greater impact on improving ductility than reducing the ultimate tensile strength (UTS). Therefore, it can be inferred that the higher average thickness of α/α′ acicular/lamellar phases in the samples fabricated with border led to an improvement in ductility while having only a minor effect on UTS. In addition, to enhance the ductility of Ti64, it is crucial to reduce the occurrence and size of defects in the samples, especially the micro-pores that form at the interlayers, as they can ultimately result in microscopic cracks and catastrophic failure. These pores have a detrimental impact on the ductility of Ti64 and can lead to the formation of microscopic cracks, which ultimately result in failure [43, 94, 95]. This finding is supported by Yan et al. [80], who also attributed the enhancement of ductility in Ti64 LPBF-processed samples to the removal of internal defects. While previous studies have shown that the improvement in ductility of Ti64 resulted in a reduction in ultimate tensile strength (UTS) [41, 50, 65, 69, 91], in the current study, the use of borders surrounding the main sample resulted in improvements in both ductility and UTS. Of the factors affecting the mechanical properties of Ti64, variations in microstructure and crystal system, resulting from phase changes, have the most significant impact [91]. Improved ductility of Ti64 without sacrificing its strength can be achieved through controlling a microstructure that includes lamellar (α + β) [78, 96]. In a previous study, an ultrafine lamellar (α + β) microstructure was achieved through in situ martensite decomposition, resulting in significantly better UTS and ductility compared to as-built LPBF fabricated samples [44]. In the current study, the use of borders surrounding the main sample led to the formation of thicker α/α′ acicular/lamellar phases and a lamellar (α + β) microstructure. While the former negatively impacted UTS, the latter increased strength. Despite some variation in lath thickness, the lamellar (α + β) microstructure ultimately outweighed the effect of lath size and resulted in superior mechanical properties for the samples fabricated with borders. Gap 0.5 had the highest elongation and strength among these samples. Additionally, a previous study by Zhou et al. [97] found that increasing energy density improves Ti64 strength, which aligns with the current study's observation that the sample with the lowest gap value (experiencing higher temperature for a longer time) had the maximum UTS. The finer and higher proportion of (α + β) microstructure in this sample's microstructure confirmed its superior mechanical properties (Figure 5.7b). In-situ martensite decomposition can be achieved at 400 ˚C, but this phase transformation can be further facilitated by maintaining the sample at higher temperatures for a longer period [44], as observed in the current study. It's important to note that DIC results showed crack imitation, leading to fracture for all parts, started near the edges of the samples, but no specific trend was observed for the location of crack imitation among the samples.

5.5. References

1. Yadav, P. and K.K. Saxena, Effect of heat-treatment on microstructure and mechanical properties of Ti alloys: An overview. Materials Today: Proceedings, 2020. 26: p. 2546-2557.

2. Romero, C., F. Yang, and L. Bolzoni, Fatigue and fracture properties of Ti alloys from powder-based processes – A review. International Journal of Fatigue, 2018. 117: p. 407-419.

3. Boyer, R.R., An overview on the use of titanium in the aerospace industry. Materials Science and Engineering: A, 1996. 213(1): p. 103-114.

4. Lütjering, G. and J.C. Williams, Titanium. 2013: Springer Berlin Heidelberg.

5. Liu, Z., et al., A Review on Additive Manufacturing of Titanium Alloys for Aerospace Applications: Directed Energy Deposition and Beyond Ti-6Al-4V. JOM, 2021. 73(6): p. 1804-1818.

6. Nyakana, S.L., J.C. Fanning, and R.R. Boyer, Quick reference guide for β titanium alloys in the 00s. Journal of Materials Engineering and Performance, 2005. 14(6): p. 799-811.

7. Fanning, J.C. and S.P. Fox, Recent developments in metastable β strip alloys. Journal of Materials Engineering and Performance, 2005. 14(6): p. 703-708.

8. Rack, H.J. and J.I. Qazi, Titanium alloys for biomedical applications. Materials Science and Engineering: C, 2006. 26(8): p. 1269-1277.

9. Liu, X., P.K. Chu, and C. Ding, Surface modification of titanium, titanium alloys, and related materials for biomedical applications. Materials Science and Engineering: R: Reports, 2004. 47(3): p. 49-121.

10. González, J.E.G. and J.C. Mirza-Rosca, Study of the corrosion behavior of titanium and some of its alloys for biomedical and dental implant applications. Journal of Electroanalytical Chemistry, 1999. 471(2): p. 109-115.

11. Arab, A., P. Chen, and Y. Guo, Effects of microstructure on the dynamic properties of TA15 titanium alloy. Mechanics of Materials, 2019. 137: p. 103121.

12. Welsch, G., R. Boyer, and E.W. Collings, Materials Properties Handbook: Titanium Alloys. 1993: ASM International.

13. Natali, A.N., Dental biomechanics. 2003: CRC Press.

14. Oberwinkler, B., M. Riedler, and W. Eichlseder, Importance of local microstructure for damage tolerant light weight design of Ti–6Al–4V forgings. International Journal of Fatigue, 2010. 32(5): p. 808-814.

15. Wu, G.Q., et al., Effect of microstructure on the fatigue properties of Ti–6Al–4V titanium alloys. Materials & Design, 2013. 46: p. 668-674.

16. Zhou, Y., W. Zeng, and H. Yu, An investigation of a new near-beta forging process for titanium alloys and its application in aviation components. Materials Science and Engineering: A, 2005. 393(1-2): p. 204-212.

17. Leyens, C. and M. Peters, Titanium and titanium alloys: fundamentals and applications. 2003: John Wiley & Sons.

18. Stráský, J., et al., The effect of microstructure on fatigue performance of Ti–6Al–4V alloy after EDM surface treatment for application in orthopaedics. Journal of the Mechanical Behavior of Biomedical Materials, 2011. 4(8): p. 1955-1962.

19. Reda, R., A. Nofal, and A.-H. Hussein, Effect of Quenching Temperature on the Mechanical Properties of Cast Ti-6Al-4V Alloy. Journal of Metallurgical Engineering (ME), 2013. 2: p. 48-54.

20. Froes, F.H.S., M.N. Gungor, and M. Ashraf Imam, Cost-affordable titanium: The component fabrication perspective. JOM, 2007. 59(6): p. 28-31.

21. Park, N.-K., J.-T. Yeom, and Y.-S. Na, Characterization of deformation stability in hot forging of conventional Ti–6Al–4V using processing maps. Journal of Materials Processing Technology, 2002. 130-131: p. 540-545.

22. Murr, L.E., et al., Microstructure and mechanical behavior of Ti–6Al–4V produced by rapid-layer manufacturing, for biomedical applications. Journal of the Mechanical Behavior of Biomedical Materials, 2009. 2(1): p. 20-32.

23. Trevisan, F., et al., Additive manufacturing of titanium alloys in the biomedical field: processes, properties and applications. J Appl Biomater Funct Mater, 2018. 16(2): p. 57-67.

24. Dutta, B. and F.H. Froes, The Additive Manufacturing (AM) of titanium alloys. Metal Powder Report, 2017. 72(2): p. 96-106.

25. Safaei, K., et al., The Build Orientation Dependency of NiTi Shape Memory Alloy Processed by Laser Powder Bed Fusion. Shape Memory and Superelasticity, 2022. 8(4): p. 265-276.

26. Safaei, K., et al. Controlling crystallographic texture and thermomechanical properties of NiTi shape memory alloy through laser powder bed fusion. in SMST2022. 2022. ASM International.

27. Ganesh-Ram, A., et al. Study of Spatter Formation and Effect of Anti-Spatter Liquid in Laser Powder Bed Fusion Processed Ti-6Al-4V Samples. in 2021 International Solid Freeform Fabrication Symposium. 2021. University of Texas at Austin.

28. Ramachandra, S., et al. Impact of Porosity Type on Microstructure and Mechanical Properties in Selectively Laser Melted IN718 Lattice Structures. in 2021 International Solid Freeform Fabrication Symposium. 2021. University of Texas at Austin.

29. Ravichander, B., et al. Investigation of the Properties of Reinforced IN718 Structures Fabricated using Laser Powder Bed Fusion. in 2021 International Solid Freeform Fabrication Symposium. 2021. University of Texas at Austin.

30. Sow, M.C., et al., Influence of beam diameter on Laser Powder Bed Fusion (L-PBF) process. Additive Manufacturing, 2020. 36: p. 101532.

31. King, W.E., et al., Observation of keyhole-mode laser melting in laser powder-bed fusion additive manufacturing. Journal of Materials Processing Technology, 2014. 214(12): p. 2915-2925.

32. Oliveira, J.P., A.D. LaLonde, and J. Ma, Processing parameters in laser powder bed fusion metal additive manufacturing. Materials & Design, 2020. 193: p. 108762.

33. Thijs, L., et al., A study of the microstructural evolution during selective laser melting of Ti–6Al–4V. Acta Materialia, 2010. 58(9): p. 3303-3312.

34. Baufeld, B. and O. van der Biest, Mechanical properties of Ti-6Al-4V specimens produced by shaped metal deposition. Science and Technology of Advanced Materials, 2009. 10(1): p. 015008.

35. Khorasani, A., et al., The effect of SLM process parameters on density, hardness, tensile strength and surface quality of Ti-6Al-4V. Additive Manufacturing, 2019. 25: p. 176-186.

36. Maleki, E., S. Bagherifard, and M. Guagliano, Application of artificial intelligence to optimize the process parameters effects on tensile properties of Ti-6Al-4V fabricated by laser powder-bed fusion. International Journal of Mechanics and Materials in Design, 2022. 18(1): p. 199-222.

37. du Plessis, A., Effects of process parameters on porosity in laser powder bed fusion revealed by X-ray tomography. Additive Manufacturing, 2019. 30: p. 100871.

38. Chen, L.Y., et al., Anisotropic response of Ti-6Al-4V alloy fabricated by 3D printing selective laser melting. Materials Science and Engineering: A, 2017. 682: p. 389-395.

39. Qiu, C., N.J.E. Adkins, and M.M. Attallah, Microstructure and tensile properties of selectively laser-melted and of HIPed laser-melted Ti–6Al–4V. Materials Science and Engineering: A, 2013. 578: p. 230-239.

40. Shi, X., et al., Selective laser melting-wire arc additive manufacturing hybrid fabrication of Ti-6Al-4V alloy: Microstructure and mechanical properties. Materials Science and Engineering: A, 2017. 684: p. 196-204.

41. Simonelli, M., Y.Y. Tse, and C. Tuck, Effect of the build orientation on the mechanical properties and fracture modes of SLM Ti–6Al–4V. Materials Science and Engineering: A, 2014. 616: p. 1-11.

42. Xu, W., et al., In situ tailoring microstructure in additively manufactured Ti-6Al-4V for superior mechanical performance. Acta Materialia, 2017. 125: p. 390-400.

43. Liu, J., et al., Achieving Ti6Al4V alloys with both high strength and ductility via selective laser melting. Materials Science and Engineering: A, 2019. 766: p. 138319.

44. Xu, W., et al., Additive manufacturing of strong and ductile Ti–6Al–4V by selective laser melting via in situ martensite decomposition. Acta Materialia, 2015. 85: p. 74-84.

45. Tsai, M.-T., et al., Heat-treatment effects on mechanical properties and microstructure evolution of Ti-6Al-4V alloy fabricated by laser powder bed fusion. Journal of Alloys and Compounds, 2020. 816: p. 152615.

46. Pathania, A., A.K. Subramaniyan, and B.K. Nagesha, Influence of post-heat treatments on microstructural and mechanical properties of LPBF-processed Ti6Al4V alloy. Progress in Additive Manufacturing, 2022. 7(6): p. 1323-1343.

47. Yadroitsev, I., et al., Qualification of Ti6Al4V ELI Alloy Produced by Laser Powder Bed Fusion for Biomedical Applications. JOM, 2018. 70(3): p. 372-377.

48. Wu, M.-W., et al., Intensification of preferred orientation in the additive manufactured Ti-6Al-4V alloy after heat treatment. Materials Letters, 2021. 286: p. 129198.

49. Mahmud, A., et al., Mechanical behavior assessment of Ti-6Al-4V ELI alloy produced by laser powder bed fusion. Metals, 2021. 11(11): p. 1671.

50. Vrancken, B., et al., Heat treatment of Ti6Al4V produced by Selective Laser Melting: Microstructure and mechanical properties. Journal of Alloys and Compounds, 2012. 541: p. 177-185.

51. Farhang, B., et al., Study on variations of microstructure and metallurgical properties in various heat-affected zones of SLM fabricated Nickel–Titanium alloy. Materials Science and Engineering: A, 2020. 774: p. 138919.

52. Farhang, B., et al., The evolution of microstructure and composition homogeneity induced by borders in laser powder bed fused Inconel 718 parts. Journal of Alloys and Compounds, 2022. 898: p. 162787.

53. Schindelin, J., et al., Fiji: an open-source platform for biological-image analysis. Nature Methods, 2012. 9(7): p. 676-682.

54. Brika, S.E., et al., Influence of particle morphology and size distribution on the powder flowability and laser powder bed fusion manufacturability of Ti-6Al-4V alloy. Additive Manufacturing, 2020. 31: p. 100929.

55. Riener, K., et al., Influence of particle size distribution and morphology on the properties of the powder feedstock as well as of AlSi10Mg parts produced by laser powder bed fusion (LPBF). Additive Manufacturing, 2020. 34: p. 101286.

56. Haferkamp, L., et al., The influence of particle shape, powder flowability, and powder layer density on part density in laser powder bed fusion. Metals, 2021. 11(3): p. 418.

57. Sehhat, M.H., et al., Investigation of Mechanical Properties of Parts Fabricated with Gas- and Water-Atomized 304L Stainless Steel Powder in the Laser Powder Bed Fusion Process. JOM, 2022. 74(3): p. 1088-1095.

58. E8, A. ASTM E8 Standard Test Methods for Tension Testing of Metallic Materials 1. in ASTM. 2013.

59. Hamza, H.M., K.M. Deen, and W. Haider, Microstructural examination and corrosion behavior of selective laser melted and conventionally manufactured Ti6Al4V for dental applications. Materials Science and Engineering: C, 2020. 113: p. 110980.

60. E92-17, A., Standard test methods for Vickers hardness and Knoop hardness of metallic materials. 2017, ASTM International West Conshohocken, PA.

61. Gong, H., et al. The effects of processing parameters on defect regularity in Ti-6Al-4V parts fabricated by selective laser melting and electron beam melting. in 2013 International Solid Freeform Fabrication Symposium. 2013. University of Texas at Austin.

62. Huang, J.-Y., et al., Systematic evaluation of selective fusion additive manufacturing based on thermal energy source applied in processing of titanium alloy specimens for medical applications. The International Journal of Advanced Manufacturing Technology, 2020. 109(9): p. 2421-2429.

63. Lan, L., et al., Effects of laser shock peening on microstructure and properties of Ti–6Al–4V titanium alloy fabricated via selective laser melting. Materials, 2020. 13(15): p. 3261.

64. Cui, Y.-W., et al., Metastable pitting corrosion behavior of laser powder bed fusion produced Ti-6Al-4V in Hank’s solution. Corrosion Science, 2022. 203: p. 110333.

65. Zhao, X., et al., Comparison of the microstructures and mechanical properties of Ti–6Al–4V fabricated by selective laser melting and electron beam melting. Materials & Design, 2016. 95: p. 21-31.

66. Cepeda-Jiménez, C.M., et al., Effect of energy density on the microstructure and texture evolution of Ti-6Al-4V manufactured by laser powder bed fusion. Materials Characterization, 2020. 163: p. 110238.

67. Kaschel, F.R., et al., Mechanism of stress relaxation and phase transformation in additively manufactured Ti-6Al-4V via in situ high temperature XRD and TEM analyses. Acta Materialia, 2020. 188: p. 720-732.

68. Bartolomeu, F., et al., Predictive models for physical and mechanical properties of Ti6Al4V produced by Selective Laser Melting. Materials Science and Engineering: A, 2016. 663: p. 181-192.

69. Jaber, H., et al., Effects of Annealing and Solution Treatments on the Microstructure and Mechanical Properties of Ti6Al4V Manufactured by Selective Laser Melting. Materials, 2022. 15(5): p. 1978.

70. Pal, S., et al., Evolution of metallurgical properties of Ti-6Al-4V alloy fabricated in different energy densities in the Selective Laser Melting technique. Journal of Manufacturing Processes, 2018. 35: p. 538-546.

71. Buhairi, M.A., et al., Review on volumetric energy density: influence on morphology and mechanical properties of Ti6Al4V manufactured via laser powder bed fusion. Progress in Additive Manufacturing, 2023. 8(2): p. 265-283.

72. Yi, J.H., et al., Effect of laser energy density on the microstructure, mechanical properties, and deformation of Inconel 718 samples fabricated by selective laser melting. Journal of Alloys and Compounds, 2019. 786: p. 481-488.

73. Brandl, E., A. Schoberth, and C. Leyens, Morphology, microstructure, and hardness of titanium (Ti-6Al-4V) blocks deposited by wire-feed additive layer manufacturing (ALM). Materials Science and Engineering: A, 2012. 532: p. 295-307.

74. Murr, L.E., et al., Microstructures and mechanical properties of electron beam-rapid manufactured Ti–6Al–4V biomedical prototypes compared to wrought Ti–6Al–4V. Materials Characterization, 2009. 60(2): p. 96-105.

75. Vilaro, T., C. Colin, and J.D. Bartout, As-Fabricated and Heat-Treated Microstructures of the Ti-6Al-4V Alloy Processed by Selective Laser Melting. Metallurgical and Materials Transactions A, 2011. 42(10): p. 3190-3199.

76. Toh, W.Q., et al., Microstructure and wear properties of electron beam melted Ti-6Al-4V parts: A comparison study against as-cast form. Metals, 2016. 6(11): p. 284.

77. Li, H., et al., Effect of heat treatment on microstructure evolution and mechanical properties of selective laser melted Ti–6Al–4V and TiB/Ti–6Al–4V composite: A comparative study. Materials Science and Engineering: A, 2021. 801: p. 140415.

78. Lütjering, G., Influence of processing on microstructure and mechanical properties of (α+β) titanium alloys. Materials Science and Engineering: A, 1998. 243(1): p. 32-45.

79. Tan, X., et al., Revealing martensitic transformation and α/β interface evolution in electron beam melting three-dimensional-printed Ti-6Al-4V. Scientific Reports, 2016. 6(1): p. 26039.

80. Yan, X., et al., Effect of heat treatment on the phase transformation and mechanical properties of Ti6Al4V fabricated by selective laser melting. Journal of Alloys and Compounds, 2018. 764: p. 1056-1071.

81. Facchini, L., et al., Ductility of a Ti-6Al-4V alloy produced by selective laser melting of prealloyed powders. Rapid Prototyping Journal, 2010. 16(6): p. 450-459.

82. Bermingham, M.J., et al., Optimising the mechanical properties of Ti-6Al-4V components produced by wire + arc additive manufacturing with post-process heat treatments. Journal of Alloys and Compounds, 2018. 753: p. 247-255.

83. Tan, P., et al., A thermo-metallurgical-mechanical model for selective laser melting of Ti6Al4V. Materials & Design, 2019. 168: p. 107642.

84. Barriobero-Vila, P., et al., Inducing Stable α + β Microstructures during Selective Laser Melting of Ti-6Al-4V Using Intensified Intrinsic Heat Treatments. Materials, 2017. 10(3): p. 268.

85. Xing, L.-L., et al., Influence of Powder Bed Temperature on the Microstructure and Mechanical Properties of Ti-6Al-4V Alloy Fabricated via Laser Powder Bed Fusion. Materials, 2021. 14(9): p. 2278.

86. Simonelli, M., Y.Y. Tse, and C. Tuck, The formation of α+ β microstructure in as-fabricated selective laser melting of Ti–6Al–4V. Journal of Materials Research, 2014. 29(17): p. 2028-2035.

87. Petrovskiy, P., et al., Effect of encapsulated hot isostatic pressing on properties of Ti6Al4V deposits produced by cold spray. The International Journal of Advanced Manufacturing Technology, 2020. 107(1): p. 437-449.

88. Sallica-Leva, E., et al., Ductility improvement due to martensite α′ decomposition in porous Ti–6Al–4V parts produced by selective laser melting for orthopedic implants. Journal of the Mechanical Behavior of Biomedical Materials, 2016. 54: p. 149-158.

89. Gu, D., et al., Densification behavior, microstructure evolution, and wear performance of selective laser melting processed commercially pure titanium. Acta materialia, 2012. 60(9): p. 3849-3860.

90. Xu, Y., et al., Microstructural tailoring of As-Selective Laser Melted Ti6Al4V alloy for high mechanical properties. Journal of Alloys and Compounds, 2020. 816: p. 152536.

91. Liu, S. and Y.C. Shin, Additive manufacturing of Ti6Al4V alloy: A review. Materials & Design, 2019. 164: p. 107552.

92. Ali, H., et al., In-situ residual stress reduction, martensitic decomposition and mechanical properties enhancement through high temperature powder bed pre-heating of Selective Laser Melted Ti6Al4V, in Materials Science and Engineering: A. 2017. p. 211-220.

93. Galarraga, H., et al., Effects of heat treatments on microstructure and properties of Ti-6Al-4V ELI alloy fabricated by electron beam melting (EBM). Materials Science and Engineering: A, 2017. 685: p. 417-428.

94. Sun, W., et al., Effects of build direction on tensile and fatigue performance of selective laser melting Ti6Al4V titanium alloy. International Journal of Fatigue, 2020. 130: p. 105260.

95. Cao, S., et al., Defect, Microstructure, and Mechanical Property of Ti-6Al-4V Alloy Fabricated by High-Power Selective Laser Melting. JOM, 2017. 69(12): p. 2684-2692.

96. Agius, D., K.I. Kourousis, and C. Wallbrink, A Review of the As-Built SLM Ti-6Al-4V Mechanical Properties towards Achieving Fatigue Resistant Designs. Metals, 2018. 8(1): p. 75.

97. Zhou, B., et al., A study of the microstructures and mechanical properties of Ti6Al4V fabricated by SLM under vacuum. Materials Science and Engineering: A, 2018. 724: p. 1-10.

6. CONCLUSIONS AND FUTURE WORKS

6.1. Conclusion

In this study, the properties of two Nickel-based and Titanium-based alloys fabricated via Laser Powder Bed Fusion (LPBF) were thoroughly examined. The microstructural, compositional, and metallurgical properties of the samples were analyzed using Optical Microscopy (OM), Secondary Electron Microscopy (SEM), Energy Dispersive X-Ray Spectroscopy (EDS), X-ray Diffraction (XRD), and Vickers hardness tests. Mechanical testing and digital image correlation (DIC) analysis were also employed to substantiate the microstructure findings. Three distinct investigations yielded several outcomes for the LPBF fabricated alloys.

The first investigation focused on the spatial variation of microstructure, composition, and metallurgical properties in the NiTi alloy. Upon analyzing the top and side surfaces of the sample, it was observed that the grains near the surface were finer compared to those further away. From the side view, larger, elongated grains were found farther from the substrate, while smaller, equiaxed grains were discovered closer to it. The melt pools exhibited differing characteristics based on their location, and both the areas near the surface and substrate shared a higher quantity of defects. Precipitates, including Ni-rich and Ti-rich types, were found near the surface and substrate, and the ratio of austenitic to martensitic phases varied throughout the sample. The highest hardness values were observed away from the surface and substrate in both views.

The second investigation delved into the evolution of microstructure homogeneity across the cross-section of LPBF-processed IN718 parts. A specialized design was used to create cubic samples with and without borders, and the microstructure was compared among them. Deeper melt pools, denser columnar grain structures, and lower surface porosity were found in samples fabricated with borders. XRD analysis confirmed the presence of more columnar grain structures along the build direction and a lower lattice parameter in samples with borders due to increased precipitation of secondary phases. These samples also demonstrated higher hardness values.

In the third investigation, the effects of cubic border design and gap space on the properties of LPBF-processed Ti64 were assessed. Utilizing a border surrounding the main part improved the density, with a higher level of density and lower average defect size obtained as the gap space decreased. The morphology and proportion of the phases were altered by the presence of the border. The microstructure varied between samples based on gap space, and the thickness of the α/α′ lath increased as the gap value decreased. The average weight percentage of vanadium decreased in samples fabricated with borders, and XRD analysis confirmed the presence of different amounts of β phase in the samples. Microhardness measurements revealed a minor increasing trend as the gap value reduced, with the Reference sample possessing the lowest value. The stress-strain curves showed higher tensile strength and ductility for samples fabricated with borders, which was also supported by the DIC analysis. It was concluded that in-situ martensitic decomposition could be achieved through implementing borders surrounding the parts.

6.2. Future Work

The following suggestions are proposed for future research directions in this field:

- Examine the influence of border geometry on the microstructural adjustment of LPBF samples.
- Investigate the impact of borders on the properties of LPBF parts with complex geometries.
- Optimize microstructural homogeneity and mechanical properties throughout the height of LPBF-processed components.
- Explore the effect of borders on the fatigue properties of LPBF-fabricated parts.
- Employ finite element analysis to simulate the influence of borders on homogenizing heat transfer during the LPBF process.